GEOCHEMICAL ASSESSMENT OF DOLERITE FROM OGHI, MANSEHRA, KHYBER PAKHTUNKHWA, PAKISTAN

SHOAIB AHMAD

09-262242-017

BAHRIA UNIVERSITY ISLAMABAD

GEOCHEMICAL ASSESSMENT OF DOLERITE FROM OGHI, MANSEHRA, KHYBER PAKHTUNKHWA, PAKISTAN

SHOAIB AHMAD

09-262242-017

A thesis is submitted in fulfillment of the requirement for the award of the degree of Master of Science (Geology)

Department of Earth and Environmental Sciences

BAHRIA UNIVERSITY ISLAMABAD

OCTOBER 2026

Bahria University

Department of Earth & Environmental Sciences

Islamabad Campus, Islamabad

Date: October 06, 2026

Certificate

A thesis submitted by **Mr. Shoaib Ahmad** to the Department of Earth & Environmental Sciences, Bahria University, Islamabad in partial fulfillment of the requirements for the degree of **Master of Science in Geology** (Session **2024– 2026).**

Committee Members	Name	Signature
Supervisor	Dr. Mumtaz Ali Khan	
Internal Examiner	Dr. Muhammad Raiees Amjad	
External Examiner	Dr. Muhammad Sajid	
Post Graduate Coordinator	Dr. Adeeb Ahmed	
Head of Department (E&ES)	Dr. Syed Umair Ullah Jamil	

APPROVAL OF EXAMINATION

Scholar's Name: "Shoaib Ahmad"

Registration No: "71999"

Program of Study: MS Geology

Thesis Title: "GEOCHEMICAL ASSESSMENT OF DOLERITE FROM OGHI, MANSEHRA, KHYBER PAKHTUNKHWA, PAKISTAN"

It is to certify that the above scholar's thesis has been completed to my satisfaction and to my belief, its standard is appropriate for submission for examination. I have also conducted plagiarism test of this thesis using HEC prescribed software and found similarity index 8% that is within the permissible limit set by the HEC for the MS degree thesis. I have also found the thesis in a format recognized by the BU for the MS thesis.

NOTE: The Plagiarism report is attached at the end of thesis.

Supervisor's Signature:_____

Date:

Name: Dr. Mumtaz Ali Khan

AUTHOR'S DECLERATION

I, "Mr. Shoaib Ahmad" is hereby stating that my MS thesis titled "GEOCHEMICAL ASSESSMENT OF DOLERITE FROM OGHI, MANSEHRA, KHYBER PAKHTUNKHWA, PAKISTAN" is my own work and has not been submitted previously by me of taking any degree from this university "Bahria University Islamabad Campus" or anywhere else in the country/world.

At any time if my statement is found to be incorrect even after my graduation, the University has the right to withdraw/cancel my MS degree.

Scholar Name: Shoaib Ahmad

Sign: _____

Date:

PLAGIARISM UNDERTAKING

I solemnly declare that research work presented in the thesis titled "GEOCHEMICAL ASSESSMENT OF DOLERITE FROM OGHI, MANSEHRA, KHYBER PAKHTUNKHWA, PAKISTAN" is solely my research work with no significant contribution from any other person. Small contribution/help wherever taken has been duly acknowledged and that complete thesis has been written by me.

I understand the zero tolerance policy of HEC and Bahria University towards plagiarism. Therefore, I as an author of the above titled thesis declared that no portion of my thesis has been plagiarized, and any material used as reference is properly referred/ cited.

I understand that if, I am found guilty of any formal plagiarism in the above titled thesis even after award of MS degree, the university reserves the right to withdraw, revoke my MS degree and that HEC and the University has the right to publish my name on the HEC/University website on which names of the scholars are placed who submitted plagiarized thesis.

Scholar/Author's

Sign: _____

Name of the Scholar: Shoaib Ahmad

DEDICATION

-This thesis is dedicated to my family-

ACKNOWLEDGEMENT

All praise and gratitude are due to Almighty Allah, the Most Gracious and the Most Merciful, whose infinite blessings, compassion, and divine guidance enabled the successful completion of this research. It is solely through His grace and mercy that this work has reached its culmination.

I owe my deepest and most sincere gratitude to my supervisor, Dr. Mumtaz Ali Khan, Associate Professor in the Department of Earth and Environmental Sciences at Bahria University, H-11 Campus, Islamabad. His invaluable guidance, scholarly wisdom, and consistent intellectual engagement were central to every phase of this research. Through his constructive feedback, patient mentorship, and unwavering dedication to academic rigor, he not only gave this thesis its direction but also enriched my understanding of the field in ways that will continue to benefit me throughout my professional life. I also extend my sincere appreciation to Allama Iqbal Open University for generously providing access to analytical facilities and technical expertise that proved indispensable to the sample analysis component of this study.

A special and heartfelt acknowledgment is due to my parents and family, whose unconditional love, constant prayers, and steadfast moral support have served as the bedrock of every milestone I have achieved throughout my academic journey. Their encouragement has been, and continues to be, my greatest source of strength. Lastly, I wish to express my sincere appreciation to all those who, in any capacity, contributed to the completion of this thesis. Their assistance and encouragement are deeply valued and gratefully acknowledged.

ABSTRACT

A detailed ICP-MS based trace element geochemical analysis of sixteen dolerite samples (SS1–SS16) from Oghi, Mansehra with the primary objective of identifying and interpreting critical minerals as defined by the United States Geological Survey (USGS) Final 2025 List of Critical Minerals have been conducted. A total of 68 minerals were measured across all samples, with concentrations reported in parts per million (ppm) and qualitative designations of Above Detection Limit (ADL), and Below Detection Limit (BDL). Out of the 60 minerals on the USGS 2025 critical minerals list, 56 are represented by measured elements within this dataset, making this the first systematic critical mineral assessment of mafic intrusions in the Oghi Mansehra region. Palladium was detected in 15 of 16 samples (0.0185–0.1873 ppm), co-occurring with Platinum (11 samples) and Ruthenium/Iridium (6 samples each), indicating a pervasive PGE signature linked to sulfide-phase control (sulfur ADL in 10/16 samples). Copper appears in all samples (mean 0.239 ppm, max 0.5458 ppm), alongside elevated Te, Sb, Ag, and As. REEs show universal Eu, Gd, and Y detection, plus V and Ti. Niobium occurs in 12 samples (up to 0.1292 ppm in SS2), with moderate Ta and BDL Cr. High K (ADL in 10/16 samples), universal Rb (mean 0.251 ppm), and universally ADL P were also observed. Fe, Ca, Na, and S levels confirm a ferro-magnesian mafic composition, while low Th/U in SS1 (Th: 0.0251 ppm, U: 0.4130 ppm) suggests possible secondary uranium mobility. Nonetheless, the findings show that dolerites from Oghi can serve as meaningful repositories of critical elements and provide a baseline for future investigation. Recommended follow-up work includes denser sampling, identification of mineral host phases, sequential extraction, fluid inclusion and isotopic studies, and structural mapping, all of which are necessary before any responsible assessment of resource potential can be made.

TABLE OF CONTENTS

CHAPTER NO.	TITLE	PAGE NO.
	APPROVAL OF EXAMINATION	i
	AUTHOR'S DECLARATION	ii
	PLAGIARISM UNDERTAKING	iii
	DEDICATION	iv
	ACKNOWLEDGEMENT	v
	ABSTRACT	vi
	LIST OF TABLES	xi
	LIST OF FIGURES	xii
	LIST OF ABBREVIATIONS	xv
1	**INTRODUCTION**	1
	1.1 Introduction	1
	1.2 Problem statement	5
	1.3 Objectives	6
	1.4 Significance of the study	6
	1.5 Expected outcomes	6
2	**GEOLOGY AND TECTONICS**	7
	2.1 Literature review	7
	2.2 Geology of study area	9
	2.3 Tectonostratigraphic divisions	11
	2.4 Hazara Region Tectonics and Stratigraphic Succession	12
	2.4.1 Tectonic Framework of the Hazara Region	12
	2.5 Stratigraphy of study area	13

2.5.1 Precambrian to Recent 15
2.5.1.1 Mansehra Granitic Complex and Dolerite Dykes and Sills 16
3 METHODOLOGY 18
3.1 Work methodology 18
3.1.1 Fieldwork and Sampling 19
3.1.2 Sample preparation 23
3.1.3 Inductively Coupled Plasma Mass Spectrometry (ICP-MS) 27
3.1.3.1 Components of ICP-MS 27
3.1.3.2 Working principle of ICP-MS 28
4 RESULTS AND INTERPRETATION 29
4.1 Dataset 29
4.2 Critical Minerals 30
4.2.1 Aluminum (Al) 30
4.2.2 Antimony (Sb) 31
4.2.3 Arsenic (As) 32
4.2.4 Barite (Ba) 33
4.2.5 Beryllium (Be) 34
4.2.6 Bismuth (Bi) 35
4.2.7 Boron (B) 35
4.2.8 Cerium (Ce) 36
4.2.9 Chromium (Cr) 37
4.2.10 Cobalt (Co) 38
4.2.11 Copper (Cu) 39
4.2.12 Dysprosium (Dy) 40
4.2.13 Erbium (Er) 41
4.2.14 Europium (Eu) 42
4.2.15 Gadolinium (Gd) 43
4.2.16 Gallium (Ga) 44
4.2.17 Germanium (Ge) 45
4.2.18 Hafnium (Hf) 46
4.2.19 Holmium (Ho) 47
4.2.20 Indium (In) 48
4.2.21 Iridium (Ir) 48
4.2.22 Lanthanum (La) 49

4.2.23 Lead (Pb) 50
4.2.24 Lithium (Li) 51
4.2.25 Lutetium (Lu) 52
4.2.26 Magnesium (Mg) 53
4.2.27 Manganese (Mn) 54
4.2.28 Neodymium (Nd) 55
4.2.29 Nickel (Ni) 56
4.2.30 Niobium (Nb) 57
4.2.31 Palladium (Pd) 58
4.2.32 Phosphorus (P) 59
4.2.33 Platinum (Pt) 60
4.2.34 Potassium (K) 61
4.2.35 Praseodymium (Pr) 62
4.2.36 Rhenium (Re) 63
4.2.37 Rhodium (Rh) 63
4.2.38 Rubidium (Rb) 63
4.2.39 Ruthenium (Ru) 64
4.2.40 Samarium (Sm) 65
4.2.41 Scandium (Sc) 66
4.2.42 Silicon (Si) 67
4.2.43 Silver (Ag) 67
4.2.44 Tantalum (Ta) 68
4.2.45 Tellurium (Te) 69
4.2.46 Terbium (Tb) 70
4.2.47 Thulium (Tm) 71
4.2.48 Tin (Sn) 72
4.2.49 Tungsten (W) 72
4.2.50 Titanium (Ti) 73
4.2.51 Uranium (U) 74
4.2.52 Vanadium (V) 75
4.2.53 Ytterbium (Yb) 76
4.2.54 Yttrium (Y) 76
4.2.55 Zinc (Zn) 77
4.2.56 Zirconium (Zr) 78
4.2.57 Uses of critical minerals 79
4.3 Other minerals 81
4.3.1 Cadmium (Cd) 81
4.3.2 Calcium (Ca) 82

4.3.3 Gold (Au) 83
4.3.4 Iron (Fe) 83
4.3.5 Mercury (Hg) 84
4.3.6 Molybdenum (Mo) 84
4.3.7 Selenium (Se) 85
4.3.8 Sodium (Na) 85
4.3.9 Strontium (Sr) 86
4.3.10 Sulfur (S) 87
4.3.11 Thallium (Tl) 88
4.3.12 Thorium (Th) 89
4.3.13 Uses of other minerals 90
5 DISCUSSION 92
5.1 Discussion 92
CONCLUSIONS 99
RECOMMENDATIONS 101
REFERENCES 102

LIST OF TABLES

TABLE NO.	TITLE	PAGE NO.
2.1	Generalized Stratigraphy of Mansehra Region showing rock formations from Precambrian to the recent, with formation of interest highlighted in yellow (Awan et al., 2021)	14
3.1	Coordinates of sample points	21

LIST OF FIGURES

FIGURE NO.	TITLE	PAGE NO.
1.1	Study area location map, Oghi, Mansehra highlighted in red box (ArcMap 10.5)	5
2.1	Geological map of the study area located south of the Main Mantle Thrust (MMT), spanning the region between the Swat and Kaghan valleys (after Treloar and Rex, 1990). Abbreviations: AT = Alpurai Thrust; BSZ = Balakot Shear Zone; BT = Batal Thrust; IR = Indus River; KF = Khannian Fault; MBT = Main Boundary Thrust; MMT = Main Mantle Thrust; PT = Panjal Thrust; TSZ = Thakot Shear Zone	11
3.1	Adopted methodology for study	19
3.2	Outcrop of Dolerite at Oghi, Mansehra, from where sampling was done, intrusion contact between country rock and dolerite marked in yellow, North arrow for northing	20
3.3	Dolerite sampling location map showing sampling points from where sampling was conducted highlighted in yellow along with labels (within the vicinity of Oghi city), (ArcMap 10.5)	22
3.4	Weighing balance used for fines	25
3.5	Heating sample solution for digestion of specimen fines in acid	25

3.6	Sample filtration process	26
3.7	Syringe filtration processes	26
3.8	Final digested samples in bottles	27
3.9	Schematic Diagram of ICP-MS (Kashani & Mostaghimi, 2010)	28
4.1	Aluminum values observed in samples	30
4.2	Antimony values observed in samples	31
4.3	Arsenic values observed in samples	32
4.4	Barite values observed in samples	33
4.5	Beryllium values observed in samples	34
4.6	Boron values observed in samples	36
4.7	Cerium values observed in samples	37
4.8	Chromium values observed in samples	38
4.9	Copper values observed in samples	39
4.10	Dysprosium values observed in samples	40
4.11	Erbium values observed in samples	41
4.12	Europium values observed in samples	42
4.13	Gadolinium values observed in samples	43
4.14	Gallium values observed in samples	44
4.15	Germanium values observed in samples	45
4.16	Hafnium values observed in samples	46
4.17	Holmium values observed in samples	47
4.18	Iridium values observed in samples	49
4.19	Lanthanum values observed in samples	50
4.20	Lithium values observed in samples	51
4.21	Lutetium values observed in samples	52
4.22	Magnesium values observed in samples	53
4.23	Manganese values observed in samples	54
4.24	Neodymium values observed in samples	55
4.25	Nickel values observed in samples	56
4.26	Niobium values observed in samples	57
4.27	Palladium values observed in samples	58
4.28	Phosphorus values observed in samples	59
4.29	Platinum values observed in samples	60
4.30	Potassium values observed in samples	61
4.31	Praseodymium values observed in samples	62

4.32	Rubidium values observed in samples	64
4.33	Ruthenium values observed in samples	65
4.34	Samarium values observed in samples	66
4.35	Scandium values observed in samples	67
4.36	Silver values observed in samples	68
4.37	Tantalum values observed in samples	69
4.38	Tellurium values observed in samples	70
4.39	Terbium values observed in samples	71
4.40	Thulium values observed in samples	72
4.41	Titanium values observed in samples	73
4.42	Uranium values observed in samples	74
4.43	Vanadium values observed in samples	75
4.44	Ytterbium values observed in samples	76
4.45	Yttrium values observed in samples	77
4.46	Zinc values observed in samples	78
4.47	Zirconium values observed in samples	79
4.48	Cadmium values observed in samples	81
4.49	Calcium values observed in samples	82
4.50	Iron values observed in samples	84
4.51	Sodium values observed in samples	86
4.52	Strontium values observed in samples	87
4.53	Sulfur values observed in samples	88
4.54	Thallium values observed in samples	89
4.55	Thorium values observed in samples	90

LIST OF ABBREVEATIONS

ADL	-	Above Detection Limit
BDL	-	Below Detection Limit
IEA	-	The International Energy Agency
UNEP	-	The United Nations Environment Program
SS1-SS16	-	Shoaib Sample 1-Shoaib Sample 16
MBT	-	Main Boundary Thrust
MCT	-	Main Central Thrust
MGC	-	Mansehra Granitic Complex
MKT	-	Main Karakoram Thrust
MMT	-	Main Mantle Thrust
PGE/PGEs	-	Platinum Group Elements
Ppm	-	Parts per million
REE/REEs	-	Rare Earth Elements
USGS	-	United States Geological Survey

CHAPTER 1

INTRODUCTION

1.1 Introduction

The northwestern part of the Himalayas in Pakistan is a geodynamically active area, which is the most structurally complex part of the Alpine Himalayan orogenic system. This area is formed due to gradual convergence and subsequent collision of the Indian and Eurasian plates, which was a tectonic event that began in the Late Mesozoic and ended in the Cenozoic time period. The resulting orogenic architecture has large scale thrust systems, crustal scale shear zones, granitoid intrusions, metamorphic complexes and mafic magmatic events that all document numerous phases of deformation and magmatism. The Hazara Kashmir Syntaxis is one such structural culmination, in which major thrust sheets bend and intersect, to generate an area of extreme deformation and crustal rearrangement. Oghi, Mansehra region is located in the western arm of such a syntaxis and contains lithological assemblages that are crucial in determining the tectonomagmatic history of northwestern Himalaya (Tahirkheli, 1979; Treloar and Izatt, 1993).

Oghi has a very strong influence of major Himalayan tectonic boundaries such as the Main Boundary Thrust and the north Main Mantle Thrust. Among these structures of regional scale, there are local zones of shear like the Oghi Shear Zone which allow strain partitioning and avenues in which magma can ascend. Shear zones of collisional orogens are also often sources of syn to post tectonic intrusions, most often mafic dykes, which take advantage of brittle to ductile crustal transitions. Introduction of dolerite dykes into the Oghi sector should be assessed to be in this

tectonic framework where structural anisotropies were probably used to regulate the orientation, thickness, and distribution of the dykes (DiPietro and Pogue, 2004).

The geologic formations of the Oghi Mansehra area are stratigraphically arranged in the form of a series of Precambrian to Paleozoic rocks that constitute the basement of the Hazara Basin. The oldest sequence is Tanawal Formation, which consists of the metasedimentary quartzites, phyllites, and schists (Calkins et al., 1975; Tahirkheli and Majid, 1977). The bodies of granitoids intruding these metasediments constitute the Mansehra Granitic Complex, which comprises a large part of the intrusive crust of the region.

U-Pb geochronology of zircon has limited the emplacement of the Mansehra granitoids to the Early Paleozoic (from 483-476 Ma), which suggests magmatism related to crustal thickening and anatexis in the course of the early orogeny (Naeem et al., 2016). Geochemically, the granites are S type and peraluminous, which is in line with their origin as a result of partial melting of metasedimentary protoliths.

After the emplacement of granitic material, the mafic intrusions were then emplaced in the form of dolerite dyke and sills in the granitic and metasedimentary host rocks. The dolerites may be most readily seen along Oghi Darband corridor and in places like Maira Chanser and Jodan Khatta. Field relationships imply acute intrusive contacts with the Mansehra granite which implies emplacement after crystallization and cooling of the granitoid host. The dolerites are petrographically fine to medium grained ophitic to sub ophitic, plagioclase and clinopyroxene with accessory quartz, amphibole, biotite and are opaque. The presence of ophitic intergrowths and low levels of alters speaks of a relatively fast rate of crystallization of mafic magma generated at shallow crustal depths (Ismaeel et al., 2019).

The Oghi dolerites have sub-alkaline to tholeiitic affinities, and lie in the field of the gabbroic compositional field geochemically. Their ferroan nature and fairly high contents of Fe and Ti indicate that they are the products of mantle derived melts which underwent minimal crustal contamination (Ismaeel et al., 2019). Similar rift

related mafic dykes of the Malka region of Lower Swat have been taken to be due to the presence of extensional tectonics associated with the northwestern boundary of the Indian plate (Majid et al., 1991; Le Bas et al., 1987). The fact that the Oghi dolerites may have similar petrogenetic affinities points to the importance of a thorough geochemical analysis with reference to the distribution of trace and rare earth elements.

During the last few decades, the significance of critical minerals has increased dramatically on the global level. Some of the elements that are essential to renewable energy technologies, electric vehicle batteries, advanced electronics, and strategic defense uses include rare earth elements (REEs), lithium, cobalt, nickel, and platinum group elements (Ali et al., 2017). The shift to low carbon energy systems has generated unparalleled demand on these materials, which has led to a resurgence of interest in mafic and ultramafic intrusions around the globe.

Research has shown that economically valuable elements can be concentrated in mafic systems by magmatic differentiation, segregation of sulfides, and hydrothermal modification (Naldrett, 2013; Robb, 2013). Although the layered intrusions are classic, dyke swarms and lesser mafic bodies have also proven to be potentially successful in hosting Ni-Cu sulfides and REE enriched phases when high favorable conditions are present.

Although this has changed the world focus of exploration, dolerite intrusions of Oghi have in the past been examined through the prism of construction and engineering. Research has been devoted to petrography, major element geochemistry, and physico-mechanical characteristics of importance to the appropriateness of aggregate and dimension stone (Ismaeel et al., 2019). Despite the fact that these studies defined the mechanical competency and mineralogical properties of the dolerites, they did not comprehensively assess trace element geochemistry and critical mineral potential. This lack in the complete geochemical datasets is a major gap in the knowledge base of the regional geological literature.

Critical minerals are defined as non fuel mineral commodities whose supply disruption could have significant consequences for national economic security and technological competitiveness, and their strategic importance has grown substantially in recent decades as modern economies have become increasingly dependent on a narrow suite of materials for applications spanning clean energy, advanced electronics, defense systems, and digital communications (Graedel et al., 2015). The concept of mineral criticality is assessed in terms of supply risk, geopolitical concentration of production, the absence of viable substitutes, and vulnerability to supply restriction are factors that vary over time as technologies, trade relationships, and extraction capacities evolve (Graedel et al., 2015). In response to these vulnerabilities, the U.S. Geological Survey (USGS), as mandated by the Energy Act of 2020, published the Final 2025 List of Critical Minerals on November 7, 2025, comprising 60 mineral commodities which includes rare earth elements, platinum group elements, lithium, cobalt, nickel, vanadium, titanium, and copper, among others, representing the most comprehensive and science based assessment of minerals critical to the U.S. economy and national security to date (U.S. Geological Survey, 2025). This list, which adds 10 new minerals compared to the 2022 update, is not a permanent designation but will be updated at least every three years to reflect current supply, demand, and policy priorities (U.S. Geological Survey, 2025). Considerable research has been directed globally toward identifying and quantifying critical mineral resources within diverse geological settings, with mafic to ultramafic intrusions, pegmatites, and alkaline systems emerging as particularly significant hosts for platinum group elements, rare earth elements, nickel, cobalt, and associated critical metals (Jowitt et al., 2018). Despite this global momentum, systematic critical mineral assessments of mafic intrusions in the Himalayan region of Pakistan remain largely absent from the literature, underscoring the need for geochemically focused investigations such as the present study.

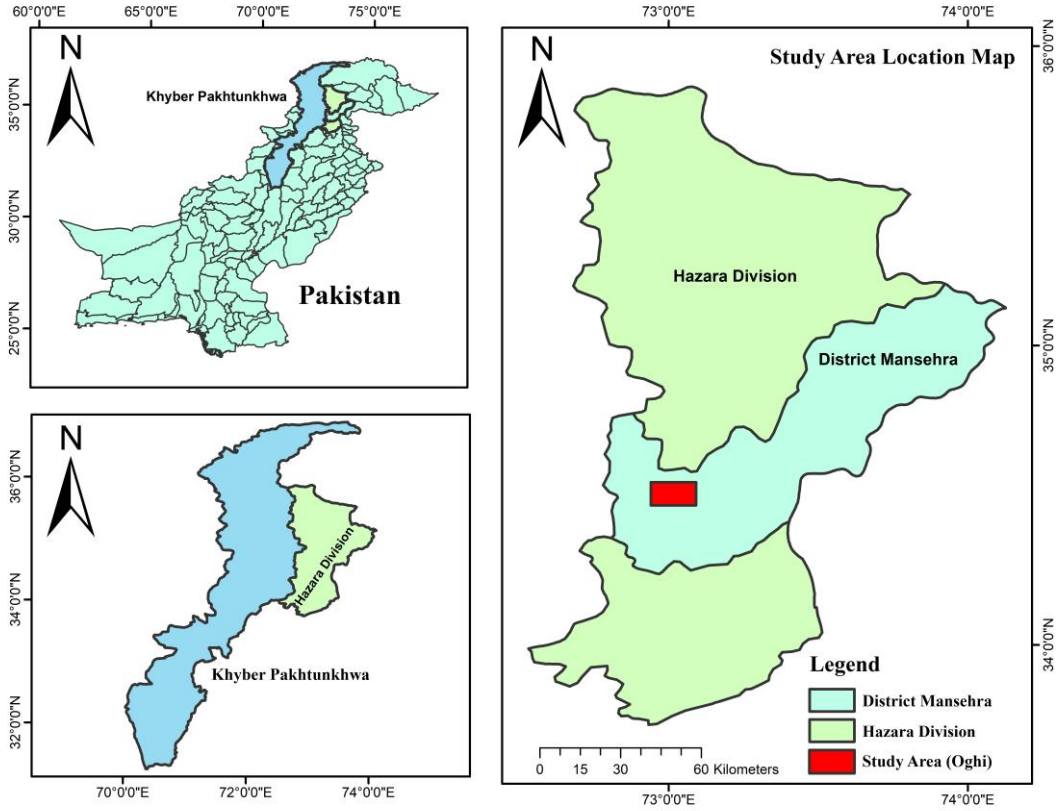


Figure 1.1 Study area location map, Oghi, Mansehra highlighted in red box (ArcMap 10.5)

1.2 Problem statement

No comprehensive geochemical assessment has yet been conducted on dolerite intrusions in the Oghi, Mansehra. This lack of systematic work limits knowledge of their mineral potential, despite their strategic geological position near major Himalayan tectonic structures such as the Hazara Kashmir Syntaxis and their potential role in hosting critical minerals.

1.3 Objectives

The primary objectives of this research are to;

a) To carry out the geochemical analysis and evaluate the concentration of critical minerals of dolerite intrusions within the Mansehra Granite in Oghi.
b) To establish the mineral resource potential of the studied dolerite intrusions.

1.4 Significance of the study

This study will provide the first detailed geochemical characterization of dolerite intrusions within Mansehra Granite from Oghi, offering foundational insights into the geochemical nature of these intrusions. The study will also evaluate the critical mineral potential of this under-explored area to provide a comprehensive understanding of the resource landscape. In addition to the scientific component, the results of this study could be valuable inputs to policy makers, industry stakeholders and geoscientists for identifying mineral exploration targets in the region and thus contributing to sustainable development and resource security in the region.

1.5 Expected outcomes

a) Generation of comprehensive geochemical dataset detailing the elemental concentration of dolerite intrusions within Mansehra Granite.
b) Assessment of the overall mineral resource potential of the studied dolerite intrusions.

CHAPTER 2

LITERATURE REVIEW

2.1 Literature review

The geology of Mansehra, Hazara area is based on the geographical mapping and stratigraphy carried out in the middle of the twentieth century. The lithostratigraphic relationship of Hazara Basin was determined through some initial work by Calkins et al. (1975) who recognized some important units such as Tanawal Formation and the intrusive granitoids of Mansehra. These initial studies furnished the fundamental geological conceptualization on which the later tectonic and petrogenetic studies have been based. The western Himalaya tectonic syntheses highlighted the complicated interaction between thrust tectonics, crustal shortening and magmatism. The tectonic architecture of the larger area of northern Pakistan was outlined by Tahirkheli (1979) pointing out the meeting of the Indian plate and the surrounding Eurasian terrains.

Treloar and Izatt (1993) also discussed the structural development of the Himalayan collision zone and took the stacking of thrusts and crustal thickening as the main processes of orogenic evolution. DiPietro and Pogue (2004) gave a better tectonostratigraphic subdivisions and emphasized the role of localized shear zones in accommodating deformation and magmatic intrusion. In this scenario, Oghi Shear Zone was probably a structural control of the mafic dyke emplacement.

Studies of the Mansehra Granitic Complex like the Petrogenetic studies of the Mansehra Granitic Complex have centered on crustal melting and granitoid development. Geochronology based on U-Pb zircon confirms Early Paleozoic emplacement, and mineralogical and geochemical studies indicate peraluminous signatures and fractional crystallization evidence (Naeem et al., 2016, 2021).

The studies of REE bearing pegmatites related to the granitic complex have reported the local enrichment of incompatible elements, which revealed the mineral exploration potential of the granitic systems in the area (Mehmood et al., 2022).

Studies on dolerites in northern Pakistan have covered petrographic properties and engineering appropriateness in the first place. Ismaeel et al. (2019) described the Oghi, Mansehra region in detail according to petrographic and geochemical, and the dolerites were sub-alkaline to tholeiitic with ferroan character. Their research came up with correlations of mineralogical composition, especially the abundance of plagioclase with mechanical strength. Although this work greatly contributed to the knowledge of dolerite petrology and engineering properties, it also did not go to trace element systematics and critical mineral assessment. Similar mafic dykes along the Malka region (Majid et al., 1991) were explained as rift related intrusions which were deposited during Permian extensional processes along the northwestern Indian plate margin. These investigations show that mafic intrusions in northern Pakistan can document both extensional or post collisional tectonic events separate of previous granitoid emplacement. These tectonic changes may be followed by mantle metasomatism or partial melting processes which may affect distribution of trace elements. Internationally, mafic and ultramafic intrusions are well known to be the hosts of magmatic sulfide and REE mineralization. The mechanisms by which processes like sulfide immiscibility, crystal accretion, and late stage hydrothermal activity can produce economically viable concentrations of Ni, Cu, Co, and REEs are comprehensively described as magmatic ore systems (Naldrett, 2013; Robb, 2013). Even though the Oghi dolerites are not huge layered intrusions, their tectonic location within a collisional orogen implies that magmas of mantle origin reacting with crustal material could have undergone geochemical evolution that could have led to the formation of local enrichment.

Moreover, the studies of the alkaline and granitoid hosted systems of the REEs in north Pakistan (Hussain et al., 2020; Mehmood et al., 2022) prove the relevance of the ICP-MS based trace element analysis to assess the potential of mineralization. These methodological tools offer a sound analytical model which can be applied to dolerite intrusions.

Critical minerals underpin the global transition to renewable energy. Mafic to ultramafic intrusions globally, including the Bushveld Complex in South Africa and the Canadian Shield, have demonstrated their economic potential for REEs, Ni, and Co (Naldrett, 2013). Such global analogues highly suggests that the dolerite intrusions in northern Pakistan could also host critical minerals if systematically investigated.

2.2 Geology of study area

The Oghi region is situated in the Mansehra District of Khyber Pakhtunkhwa, Northern Pakistan, and forms an integral part of the broader Hazara geological domain within the western Himalayan fold and thrust belt. The area lies at the geologically complex junction of the Lesser Himalayan Zone and the hinterland of the western Himalaya, where Precambrian to Cenozoic rock sequences are extensively exposed, deformed, and intruded by igneous bodies of varying ages and compositions. The physiographic and geological character of the region has been shaped by a prolonged and multiphase tectonic history encompassing Precambrian sedimentation, Early Paleozoic magmatism, Mesozoic passive margin deposition, and Cenozoic collisional deformation associated with the convergence of the Indian and Eurasian plates (Calkins et al., 1975; Tahirkheli, 1979; DiPietro & Pogue, 2004).

The fundamental geological framework of the Mansehra Hazara area was established through the pioneering mapping and stratigraphic work of Calkins et al. (1975), whose U.S. Geological Survey Professional Paper on the geology of the southern Himalaya in Hazara, Pakistan, defined the major lithostratigraphic units of

the basin, recognized the Tanawal Formation and the intrusive granitoids of Mansehra as key elements of the Hazara succession, and laid the conceptual foundation for all subsequent tectonic and petrogenetic investigations in the region. The Hazara Basin, which encompasses the Mansehra area, represents a major synformal structure within the Lesser Himalayan Zone and is broadly divisible into two segments, the eastern Abbottabad Block and the western Tanawal Block, separated by the Panjal Khairabad Thrust, which functions as the Main Central Thrust equivalent in the western Himalaya (DiPietro & Pogue, 2004). The study area of Oghi lies within this structurally complex zone, where multiple thrust systems, mafic dyke swarms, and the granitic plutons of the Mansehra Granitic Complex collectively define a geologically diverse and economically prospective terrain.

The topography of the Oghi, Mansehra region is deeply dissected, with the Kunhar River and its tributaries incising through a succession of metamorphic and sedimentary rocks that range from Precambrian phyllites and quartzites to Eocene carbonates and Miocene molasse deposits. Dolerite dykes and sills intrude the older country rocks throughout the area and are particularly prominent along structural corridors, most notably the Oghi Shear Zone, which is interpreted as a key structural control on mafic magma emplacement in the region (DiPietro & Pogue, 2004). The broader tectonic setting is that of the western Himalayan hinterland, which extends north of the Panjal Khairabad Thrust for approximately 100 km to where metamorphic and intrusive Indian plate rocks truncate against the Main Mantle Thrust zone (DiPietro & Pogue, 2004), placing the Oghi, Mansehra intrusions firmly within the interior of the deformed Indian plate margin.

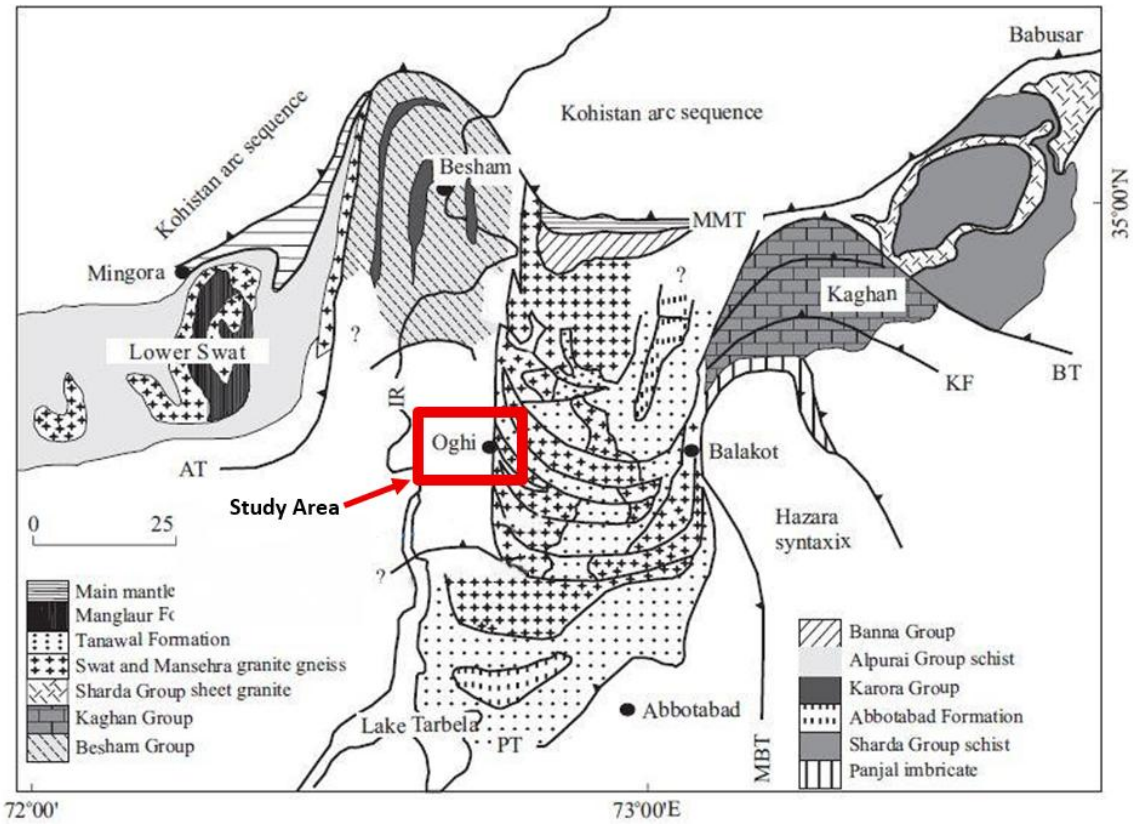


Figure 2.1 Geological map of the study area located south of the Main Mantle Thrust (MMT), spanning the region between the Swat and Kaghan valleys (after Treloar and Rex, 1990). Abbreviations: AT = Alpurai Thrust; BSZ = Balakot Shear Zone; BT = Batal Thrust; IR = Indus River; KF = Khannian Fault; MBT = Main Boundary Thrust; MMT = Main Mantle Thrust; PT = Panjal Thrust; TSZ = Thakot Shear Zone

2.3 Tectonostratigraphic divisions

The Himalaya is broadly divided into hinterland (metamorphosed) and foreland (unmetamorphosed) zones (Coward et al., 1986), with the hinterland comprising crystalline rocks and the foreland comprising stratified rock successions. The Karakoram Block forms the southern edge of the Eurasian plate in northern Pakistan and is bounded to the north by the Rushan-Pshart Suture Zone and to the south by the Main Karakoram Thrust (MKT); internally it is subdivided into the high-grade Karakoram Metamorphic Complex, the composite Karakoram Batholith

(Jurassic to Miocene), and the Northern Karakoram Sedimentary Terrane (Searle, 1991; Crawford & Searle, 1992; Searle et al., 1999; Tahirkheli, 1979). The MKT separates the Karakoram from the Kohistan-Ladakh Island arc and is a south-directed thrust suture formed during arc-continent collision in the Late Cretaceous (75–102 Ma) and India-Asia collision in the Early Miocene (55–50 Ma) along the Main Mantle Thrust to the south (Searle, 1991; Crawford & Searle, 1992; Searle et al., 1999). The Main Boundary Thrust (MBT), a NW-striking, NE-dipping structure formed between 15–18 Ma, separates Lesser Himalayan metasedimentary rocks from Sub-Himalayan molasse deposits and is prominently folded by the Hazara-Kashmir Syntaxis near Balakot, remaining seismically active today and forming the southern structural boundary of the Oghi-Mansehra domain (Baig & Lawrence, 1987; Bossart et al., 1988; Calkins et al., 1975; Meigs et al., 1995). The Main Central Thrust (MCT), which is equivalent to the Panjal-Khairabad Thrust in Pakistan, separates the Greater Himalayan Crystalline Sequence from the Lesser Himalayan Zone, splits the Hazara Basin into Abbottabad and Tanawal blocks, and marks the northern boundary of the region where the Oghi dolerites were emplaced (DiPietro & Pogue, 2004; Calkins et al., 1975; Qasim et al., 2018).

2.4 Hazara Region Tectonics and Stratigraphic Succession

2.4.1 Tectonic Framework of the Hazara Region

Hazara domain is characterized by Hazara-Kashmir Syntaxis (HKS), a large scale (>100 km) antiformal hairpin made up of folded MBT and Panjal Thrust developed on eastern side of Indus syntaxis. The HKS constitutes the easternmost limit of the western Himalayan tectonic domain and is bounded by the Jhelum-Balakot transverse fault, separating the western and central Himalayan structural domains (Bossart et al., 1988; Calkins et al., 1975; DiPietro and Pogue, 2004). It

developed through at least two distinct deformation phases: early NNE-SSW trending tight to isoclinal folds associated with penetrative cleavage; and later NW-verging asymmetric to overturned folds related to sinistral shear. These deformation phases resulted from the transition of Indian plate motion from translational to translational-cum-rotational during Miocene which accommodated crustal shortening by out of sequence reverse faults such as Balakot - Bagh fault, which was ruptured during Kashmir earthquake (Mw 7.6) in 2005 (Bossart et al., 1988). The regional tectonic framework was first recognized by Tahirkheli (1979) and was later refined by Searle et al., (1999). Treloar and Izatt (1993) interpreted three successive phases of collision, suturing of the Kohistan arc to Asia at ~100 Ma followed by India-Asia collision at ~55 Ma and India-Afghanistan collision during the Pliocene as controlling factors of progressive deformation documented in the Hazara domain. Later, DiPietro and Pogue (2004) reported Oghi Shear Zone as the major structural control on emplacement of mafic magmas in the region. The structural setting of Oghi area corresponds to the western limb of HKS where the fold axes trending NNE-SSW are offset and deflected to northwest with sinistral sense of shear and controlled the pathway for emplacement of dolerite dykes and sills into Precambrian Tanawal Formation.

2.5 Stratigraphy of study area

The stratigraphy of Oghi Mansehra area indicates a very long and complicated geological history dating back to the Precambrian period up to the Quaternary. The sequence of stratigraphy documents several stages of sedimentation, metamorphism, magmatism, deformation as well as erosion linked to regional tectonics and Himalayan tectonics. The Mansehra Granitic Complex is one of the different lithological units that are centrally located because of its large distribution, unique petrogenesis, and high mineral potential. Stratigraphy is an important component that requires a detailed comprehension of the evolution and mineralization processes of the study area geologically.

Table 2.1 Generalized Stratigraphy of Mansehra Region showing rock formations from Precambrian to the recent, with formation of interest highlighted in yellow (Awan et al., 2021)

Formation	Age	Description
Alluvium	Recent	Unconsolidated deposits of gravel, clay, and pebbles, etc
Siwaliks Group	Miocene to Pliocene	Sandstone, siltstone, clays, and conglomerates
Murree Formation	Early Miocene	Cyclic order of sandstone and shale with subordinate claystone and conglomerates
Kuldana Formation	Middle to Late Eocene	Siltstone and fine-grained sandstone
Chorgali Formation	Early Eocene	Siltstone and dolomitic limestone, calcareous shale
Margala Hill Limestone	Early Eocene	Limestone with subordinate greenish-grey shale
Patala Formation	Late Paleocene	Khaki shale and marl with subordinate sandstone and limestone
Lockhart Limestone	Early Paleocene	Massive, hard, and thick-bedded grey to medium grey nodular and flaggy limestone
Hangu Formation	Early Paleocene	Sandstone, laterite, bauxite, fireclay, and coal
Unconformity		
Mansehra Granite	Cambrian to Ordovician	Quartz alkali feldspar and sodium-rich plagioclase and accessory minerals are micas (muscovite and biotite). Xenolith present in some places.
Abbottabad	Cambrian	Chiefly dolomite, limestone, chert bands, and

Formation		black shale
Tanol Formation	Precambrian	Metasediments, phyllite, and quartzite schist
Hazara Formation	Precambrian	Slates with subordinate metasediments.

2.5.1 Precambrian to Recent

The Hazara Basin is underlain by the metamorphosed slates and phyllites of the Hazara Formation (Late Neoproterozoic), intruded by the Mansehra Granitic Complex (Calkins et al., 1975; Bossart et al., 1988; Naeem et al., 2016), followed by the metamorphosed slates and phyllites of the Tanawal Formation of the Neoproterozoic-Cambrian, which hosts the Mansehra Granite and the Oghi dolerites, and whose age was previously determined by Rb-Sr dating (Calkins et al., 1975; DiPietro & Pogue, 2004; Le Fort et al., 1980; Qasim et al., 2018), and the unconformable early Cambrian Abbottabad Formation of shallow marine limestones and dolomites with both Hyolithid and Cruziana trace fossils (Calkins et al., 1975; The sedimentation was resumed during the Late Triassic-Early Jurassic when the fluvial-marginal marine Datta Formation was deposited followed by the Middle-Late Jurassic carbonate-platform Samana Suk Formation, conformable, followed by the Late Jurassic-Early Cretaceous dysoxic-anoxic Chichali Formation with oolitic ironstones, disconformable, followed by the Late Cretaceous deep open-marine Kawagarh Formation that was deposited with increasing siliciclastic input towards the India-Asia collision (Hussain et al., 2024; Qasim et al., 2018). The Cenozoic sequence represents the transition from passive margin to collision zone and consists of transgressive Paleocene Hangu Formation, nummulitic Lockhart Formation, deepening Patala Formation, shallow-marine Margalla Hill Formation, increasingly siliciclastic Chorgali Formation, continental Kuldana Formation, and finally thick Early-Middle Miocene Murree molasse deposited by Himalayan-derived river

systems and deformed by the Main Boundary Thrust (Qasim et al., 2018; Meigs et al., 1995; Hussain et al., 2024), with the youngest being the Quaternary alluvial fans, terraces, and colluvium.

2.5.1.1 Mansehra Granitic Complex and Dolerite Dykes and Sills

The Mansehra Granitic Complex (MGC) of the early paleozoic in the region is the most volumetrically significant event, with a suite of peraluminous, calc alkaline, S type, granitoids intruding Hazara and Tanawal formations, age 466-478 Ma. Mansehra Granite, leucogranites associated with it, and Hakale Granite have crystallization ages of 478 Ma, 475 Ma, and 466 Ma respectively, respectively, respectively, by SHRIMP and LA-ICP-MS U-Pb zircon geochronology (Naeem et al., 2016). There are earlier ages of 83 Ma (K/Ar), 215 Ma (Ar/Ar on biotite) and 516 ± 16 Ma (Rb-Sr whole-rock) which have been assigned to resetting due to the effects of later thermal events (Naeem et al., 2016). The geochemically derived sediments of the MGC are peraluminous (A/CNK > 1.1), calc-alkaline, and have high initial $^{87}Sr/^{86}Sr$ ratios (0.7324–0.7444) and negative εNd(t) (−9.2 to −8.6), suggesting that they are derived from Neoproterozoic to Cambrian sedimentary protoliths with Paleoproterozoic ancestry in the basement (Naeem et al., 2016). It was emplaced in an Andean-type Cambro-Ordovician orogenic environment on the northern boundary of East Gondwana (Naeem et al., 2016).

The Dolerite Dykes and Sills (Permo-Triassic) cross the Precambrian Tanawal (Precambrian) Formation and are believed to be related to extensional tectonics of rifting of northern edge of Indian plate and formation of Neo-Tethys Ocean (Qasim et al., 2018). Widely distributed Permian mafic magmatism, in the Malka region, is supported by analogous mafic dykes developed as a result of lithospheric extension along the northwestern margin of the Indian plate. The dolerites have a fine to medium-grained fabric, are dark grey to greenish grey, and are subophitic to intergranular in texture and are found as concordant sills and discordant dykes along

structural corridors like the Oghi Shear Zone (DiPietro & Pogue, 2004) and in the Tanawal Formation. The vast majority of the intrusions are the focus of the present geochemical study.

CHAPTER 3

METHODOLOGY

3.1 Work methodology

A six stage workflow was followed to geochemically characterize the Dolerites from Oghi, Mansehra in this study. The first phase was fieldwork and sampling, during which 16 samples (SS1-SS16) were obtained from within the vicinity of Oghi area. The samples were then prepared through crushing, pulverizing, and homogenization processes before being analyzed by ICP-MS to determine the concentrations of critical minerals, including trace elements, uranium, phosphorus, REEs, and other base metals, as detailed in Chapter 4. Data was collected and compiled into a 16 sample data set during the data acquisition phase, and during the data interpretation phase, this data set was used to determine geochemical baselines for the formation. The last phase included the results and conclusions, which were designed to evaluate the critical mineral potential. This study follows the methodology as shown below;

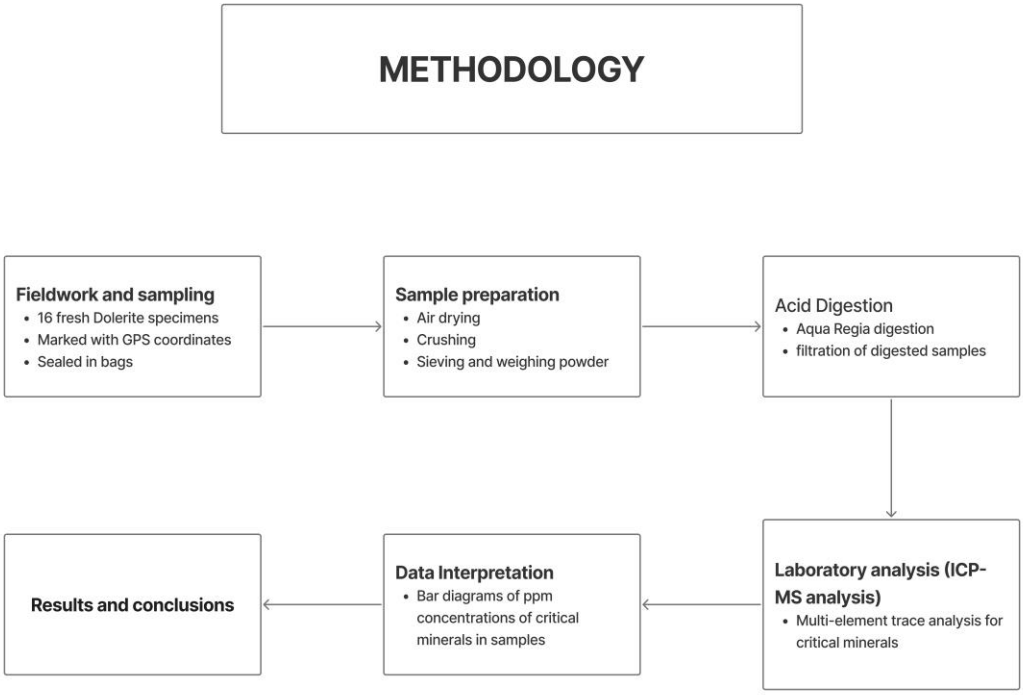


Figure 3.1 Adopted methodology for study

3.1.1 Fieldwork and Sampling

Sampling of Dolerite dykes in Oghi, Mansehra, Pakistan, Pakistan was conducted. This topic was selected due to the composition and its potential to host critical minerals. Fieldwork was carried out systematically to ensure that representative samples were collected from exposed outcrops. Field site was selected after careful evaluation of its suitability, accessibility, and degree of weathering, with preference given to minimally weathered locations. A total of sixteen (16) dolerite samples were collected from the outcrop, the were named as SS1-SS16. Fresh surfaces were targeted to minimize the effects of erosion and weathering. Prior to extraction, weathered layers were removed using a geological hammer and chisel. Each sample was weighed, with masses ranging between 500 g and 900 g. After labeling, samples were stored in clean, high density polyethylene bags to prevent

errors in identification. The use of non metallic containers helped minimize the risk of cross contamination during trace metal analysis. All samples were documented with GPS coordinates, lithological descriptions, and mineralogical observations. Field photograph was also taken to support site documentation and archiving.

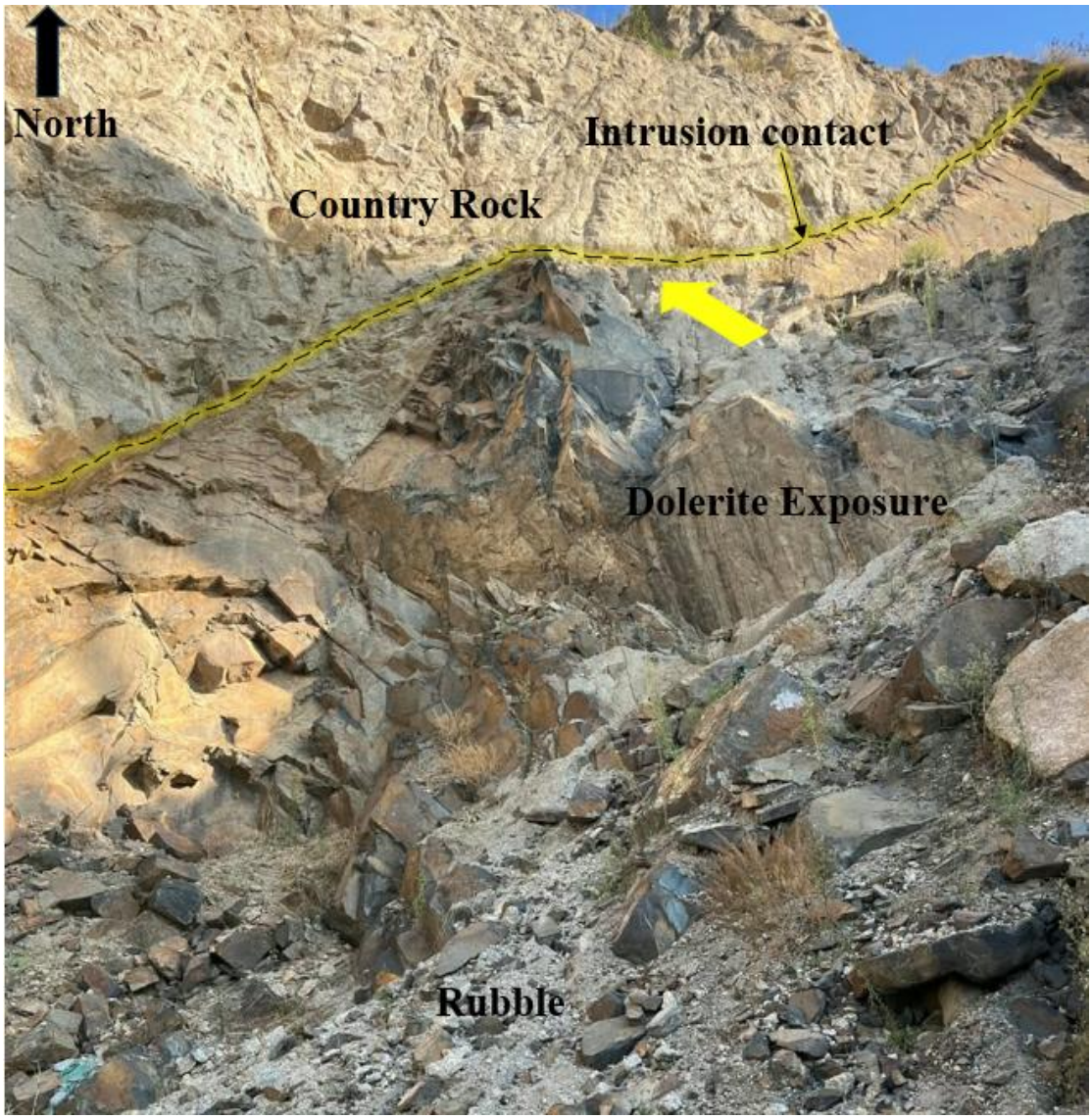


Figure 3.2 Outcrop of Dolerite at Oghi, Mansehra, from where sampling was done, intrusion contact between country rock and dolerite marked in yellow, North arrow for northing

Table 3.1 Coordinates of sample points

Sr. no	Name	Latitude	Longitude
1	SS1	34.463554	72.998195
2	SS2	34.463576	72.998152
3	SS3	34.463815	72.997981
4	SS4	34.463750	72.998033
5	SS5	34.463686	72.998127
6	SS6	34.463639	72.998220
7	SS7	34.463504	72.998113
8	SS8	34.463781	72.997970
9	SS9	34.463799	72.998290
10	SS10	34.463606	72.998440
11	SS11	34.463709	72.998390
12	SS12	34.463534	72.998246
13	SS13	34.463434	72.998119
14	SS14	34.463377	72.997989
15	SS15	34.463539	72.997938
16	SS16	34.463410	72.997580

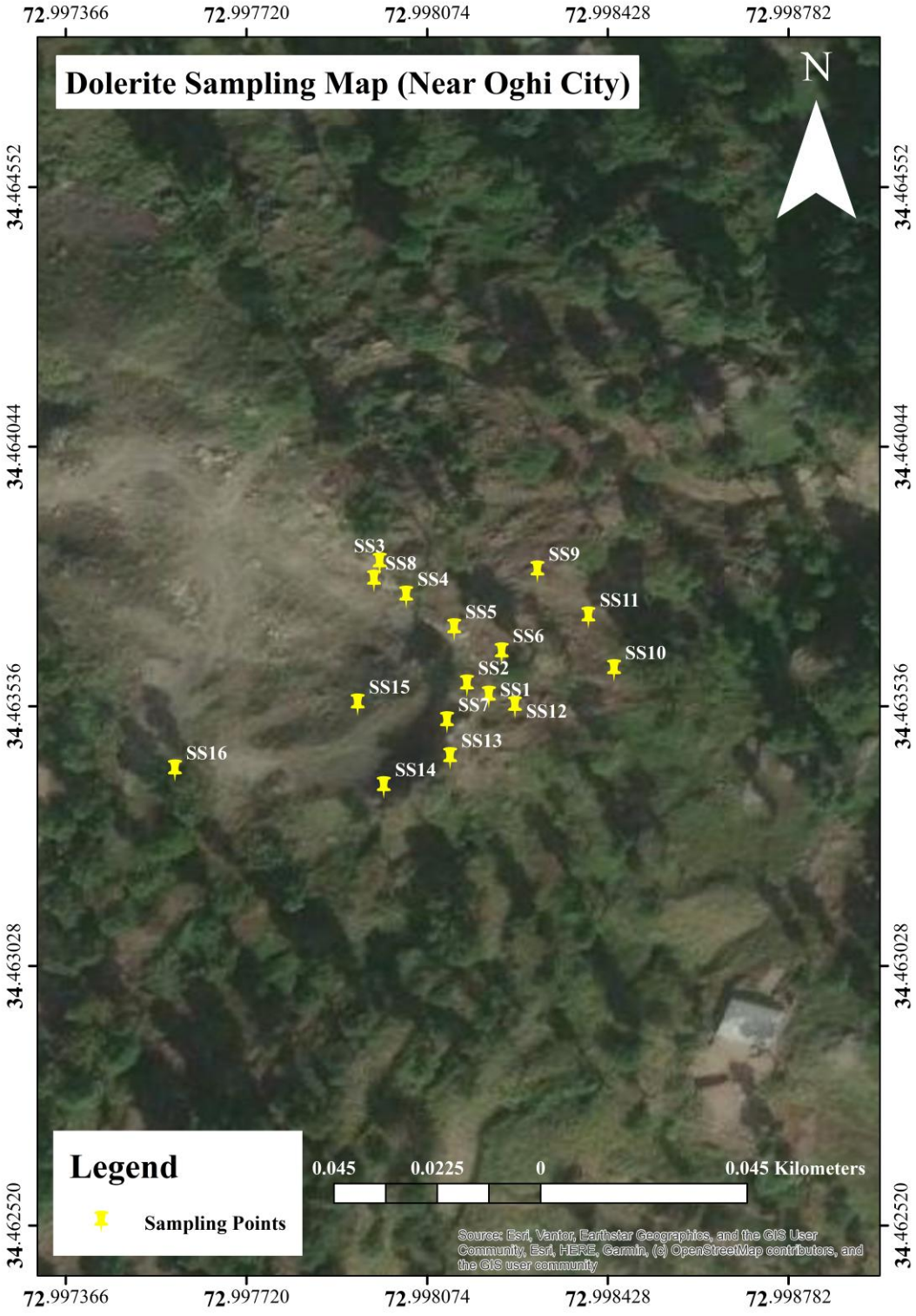


Figure 3.3 Dolerite sampling location map showing sampling points from where sampling was conducted highlighted in yellow along with labels (within the vicinity of Oghi city), (ArcMap 10.5)

3.1.2 Sample preparation

Solid samples were air dried at room temperature to remove residual moisture prior to further processing. Thermal drying was deliberately avoided to preserve volatile critical minerals, as elevated temperatures during sample preparation can result in the loss of volatile elements such as As, Hg, Pb, Ge, Sb, and Te, thereby compromising the accuracy of subsequent trace element analysis in accordance with (Totland et al., 1992). The dried samples were crushed and powdered, then sieved using 30 and 100 mesh screens to separate fine fractions. Reduction to fine powder fractions below 100 mesh (<150 μm) is a standard and well established procedure for geological sample preparation prior to geochemical analysis, ensuring sufficient sample homogeneity for representative sub sampling and accurate elemental quantification in line with (Taylor & Theodorakos, 2002; Potts, 1987). The retained fines were then weighed for subsequent acid digestion.

Geological materials play a crucial role in determining critical and trace elements using Inductively Coupled Plasma Mass Spectrometry (ICP-MS), which is the most widely applied technique for the precise and accurate multi-element analysis of rocks, minerals, ores, soils, and sediments owing to its low detection limits, wide dynamic range, and high sample throughput (Hall & Plant, 1992; Balaram, 2021). Sample digestion was performed using aqua regia, consisting of one third nitric acid (HNO_3) and two thirds hydrochloric acid (HCl) in concentrated form. Aqua regia is a well established partial digestion method routinely used for extracting major, minor, and trace elements, including base metals and platinum group elements from geological samples prior to ICP MS analysis; sample dissolution is generally recognized as the most critical and limiting step in the entire analytical workflow in line with procedure devised by (Totland et al., 1992; Jarvis & Jarvis, 1992).

All standard operating procedures (SOPs) were strictly followed during laboratory work. Protective equipment, including lab coats, gloves, goggles, and KN95 masks, was worn under the supervision of laboratory personnel. Glassware such as flasks, beakers, and spatulas were thoroughly cleaned with distilled water and

labeled using permanent markers to prevent fading during heating. Storage bottles for ICP-MS solutions were also cleaned with distilled water. Strict contamination control during sample preparation is essential for the integrity of trace element data at ppm (parts per million) concentrations in line with (Potts, 1987; Thomas, 2013).

After digestion, beakers were removed from the hot plate, and 30 ml of distilled water was added to dilute the concentrated solutions. The samples were then allowed to cool. The digestion process involved oxidation of metals by acids and the formation of stable soluble chloro complexes through reactions with chloride ions supplied by HCl, which is the primary dissolution mechanism of aqua regia procedurally done in accordance with (Totland et al., 1992);

$$3HCl + HNO3 \rightarrow NOCl + Cl2 + 2H2O$$

The solutions were initially filtered using standard filter paper and transferred to storage bottles. Subsequently, syringe filtration was performed to remove remaining total dissolved solids (TDS). Spectral and non-spectral interferences in ICP-MS measurements were minimized through the use of internal standards and matrix-matched external calibration procedures, following established SOPs to ensure analytical accuracy and minimize contamination throughout in accordance to (Balaram, 2021; Jarvis & Jarvis, 1992; Thomas, 2013).



Figure 3.4 Weighing balance used for fines



Figure 3.5 Heating sample solution for digestion of specimen fines in acid

.



Figure 3.6 Sample filtration process



Figure 3.7 Syringe filtration processes

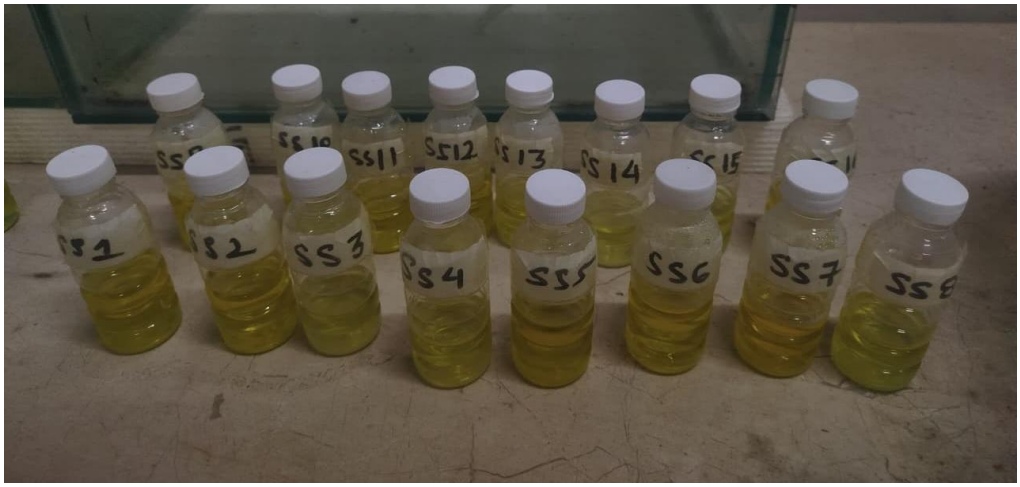


Figure 3.8 Final digested samples in bottles

3.1.3 Inductively Coupled Plasma Mass Spectrometry (ICP-MS)

3.1.3.1 Components of ICP-MS

Inductively Coupled Plasma Mass Spectrometry (ICP-MS) is a highly sensitive analytical technique used for determining major, minor, and trace elements in geological samples. It is particularly suitable for geochemical studies involving elements that are difficult to detect due to their low concentrations or small atomic sizes (Jarvis et al., 1992). In this study, ICP MS was used to measure elemental concentrations in acid digested rock samples. ICP MS enables multi element analysis through sequential processes that include aerosol formation, plasma ionization, ion extraction, mass separation, and detection. During analysis, liquid samples are converted into fine aerosols through nebulization and introduced into an argon plasma generated by a radiofrequency field. The plasma temperature ranges between 6,000 and 10,000 K, which is sufficient for complete desolvation, atomization, and ionization of most elements, allowing them to form singly charged ions (Thomas, 2013).

3.1.3.2 Working principle of ICP-MS

Ionization efficiency depends on plasma temperature and the ionization potential of individual elements, with low ionization potential elements being more readily ionized (Becker, 2007). Plasma generation occurs within a quartz torch surrounded by a copper induction coil, producing a stable high energy environment that supports ion formation (Jarvis et al., 1992). The resulting ions are extracted through sampler and skimmer cones, which reduce pressure and facilitate ion transfer (Becker, 2007). Mass separation is achieved using a quadrupole mass analyzer, which rapidly scans a wide range of mass to charge ratios, enabling simultaneous detection of multiple elements (Thomas, 2013). Ion signals are amplified by an electron multiplier detector, allowing detection of trace elements at sub parts per million and billion levels (Jarvis et al., 1992). Despite its high sensitivity, ICP MS is susceptible to spectral and non spectral interferences. These are minimized through correction procedures and the use of internal standards (Jarvis & Jarvis, 1992; Thomas, 2013). Quantification is achieved through external calibration, while quality control measures are applied to ensure analytical accuracy (Potts, 1987).

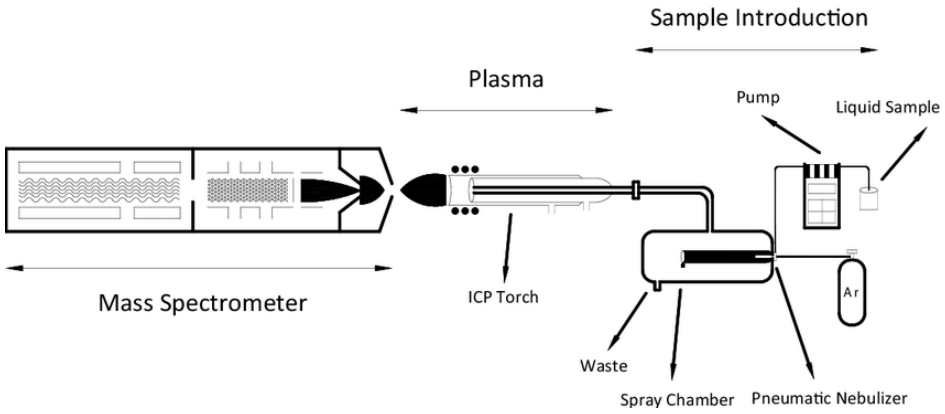


Figure 3.9 Schematic Diagram of ICP-MS (Kashani & Mostaghimi, 2010)

CHAPTER 4

RESULTS AND INTERPRETATION

4.1 Dataset

The dataset comprises 16 dolerite samples (SS1–SS16) from Oghi, Mansehra, analyzed by Inductively Coupled Plasma Mass Spectrometry (ICP MS). A total of 68 elements were observed across all samples in parts per million (ppm). Three qualitative designations appear; BDL (Below Detection Limit), ADL (Above Detection Limit, elevated beyond the calibration range), and ODL (Over Detection Limit). The USGS Final 2025 List of Critical Minerals (Federal Register, November 7, 2025) identifies 60 critical minerals, of which 56 are represented by measured elements in this dataset. Elements not on the 2025 list constitute the Other Minerals section.

4.2 Critical Minerals

4.2.1 Aluminum (Al)

Aluminum was detected in all 16 samples with a concentration range of 0.1401–3.3752 ppm and a mean of approximately 0.8760 ppm. The highest Al was recorded in SS5 (3.3752 ppm), followed by SS1 (2.7603 ppm) and SS2 (2.1388 ppm), while the lowest values occurred in SS10 (0.1401 ppm), SS16 (0.1660 ppm), and SS14 (0.1787 ppm). The nearly 24 fold range from SS10 to SS5 is the largest absolute spread among any universally detected element in the dataset, pointing to strong compositional heterogeneity across the intrusion.

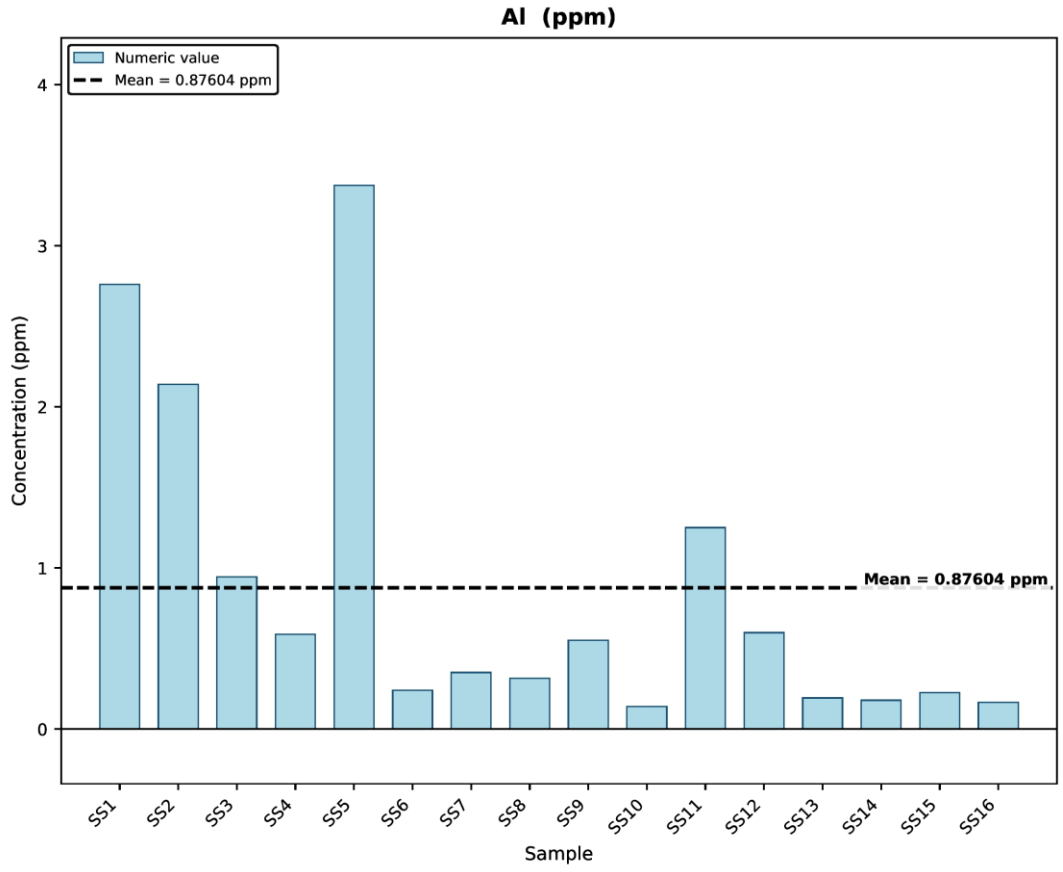


Figure 4.1 Aluminum values observed in samples

4.2.2 Antimony (Sb)

Antimony was detected in 12 out of 16 samples. SS1 (0.0790 ppm), SS2 (0.0588 ppm), SS5 (0.0837 ppm), SS6 (0.0900 ppm), SS7 (0.0821 ppm), SS8 (0.0548 ppm), SS9 (0.0833 ppm), SS10 (0.0342 ppm), SS11 (0.0532 ppm), SS12 (0.0778 ppm), SS15 (0.0660 ppm), and SS16 (0.0567 ppm), remaining BDL in SS3, SS4, SS13, and SS14. The highest Sb was recorded in SS6 (0.0900 ppm), while the lowest detectable value appeared in SS10 (0.0342 ppm). The broad and relatively consistent detection of Sb across 12 samples, combined with a relatively narrow concentration range in the detecting samples, suggests that Sb is a widely distributed across the Oghi dolerites rather than being concentrated in discrete zones.

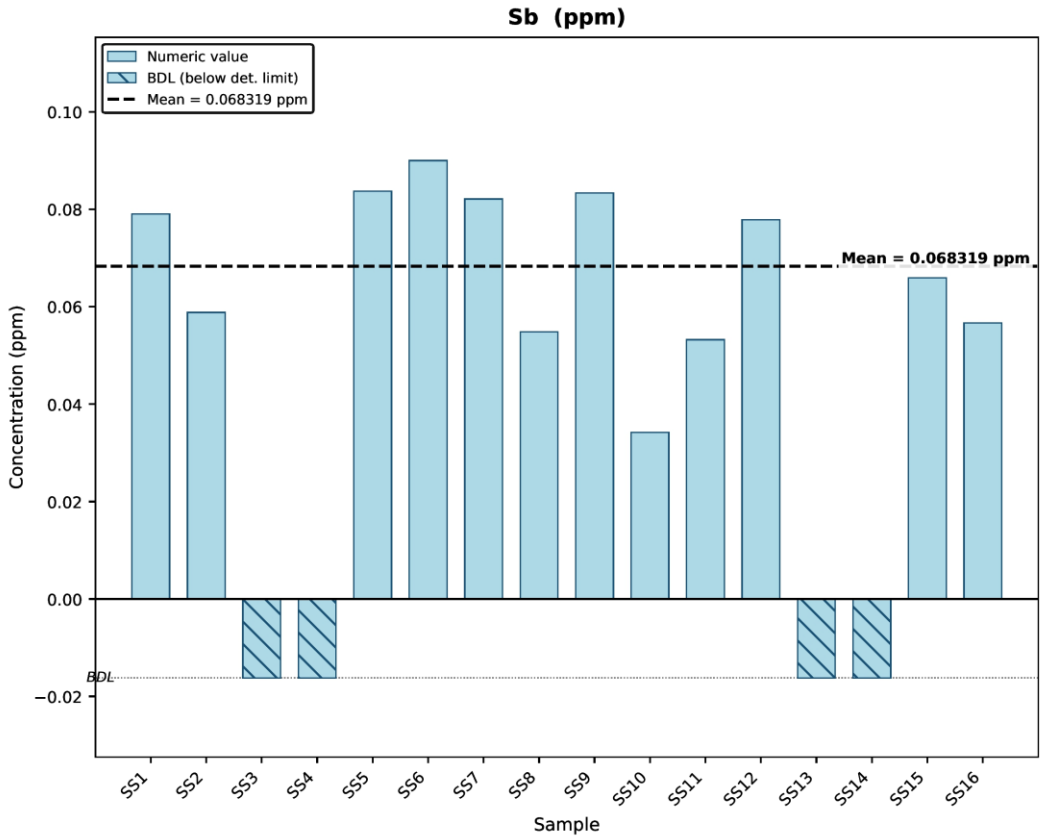


Figure 4.2 Antimony values observed in samples

4.2.3 Arsenic (As)

Arsenic was detected in only 1 out of 16 samples. SS5 (0.2487 ppm), remaining BDL in all other samples including SS1 through SS4 and SS6 through SS16, representing a highly localized, anomalous occurrence rather than a suite-wide signal.

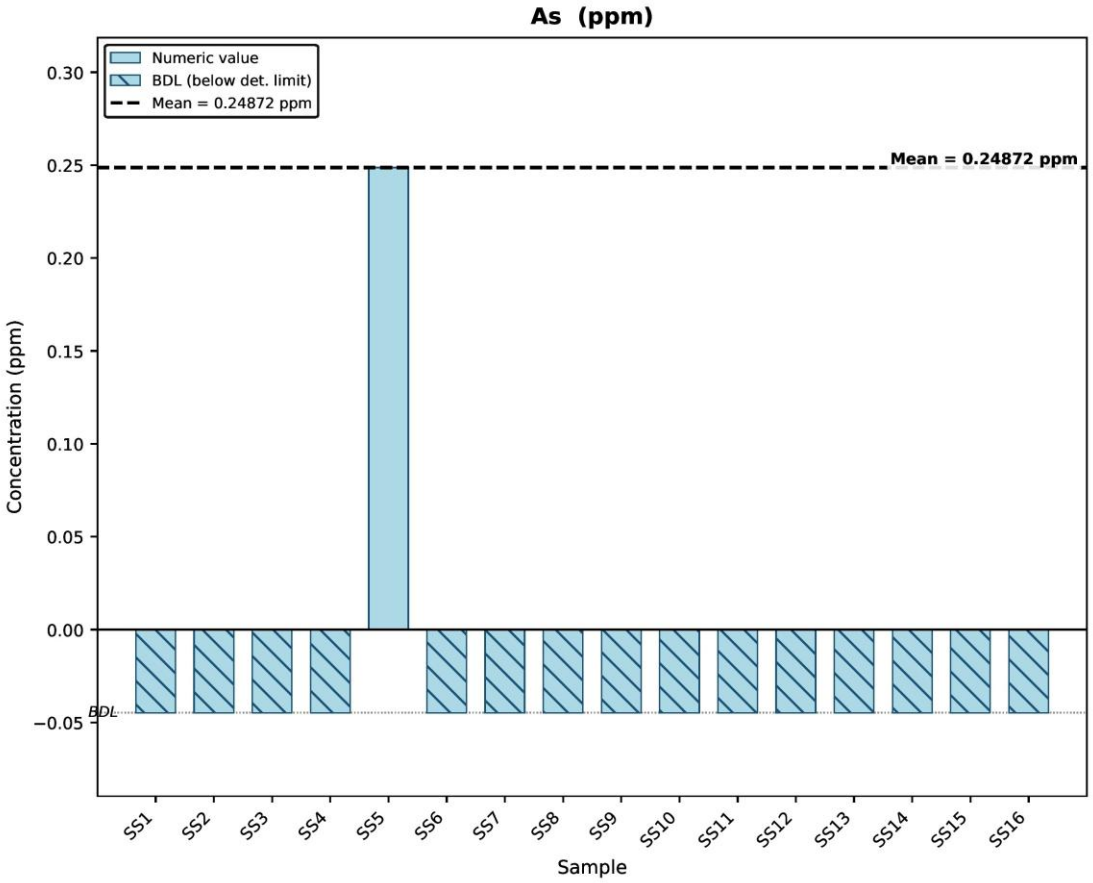


Figure 4.3 Arsenic values observed in samples

4.2.4 Barite (Ba)

Barium was detected in all 16 samples with a concentration range of 0.0007–0.0740 ppm and a mean of approximately 0.0203 ppm. The highest Ba was recorded in SS11 (0.0740 ppm), followed by SS1 (0.0481 ppm) and SS12 (0.0390 ppm), while the lowest values occurred in SS10 (0.0007 ppm), SS15 (0.0007 ppm), and SS14 (0.0041 ppm). The universal detection of Ba across all samples from SS1 to SS16, combined with the high Ba in SS11, reflecting a widespread background enrichment overprinted by localized enrichment.

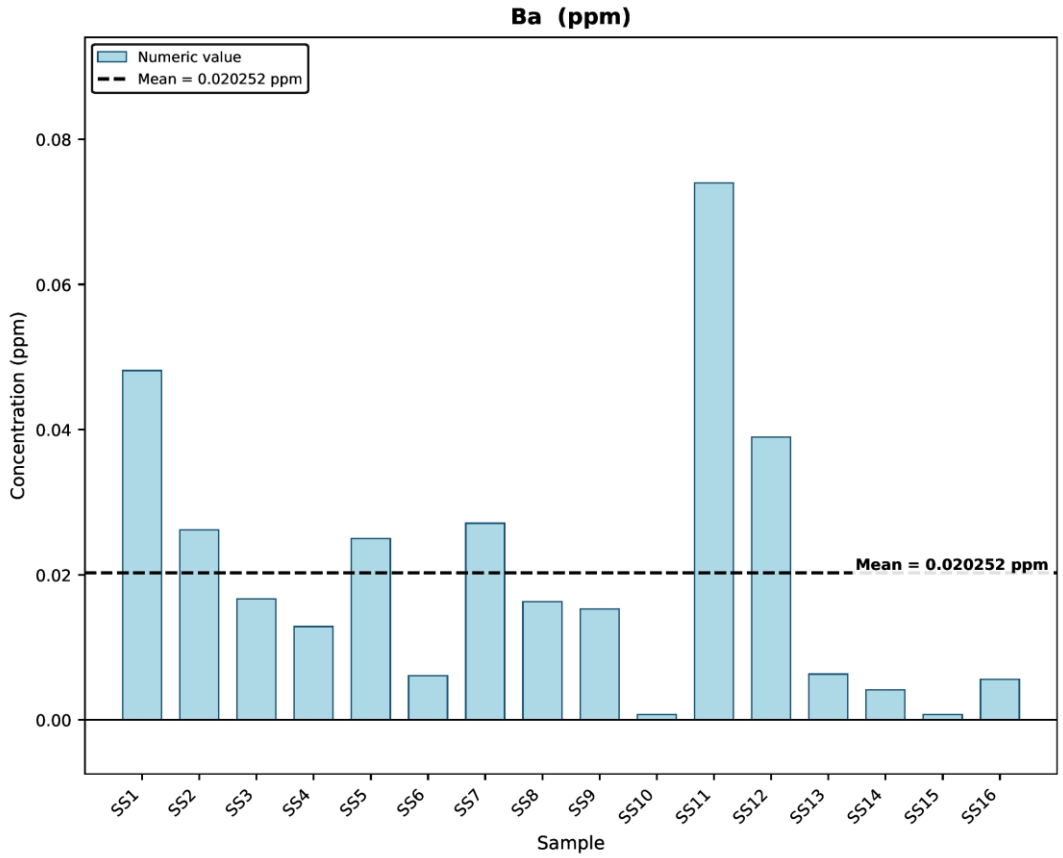


Figure 4.4 Barite values observed in samples

4.2.5 Beryllium (Be)

Beryllium was detected in all 16 samples with a concentration range of 0.0006–0.0023 ppm and a mean of approximately 0.0012 ppm. The highest Be was recorded in SS12 (0.0023 ppm), followed by SS11 (0.0017 ppm) and SS1 (0.0015 ppm), while the lowest values occurred in SS15 (0.0006 ppm), SS6 (0.0008 ppm), and SS10 (0.0009 ppm). The universal detection of Be across all 16 samples at extremely narrow concentrations ranging only from 0.0006 to 0.0023 ppm is consistent with a uniformly distributed trace Be signature throughout the intrusive body.

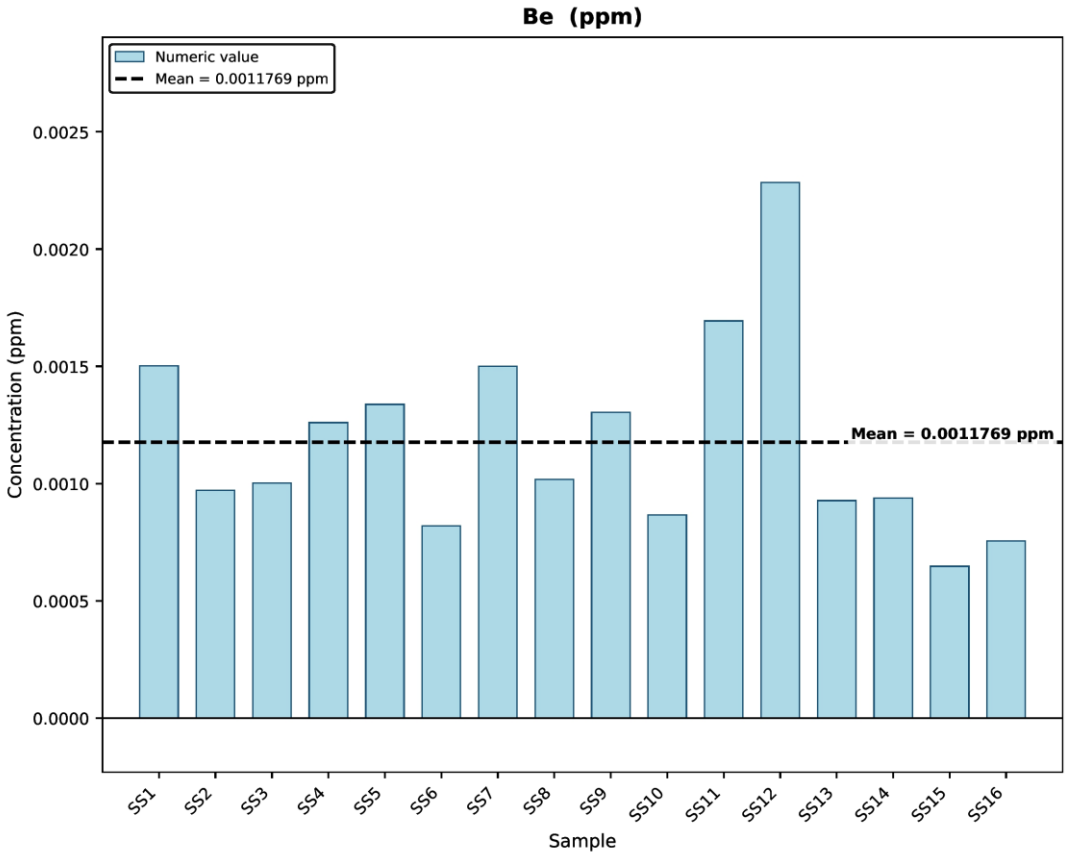


Figure 4.5 Beryllium values observed in samples

4.2.6 Bismuth (Bi)

Bismuth remained BDL across all 16 samples SS1 through SS16 without exception. The complete absence of detectable Bi across the entire suite confirms the absence of any significant Bi bearing phases in the Oghi dolerites, consistent with their primary mafic igneous origin without significant hydrothermal Bi mineralization.

4.2.7 Boron (B)

Boron was detected in 11 out of 16 samples. SS1 (0.1596 ppm), SS2 (0.0510 ppm), SS3 (0.0298 ppm), SS5 (0.0630 ppm), SS6 (0.0071 ppm), SS7 (0.0227 ppm), SS8 (0.0153 ppm), SS9 (0.0322 ppm), SS11 (0.0450 ppm), SS12 (0.0357 ppm), and SS15 (0.0126 ppm), remaining BDL in SS4, SS10, SS13, SS14, and SS16. The highest B was recorded in SS1 (0.1596 ppm), more than three times higher than the second highest value in SS5 (0.0630 ppm), while the lowest detectable value appeared in SS6 (0.0071 ppm). The anomalously high B in SS1, combined with the BDL status in SS4, SS10, SS13, SS14, and SS16, suggests heterogeneous fluid rock interaction across the sample suite, with SS1 having experienced either greater hydrothermal alteration or greater incorporation of B bearing fluids than the other samples.

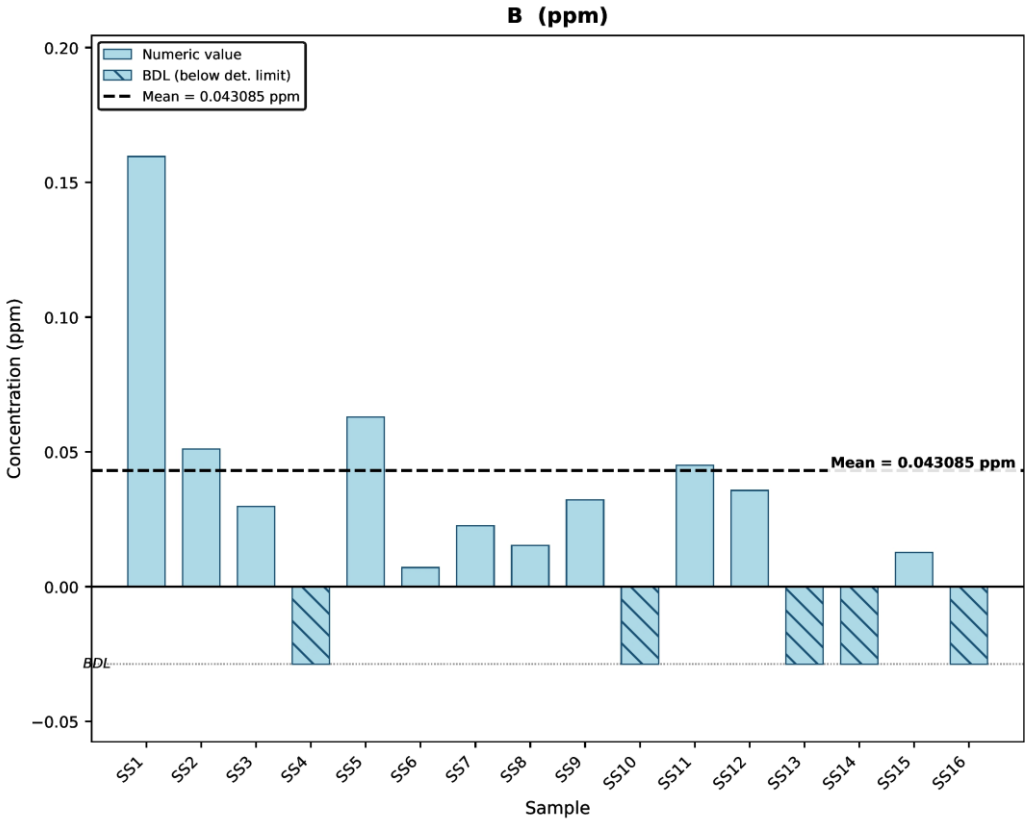


Figure 4.6 Boron values observed in samples

4.2.8 Cerium (Ce)

Cerium was detected in 13 out of 16 samples, remaining BDL in SS3, SS5, and SS13, with a concentration range of 0.0132–0.0928 ppm and a mean of approximately 0.0405 ppm. The highest value was recorded in SS8 (0.0928 ppm), followed by SS16 (0.0616 ppm), SS4 (0.0544 ppm), and SS1 (0.0455 ppm), while the lowest detectable value occurred in SS15 (0.0132 ppm), widespread LREE presence with no single dominant control identified.

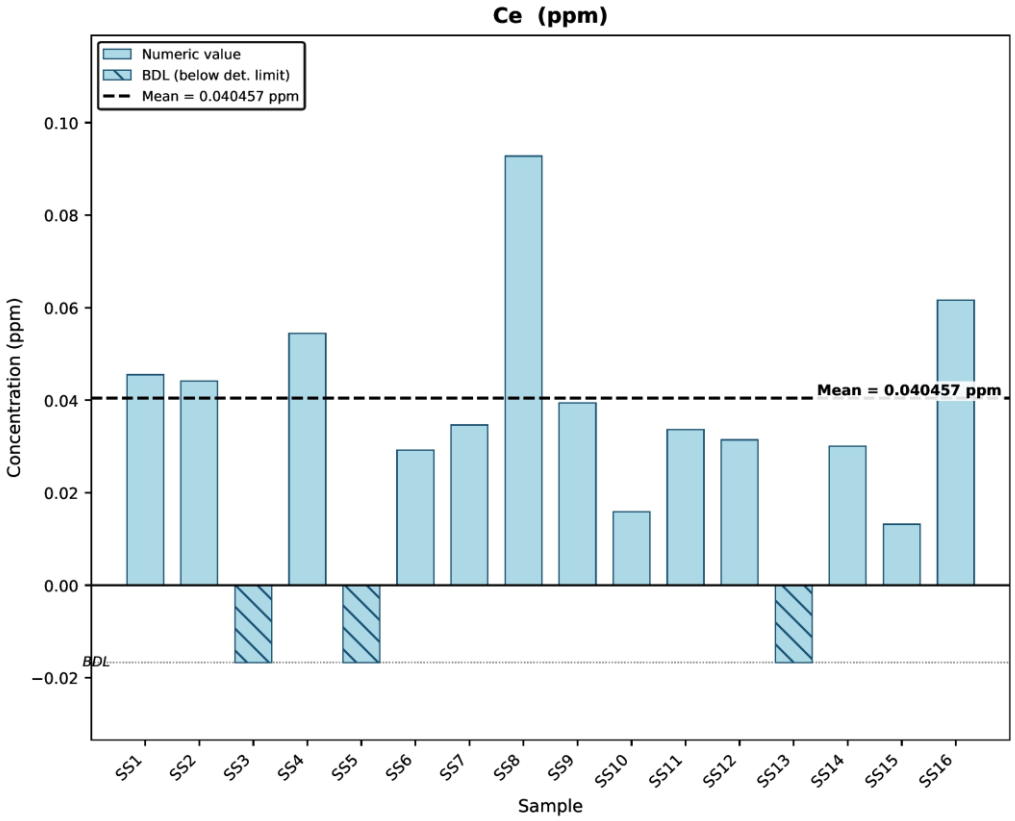


Figure 4.7 Cerium values observed in samples

4.2.9 Chromium (Cr)

Chromium was detected in only 5 out of 16 samples. SS1 (0.0590 ppm), SS2 (0.0085 ppm), SS5 (0.0317 ppm), SS9 (0.0240 ppm), and SS12 (0.0032 ppm), remaining BDL in SS3, SS4, SS6, SS7, SS8, SS10, SS11, SS13, SS14, SS15, and SS16. The highest Cr was recorded in SS1 (0.0590 ppm), followed by SS5 (0.0317 ppm) and SS9 (0.0240 ppm), while the lowest detectable value appeared in SS12 (0.0032 ppm), indicating patchy retention or loss during crystallization/alteration.

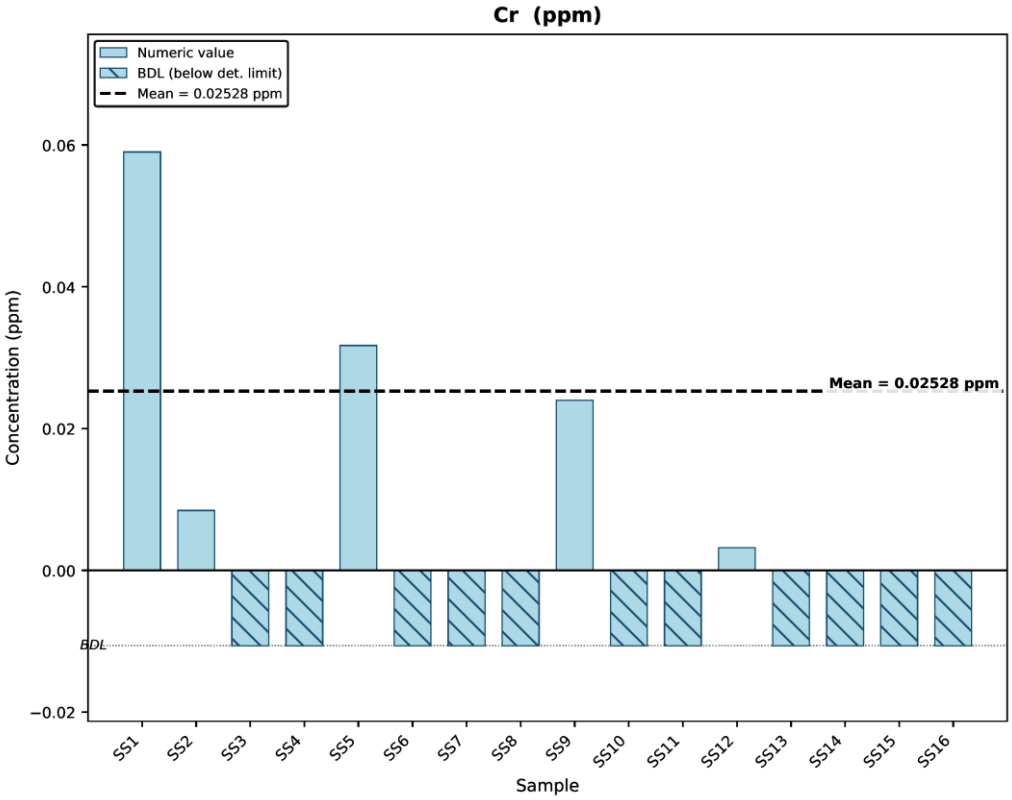


Figure 4.8 Chromium values observed in samples

4.2.10 Cobalt (Co)

Cobalt remained BDL across all 16 samples, SS1 through SS16 without exception. The complete absence of detectable Co across the entire suite is one of the more geochemically unexpected results given that Co is typically a compatible element in mafic systems.

4.2.11 Copper (Cu)

Copper was detected in all 16 samples with a concentration range of 0.0512–0.5458 ppm and a mean of approximately 0.2386 ppm. The highest Cu was recorded in SS5 (0.5458 ppm), followed by SS1 (0.4496 ppm) and SS2 (0.3766 ppm), while the lowest value occurred in SS14 (0.0512 ppm). The universal detection of Cu across all 16 samples, from the most mafic (SS1) to the most depleted (SS14) makes Cu one of the most pervasive geochemical signals in the entire dataset.

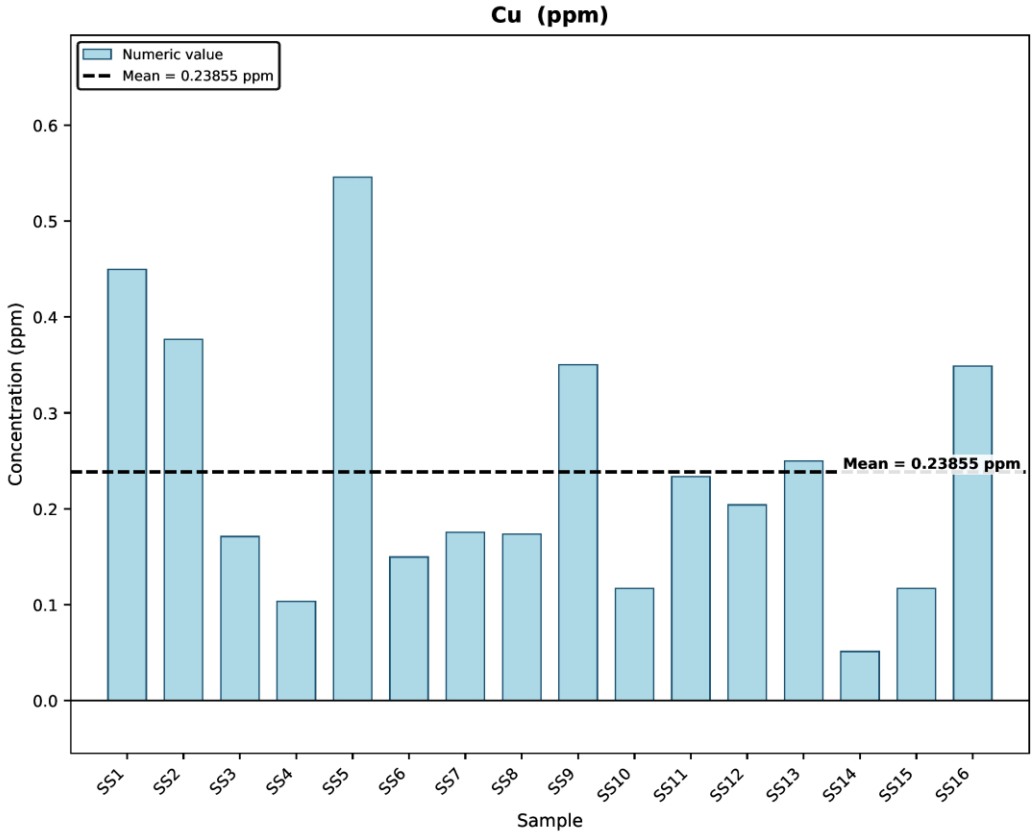


Figure 4.9 Copper values observed in samples

4.2.12 Dysprosium (Dy)

Dysprosium was detected in 15 out of 16 samples, remaining BDL only in SS14, with a concentration range of 0.0010–0.0180 ppm and a mean of approximately 0.0060 ppm. The highest value was observed in SS10 (0.0180 ppm), followed by SS7 (0.0096 ppm) and SS13 (0.0089 ppm), while the lowest detectable value appeared in SS1 (0.0010 ppm), indicating broad but variable HREE distribution.

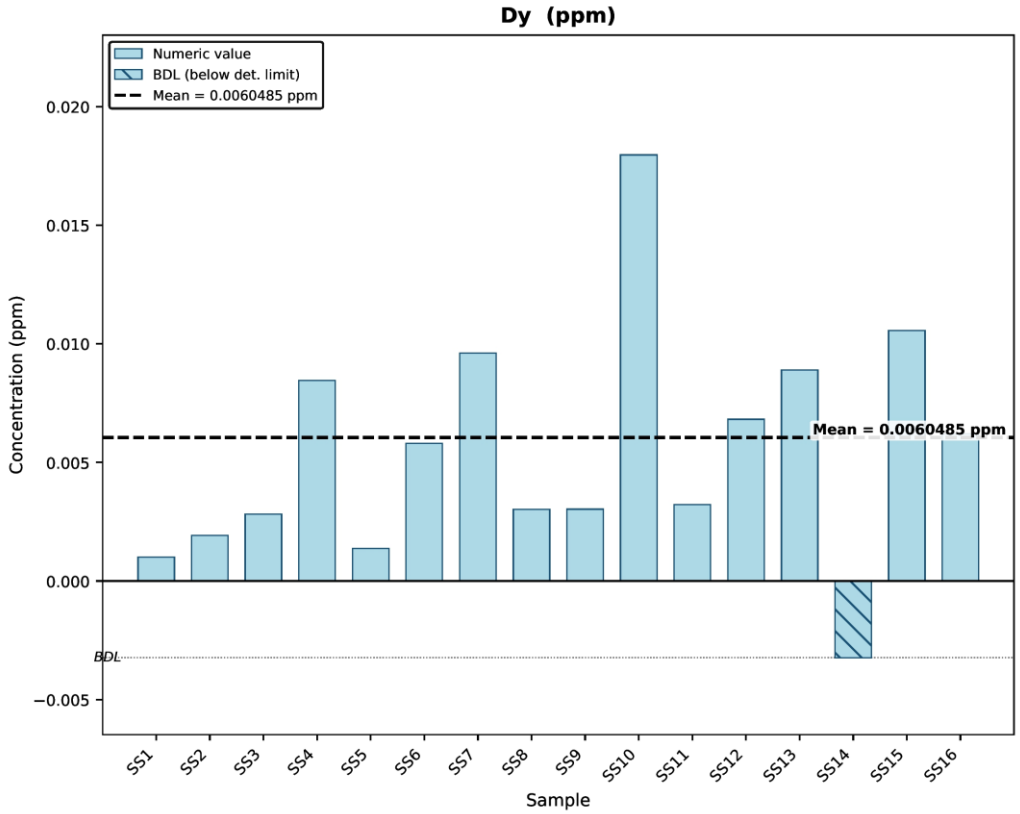


Figure 4.10 Dysprosium values observed in samples

4.2.13 Erbium (Er)

Erbium was detected in only 3 out of 16 samples. SS2 (0.0038 ppm), SS8 (0.0034 ppm), and SS7 (0.0018 ppm) remaining BDL in the remaining 13 samples including SS1, SS3, SS4, SS5, SS6, SS9, SS10, SS11, SS12, SS13, SS14, SS15, and SS16, reflecting a highly restricted HREE occurrence.

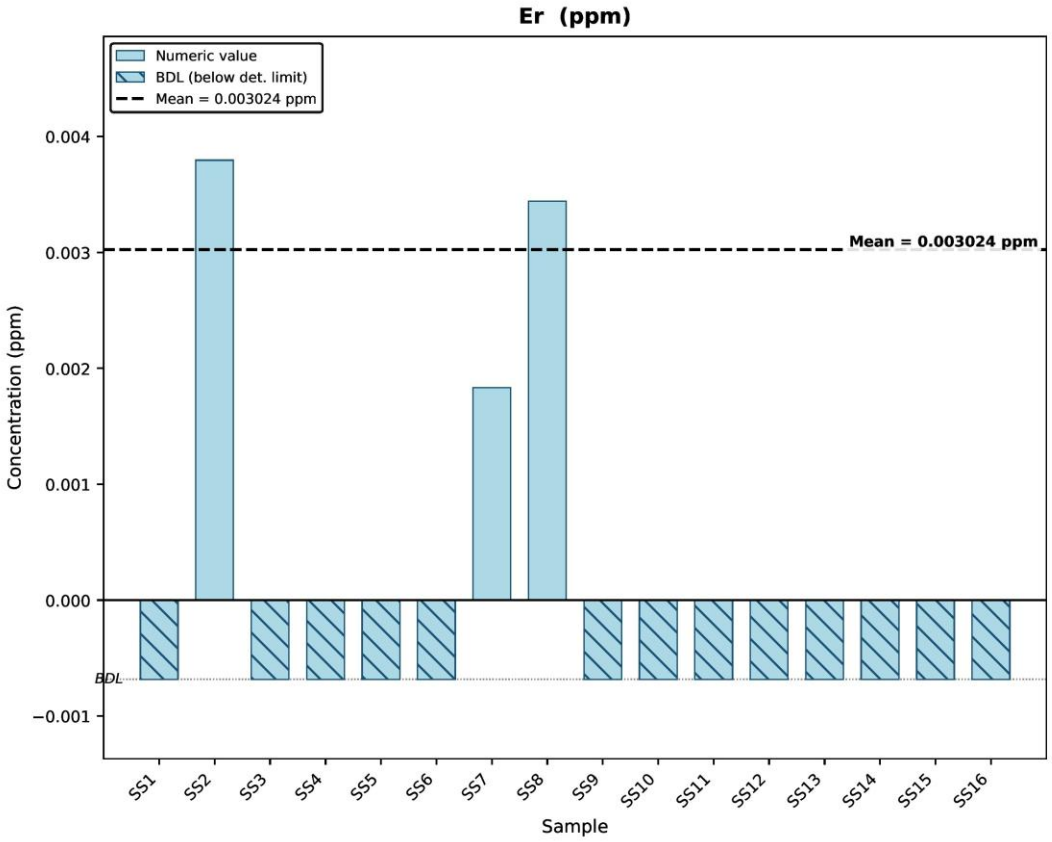


Figure 4.11 Erbium values observed in samples

4.2.14 Europium (Eu)

Europium was detected in all 16 samples with a concentration range of 0.0025–0.0078 ppm and a mean of approximately 0.0043 ppm. The highest value was recorded in SS12 (0.0078 ppm), followed by SS5 (0.0058 ppm) and SS3 (0.0053 ppm), while the lowest values were found in SS10 (0.0025 ppm) and SS15 (0.0027 ppm). The universal detection of Eu across all 16 samples, from SS1 through SS16 is one of the most consistent patterns and distinguishes Eu from all other REEs in the dataset. This near uniform distribution across the entire sample suite points to a stable and uniform incorporation of Eu throughout the crystallization history of the intrusive body.

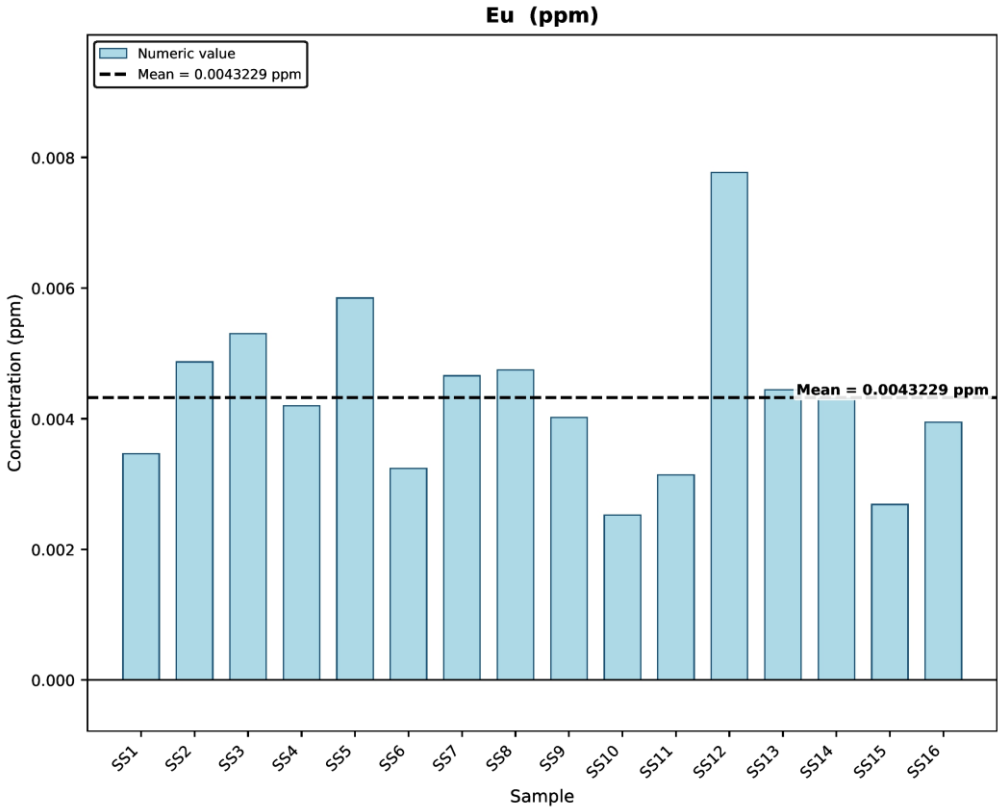


Figure 4.12 Europium values observed in samples

4.2.15 Gadolinium (Gd)

Gadolinium was detected in all 16 samples with a concentration range of 0.0052–0.0480 ppm and a mean of approximately 0.0169 ppm. The highest value was recorded in SS1 (0.0480 ppm), followed by SS5 (0.0284 ppm) and SS2 (0.0226 ppm), while the lowest value occurred in SS8 (0.0052 ppm), moderate variability with no dominant single-sample control highlighted.

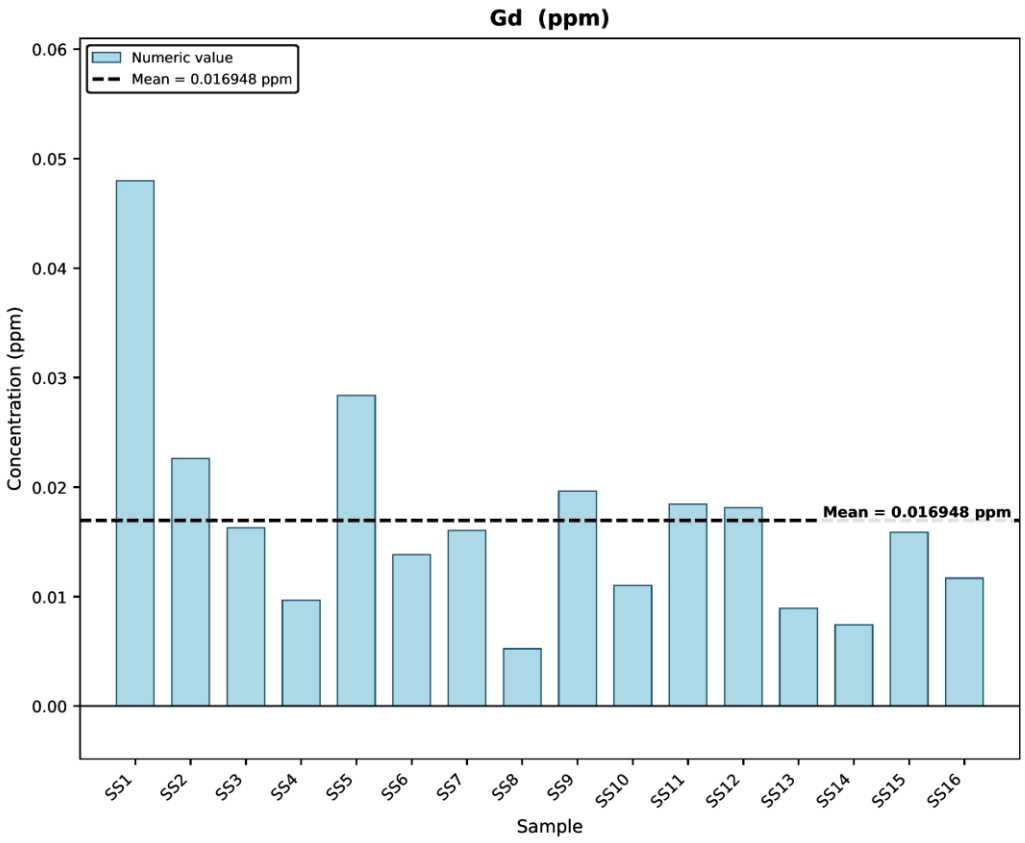


Figure 4.13 Gadolinium values observed in samples

4.2.16 Gallium (Ga)

Gallium was detected in 15 out of 16 samples, remaining BDL only in SS6, with a concentration range of 0.0285–0.1310 ppm and a mean of approximately 0.0897 ppm. The highest Ga values were recorded in SS7 (0.1310 ppm), SS4 (0.1306 ppm), and SS16 (0.1131 ppm), while the lowest detectable value occurred in SS10 (0.0285 ppm). Ga is among the most consistently and abundantly detected critical minerals in the entire dataset, with its near universal presence and relatively elevated concentrations clearly reflecting the Al-rich composition of these dolerites. SS5 records the highest Al (3.3752 ppm) and also a high Ga (0.0512 ppm), though the Ga-Al relationship is not strictly linear across all samples, suggesting that additional factors modulate Ga distribution within the suite.

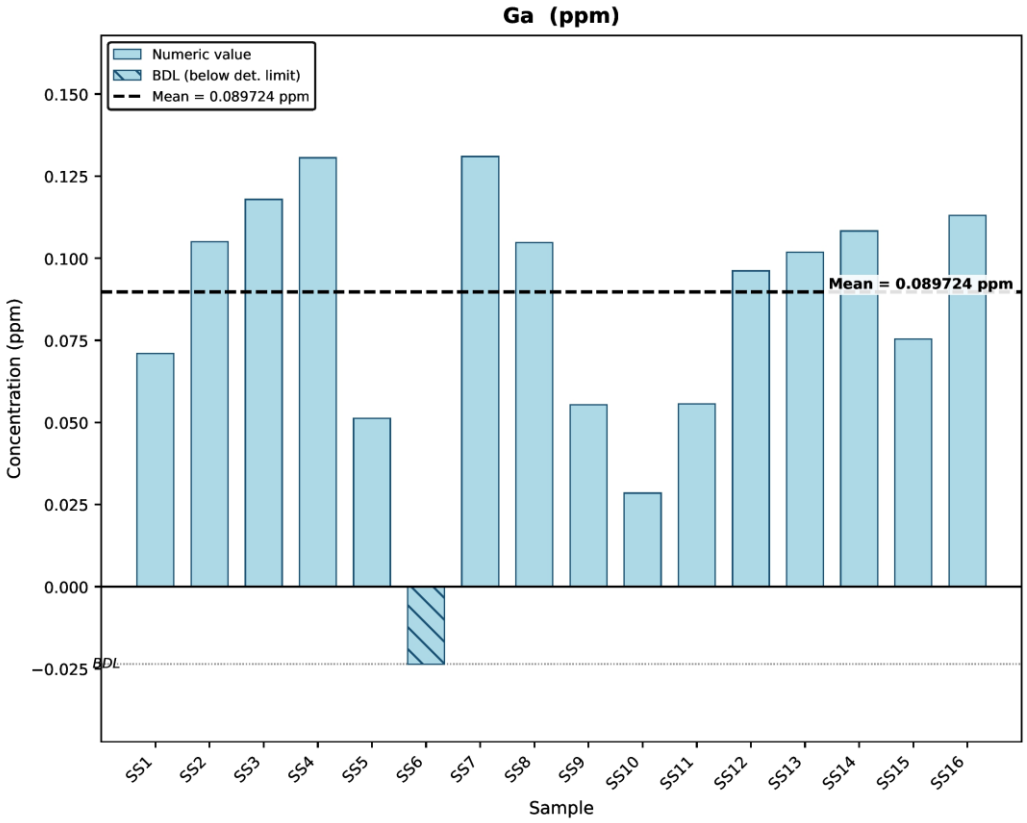


Figure 4.14 Gallium values observed in samples

4.2.17 Germanium (Ge)

Germanium was detected in only 2 out of 16 samples. SS8 (0.0502 ppm) and SS10 (0.0793 ppm), remaining BDL in all 14 other samples including SS1 through SS7, SS9, SS11 through SS16. The highest Ge value was recorded in SS10 (0.0793 ppm), which is also notable for having one of the lowest Al (0.1401 ppm), Mg (0.0060 ppm), and Mn values in the suite.

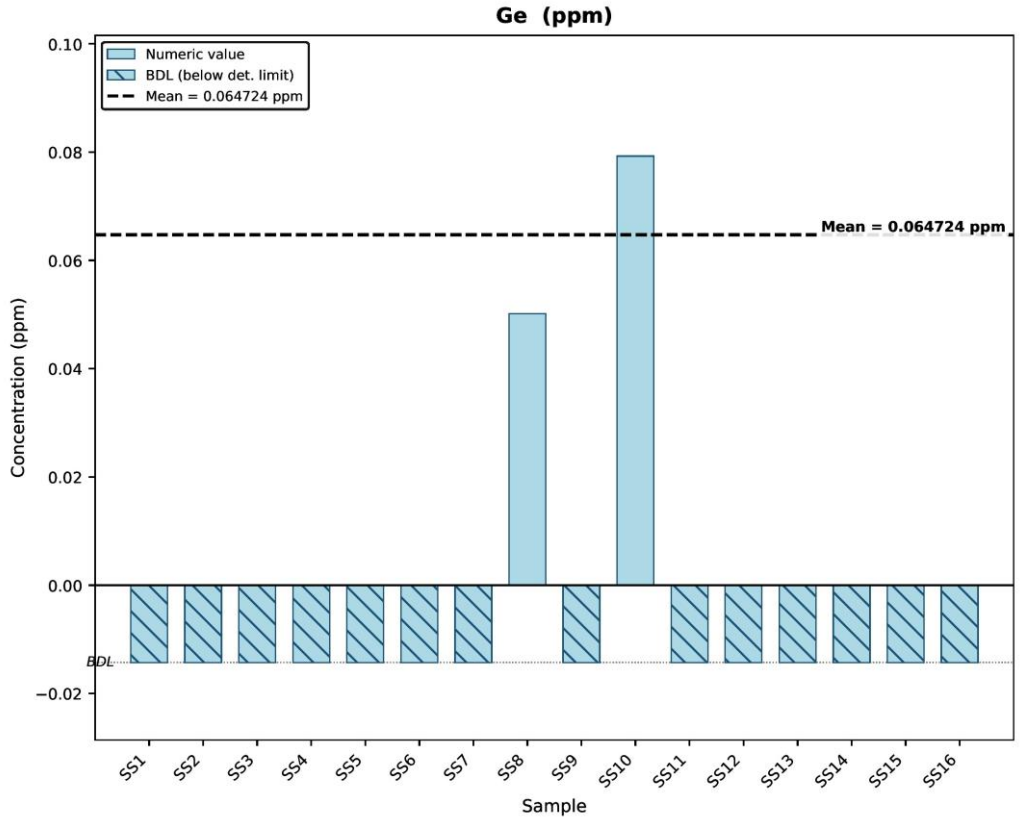


Figure 4.15 Germanium values observed in samples

4.2.18 Hafnium (Hf)

Hafnium was detected in 7 out of 16 samples. SS1 (0.0047 ppm), SS5 (0.0023 ppm), SS6 (0.0061 ppm), SS8 (0.0020 ppm), SS9 (0.0077 ppm), SS12 (0.0043 ppm), and SS13 (0.0064 ppm), remaining BDL in SS2, SS3, SS4, SS7, SS10, SS11, SS14, SS15, and SS16. The highest Hf value was recorded in SS9 (0.0077 ppm), followed by SS6 (0.0061 ppm) and SS13 (0.0064 ppm), while the lowest detectable value appeared in SS8 (0.0020 ppm). The detection of Hf in just 7 samples confirms that the Hf bearing phase, if any, is distributed sporadically throughout the intrusive body.

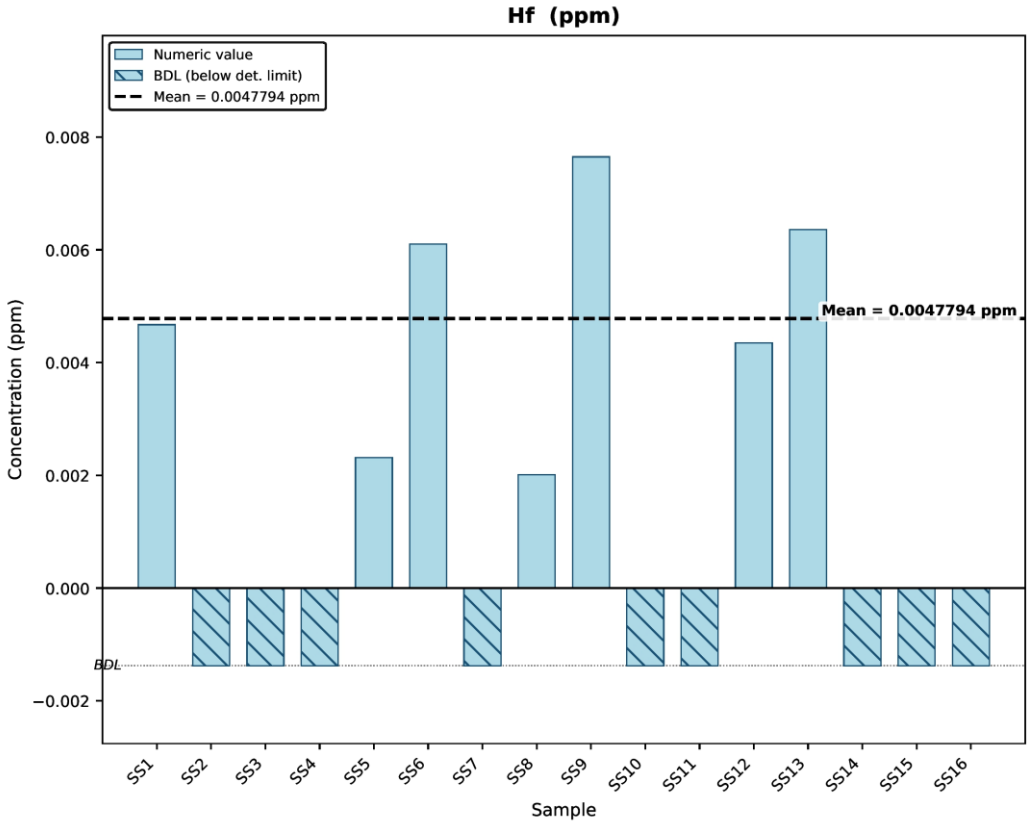


Figure 4.16 Hafnium values observed in samples

4.2.19 Holmium (Ho)

Holmium was detected in 10 out of 16 samples. SS3 (0.0066 ppm), SS4 (0.0053 ppm), SS6 (0.0116 ppm), SS7 (0.0078 ppm), SS10 (0.0087 ppm), SS11 (0.0040 ppm), SS12 (0.0079 ppm), SS14 (0.0113 ppm), SS15 (0.0088 ppm), and SS16 (0.0057 ppm), remaining BDL in SS1, SS2, SS5, SS8, SS9, and SS13. The highest value was recorded in SS6 (0.0116 ppm) and SS14 (0.0113 ppm), while the lowest detectable value appeared in SS11 (0.0040 ppm), a moderately widespread but variable HREE signal.

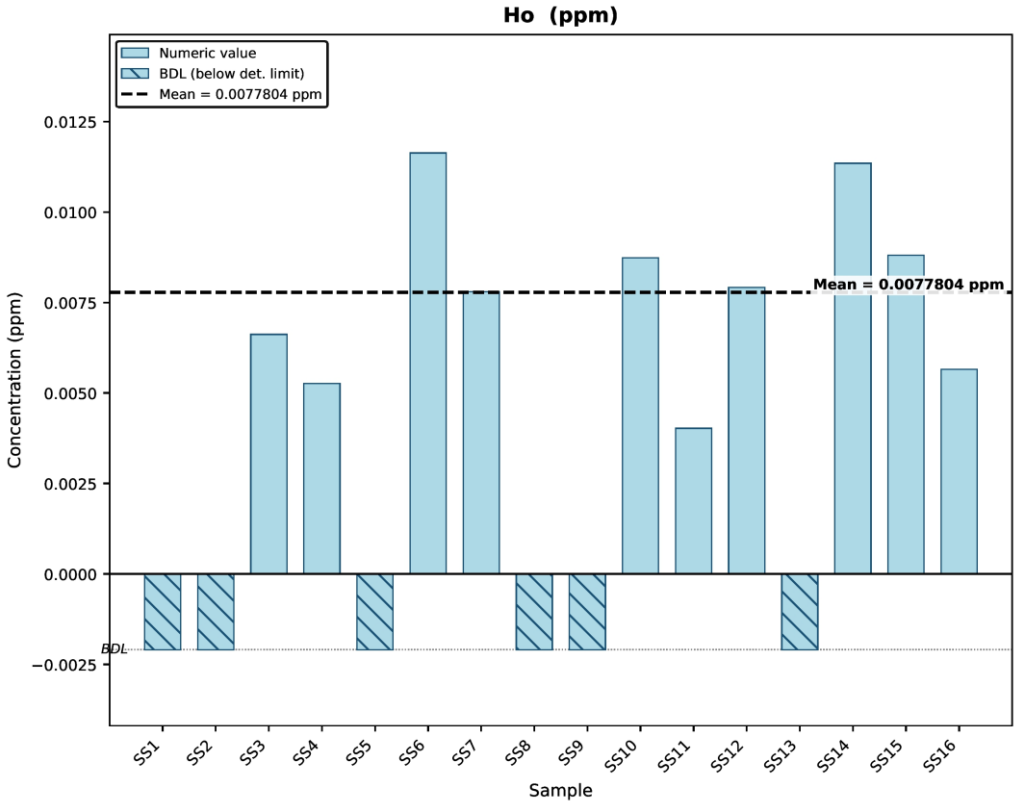


Figure 4.17 Holmium values observed in samples

4.2.20 Indium (In)

Indium remained BDL across all 16 samples, SS1 through SS16 without exception. The complete absence of detectable In across the entire sample suite is consistent with its geochemical behavior as a dispersed element typically concentrated in zinc sulfide deposits. Its universal BDL status throughout all 16 samples confirms the absence of any significant In mineralization in the Oghi dolerites.

4.2.21 Iridium (Ir)

Iridium was detected in 6 out of 16 samples. SS4 (0.0156 ppm), SS5 (0.0180 ppm), SS8 (0.0150 ppm), SS13 (0.0108 ppm), SS14 (0.0087 ppm), and SS16 (0.0126 ppm), remaining BDL in SS1, SS2, SS3, SS6, SS7, SS9, SS10, SS11, SS12, and SS15. The highest Ir value was recorded in SS5 (0.0180 ppm), the same sample that also records the highest Cu, As, and Al values, and the lowest Ag and Pd values in the dataset. The detection of Ir in scattered, non consecutive samples SS4, SS5, SS8, SS13, SS14, SS16, without a clear spatial trend suggests heterogeneous PGE distribution within the intrusive body, likely related to patchy sulfide or oxide crystallization across different zones of the dolerite.

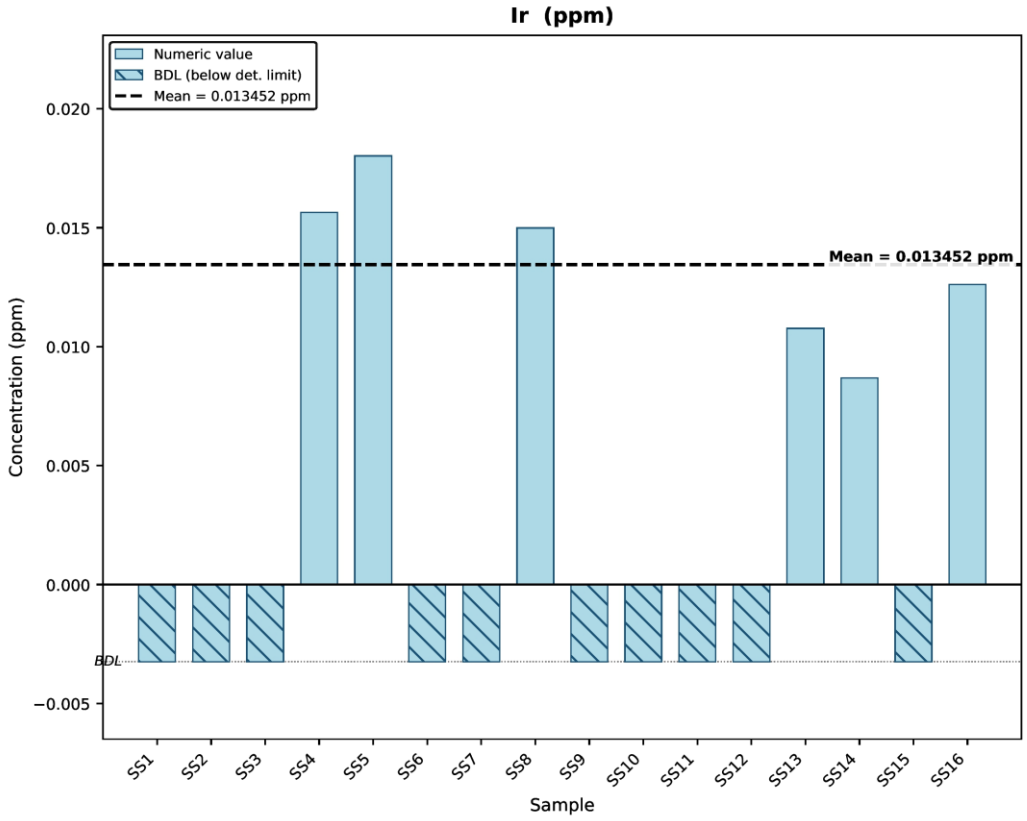


Figure 4.18 Iridium values observed in samples

4.2.22 Lanthanum (La)

Lanthanum was detected in only 4 out of 16 samples. SS1 (0.0025 ppm), SS10 (0.0030 ppm), SS11 (0.0059 ppm), and SS12 (0.0031 ppm), remaining BDL in SS2, SS3, SS4, SS5, SS6, SS7, SS8, SS9, SS13, SS14, SS15, and SS16. The highest La value was recorded in SS11 at (0.0059 ppm), reflecting restricted LREE occurrence.

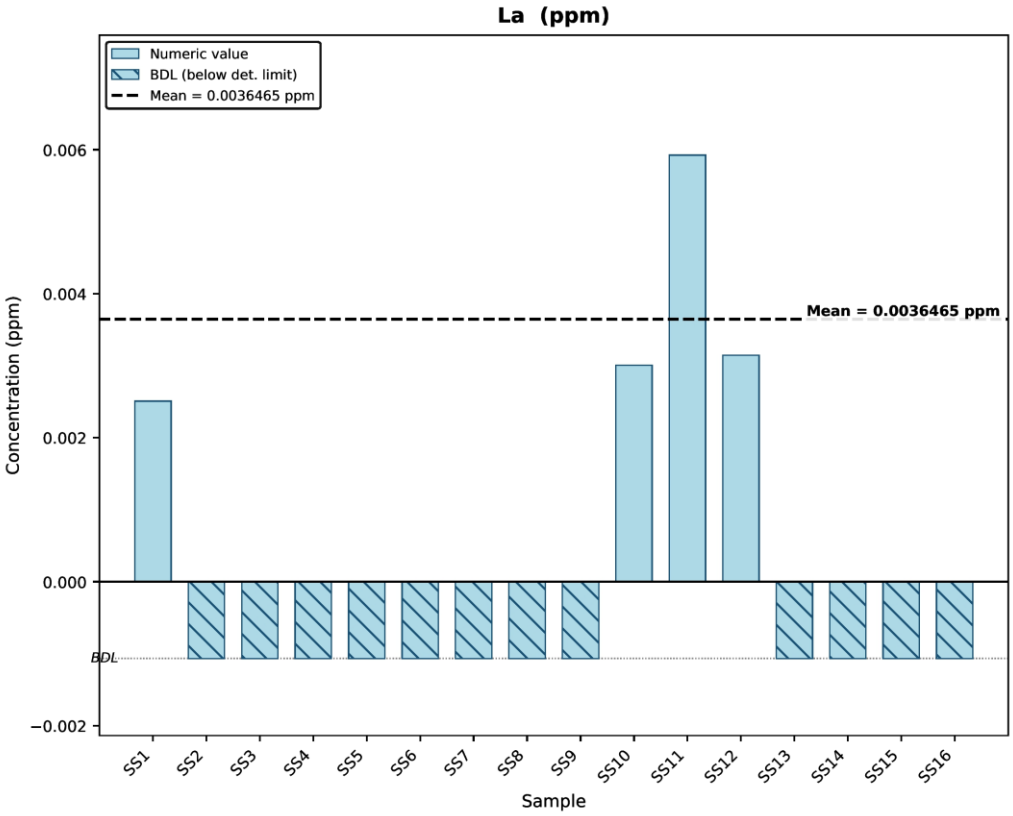


Figure 4.19 Lanthanum values observed in samples

4.2.23 Lead (Pb)

Lead remained BDL across all 16 samples, SS1 through SS16, without exception. The universal absence of detectable Pb across the entire sample suite is consistent with the primary mafic igneous origin of these dolerites, as Pb is an incompatible element that typically concentrates in felsic melts and hydrothermal systems rather than in primary mafic intrusions.

4.2.24 Lithium (Li)

Lithium was detected in all 16 samples with a concentration range of 0.0049–0.0565 ppm and a mean of approximately 0.0186 ppm. The highest Li values were recorded in SS1 (0.0565 ppm) and SS11 (0.0534 ppm), while the lowest values occurred in SS10 (0.0049 ppm) and SS14 (0.0086 ppm). The universal detection of Li across all samples from SS1 through SS16 makes it one of the most consistently present critical minerals in the dataset. The notably elevated Li in SS1 and SS11 compared to other samples, with SS1 also recording the highest values for Mg, Mn, V, Gd, Lu, Ru, and several other elements, suggests that SS1 represents the most compositionally enriched sample within the suite, potentially reflecting a more primitive or less fractionated mafic composition.

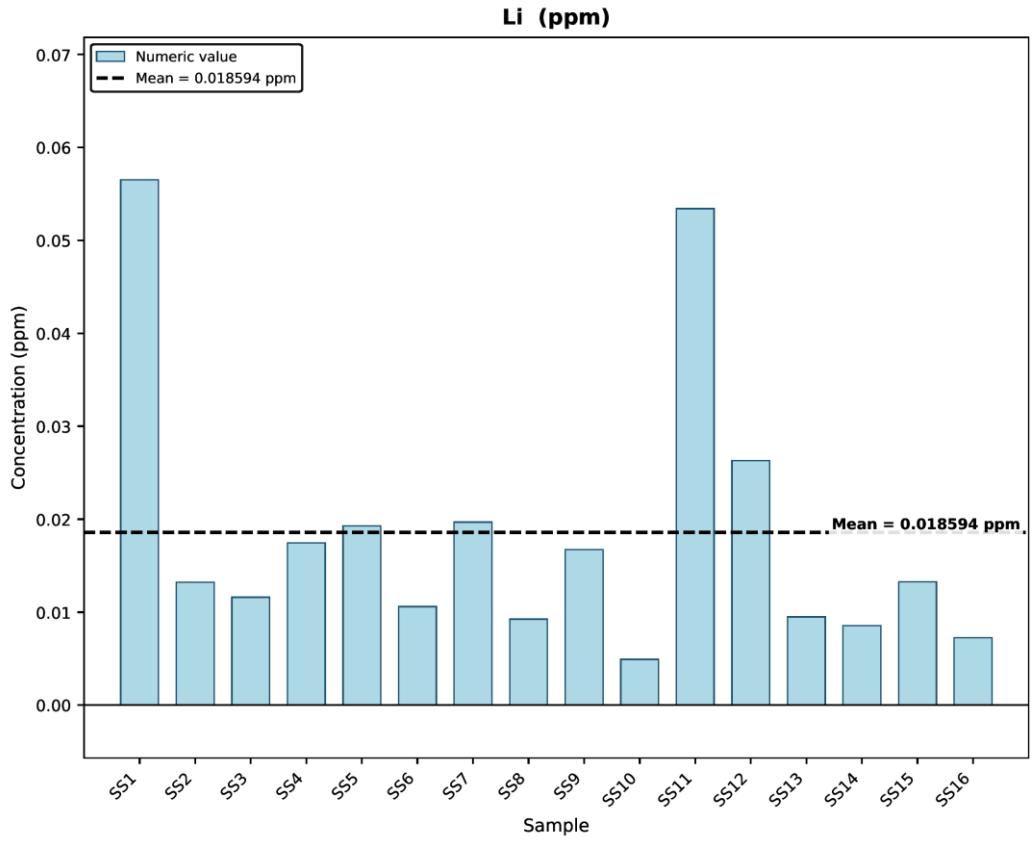


Figure 4.20 Lithium values observed in samples

4.2.25 Lutetium (Lu)

Lutetium was detected in 13 out of 16 samples, remaining BDL in SS10, SS14, and SS16, with a concentration range of 0.0008–0.0070 ppm and a mean of approximately 0.0026 ppm. The highest Lu value was recorded in SS1 (0.0070 ppm), followed by SS3 (0.0036 ppm) and SS9 (0.0035 ppm), while the lowest detectable value appeared in SS4 (0.0008 ppm), a moderately widespread HREE with SS1 standing out as most enriched.

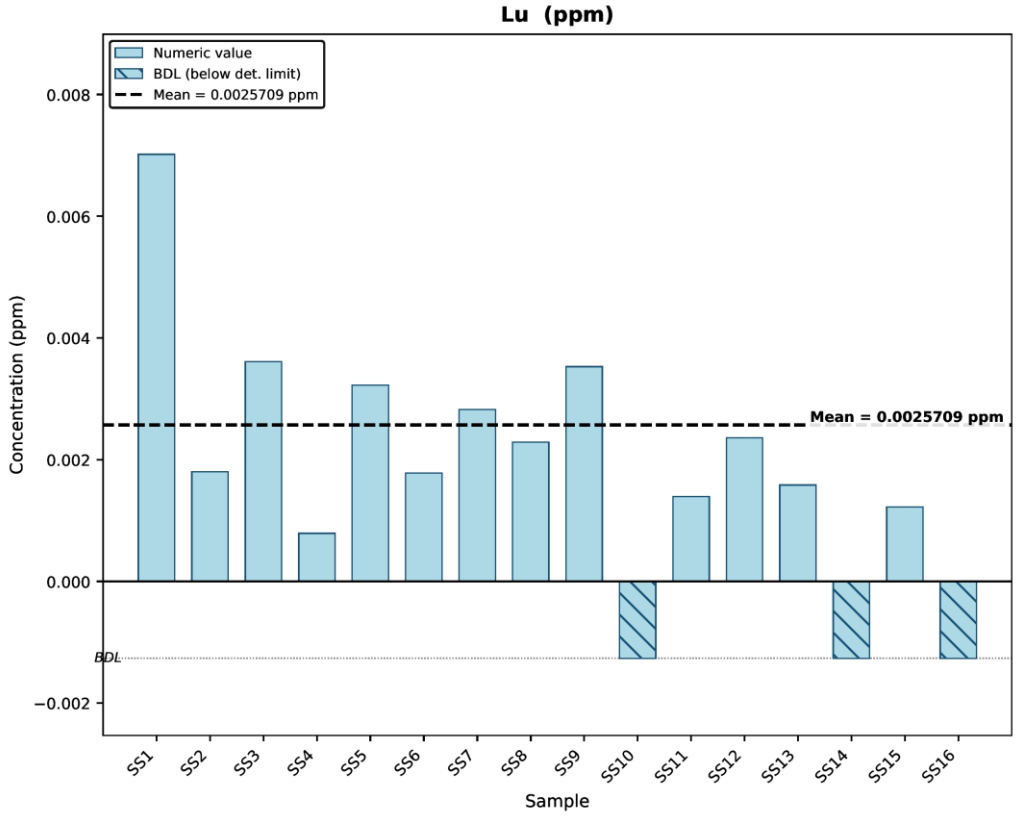


Figure 4.21 Lutetium values observed in samples

4.2.26 Magnesium (Mg)

Magnesium was detected in all 16 samples with a concentration range of 0.0046–1.6211 ppm and a mean of approximately 0.3223 ppm. The highest Mg was recorded in SS1 (1.6211 ppm), followed by SS5 (0.8727 ppm) and SS2 (0.6230 ppm), while the lowest values occurred in SS14 (0.0046 ppm), SS10 (0.0060 ppm), and SS16 (0.0433 ppm). The nearly 355 fold range from SS14 to SS1 is the largest relative inter sample variation of any universally detected element in the dataset and clearly delineates two compositional groups, the Mg-rich samples SS1, SS2, SS5, SS11 and the Mg-poor samples SS14, SS10, SS16, SS6, suggesting significant mineralogical variability across the 16 sampled portions of the intrusive body.

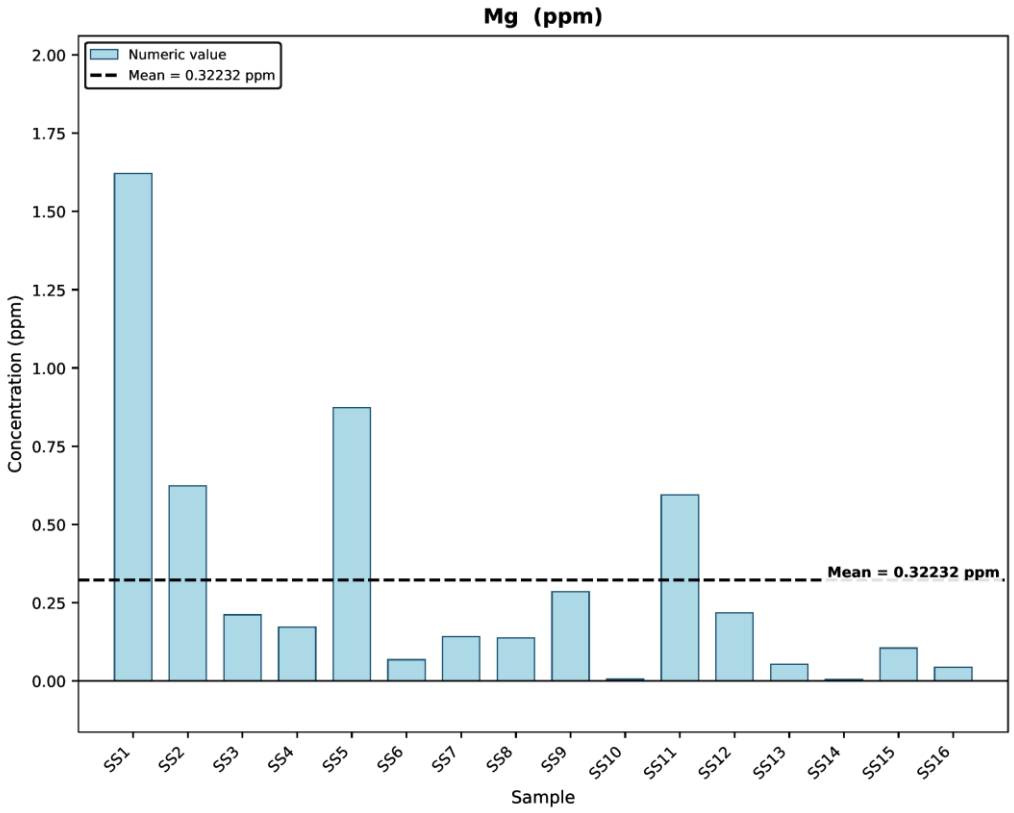


Figure 4.22 Magnesium values observed in samples

4.2.27 Manganese (Mn)

Manganese was detected in all 16 samples with a concentration range of 0.0194–0.3436 ppm and a mean of approximately 0.1115 ppm. The highest Mn was recorded in SS1 (0.3436 ppm), followed by SS12 (0.2510 ppm) and SS5 (0.2255 ppm), while the lowest values occurred in SS16 (0.0194 ppm), SS15 (0.0265 ppm), and SS8 (0.0351 ppm). The wide concentration range is nearly 18 fold from SS16 to SS1 and is among one of the largest inter sample variations for any universally detected element in the dataset. The high Mn in SS1 is consistent with its overall enrichment in multiple elements including Mg (1.621 ppm), V (1.161 ppm), Li (0.0565 ppm), and Rb (0.5004 ppm), further supporting the interpretation of SS1 as the most mafically enriched sample in the suite.

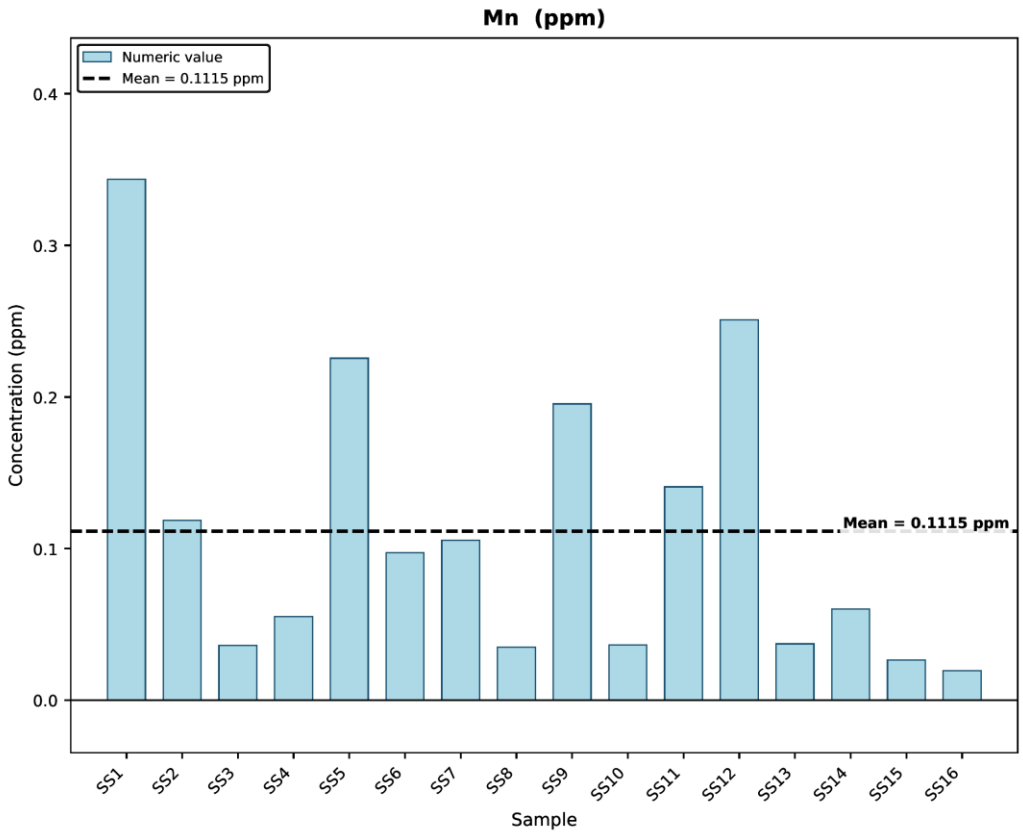


Figure 4.23 Manganese values observed in samples

4.2.28 Neodymium (Nd)

Neodymium was detected in 14 out of 16 samples, remaining BDL in SS4 and SS8, with a concentration range of 0.0088–0.0455 ppm and a mean of approximately 0.0256 ppm. The highest Nd value was recorded in SS2 (0.0455 ppm), followed by SS5 (0.0405 ppm) and SS16 (0.0391 ppm), while the lowest detectable value occurred in SS9 (0.0088 ppm), a broadly distributed LREE with no single dominant control noted.

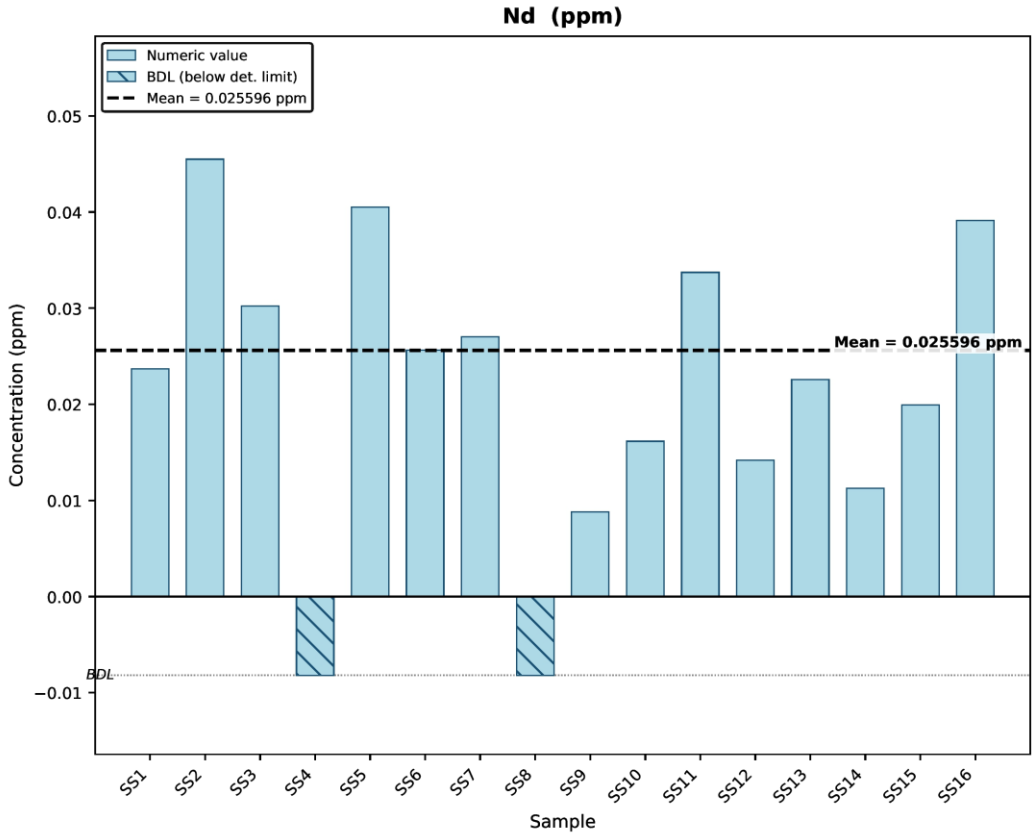


Figure 4.24 Neodymium values observed in samples

4.2.29 Nickel (Ni)

Nickel was detected in 11 out of 16 samples. SS1 (0.0931 ppm), SS2 (0.0475 ppm), SS3 (0.0084 ppm), SS5 (0.0130 ppm), SS6 (0.0052 ppm), SS8 (0.0067 ppm), SS9 (0.0543 ppm), SS11 (0.0146 ppm), SS12 (0.0084 ppm), SS13 (0.0217 ppm), and SS16 (0.0270 ppm), remaining BDL in SS4, SS7, SS10, SS14, and SS15. The highest Ni was recorded in SS1 (0.0931 ppm), consistent with that sample's overall high compatible element signature, while the lowest detectable value appeared in SS6 (0.0052 ppm). The five BDL samples, SS4, SS7, SS10, SS14, SS15, are broadly consistent with being among the more compositionally evolved or modified samples in the suite.

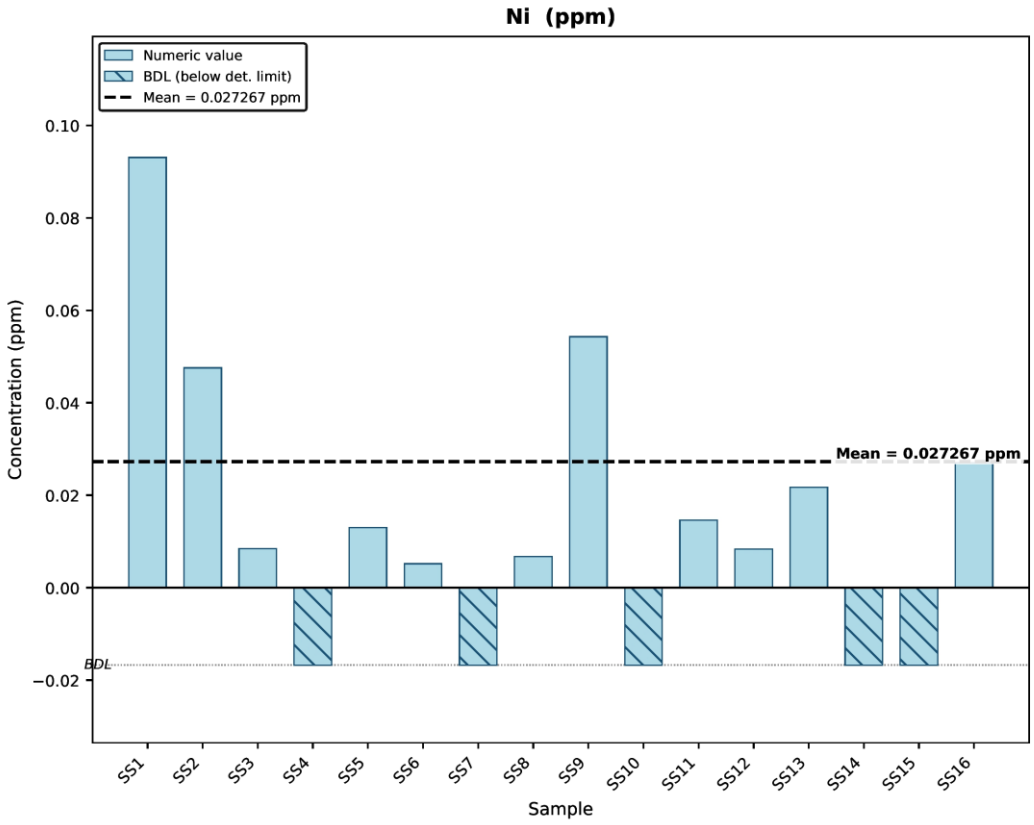


Figure 4.25 Nickel values observed in samples

4.2.30 Niobium (Nb)

Niobium was detected in 12 out of 16 samples. SS1 (0.1064 ppm), SS2 (0.1292 ppm), SS3 (0.0212 ppm), SS5 (0.0864 ppm), SS7 (0.0077 ppm), SS8 (0.0080 ppm), SS9 (0.0100 ppm), SS10 (0.0036 ppm), SS11 (0.0408 ppm), SS12 (0.0068 ppm), SS15 (0.0139 ppm), and SS16 (0.0074 ppm), remaining BDL in SS4, SS6, SS13, and SS14. The highest Nb was recorded in SS2 (0.1292 ppm), followed by SS1 (0.1064 ppm) and SS5 (0.0864 ppm), while the lowest detectable value appeared in SS10 (0.0036 ppm). The high Nb in SS2 and SS1 is consistent with these being among the more geochemically enriched samples, as SS2 also records the highest Ti (0.7035 ppm) and Pd (0.1873 ppm) values, suggesting coenrichment of Nb and Ti in the samples.

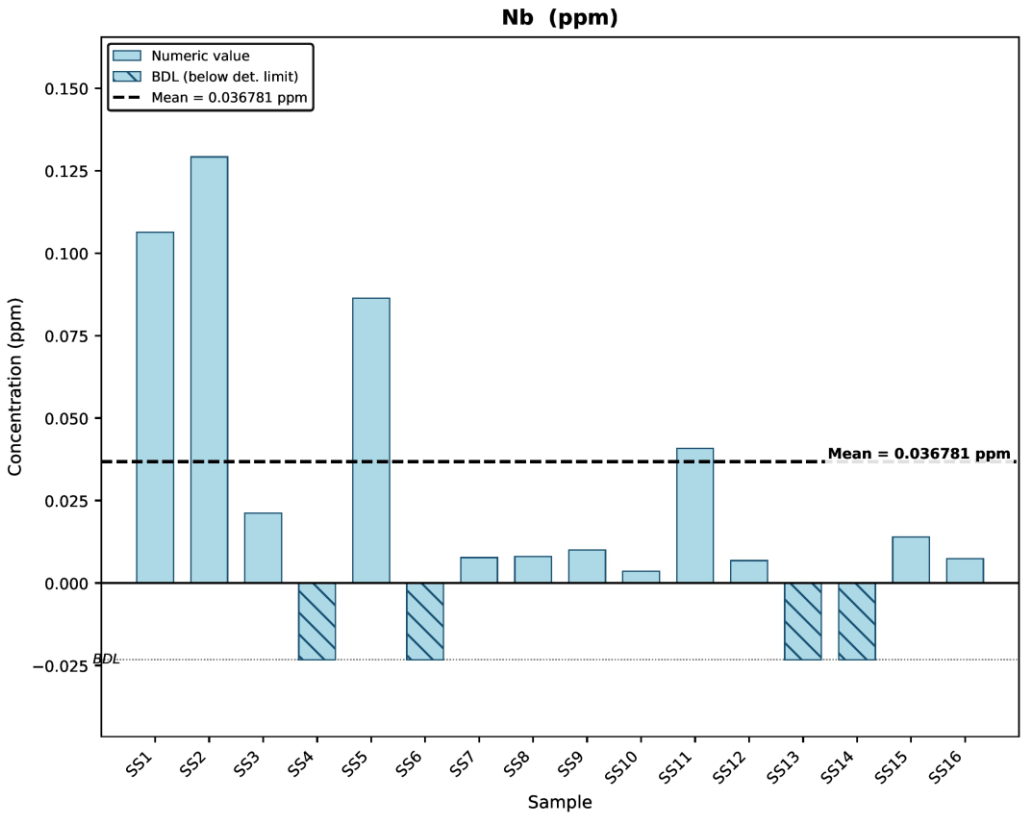


Figure 4.26 Niobium values observed in samples

4.2.31 Palladium (Pd)

Palladium was detected in 15 out of 16 samples, remaining BDL only in SS7, with a concentration range of 0.0185–0.1873 ppm and a mean of approximately 0.0880 ppm. The highest Pd value was recorded in SS2 (0.1873 ppm), followed by SS13 (0.1575 ppm) and SS10 (0.1410 ppm), while the lowest detectable value occurred in SS5 (0.0185 ppm). The near universal detection of Pd with a wide concentration range is one of the most geochemically significant observations in the entire dataset, as it indicates pervasive Pd enrichment throughout most of the Oghi dolerite intrusion. The exceptionally low Pd in SS5 (0.0185 ppm) stands in contrast to its anomalous Cu (0.5458 ppm), As (0.2487 ppm), Fe (8.274 ppm), and Al (3.3752 ppm) values.

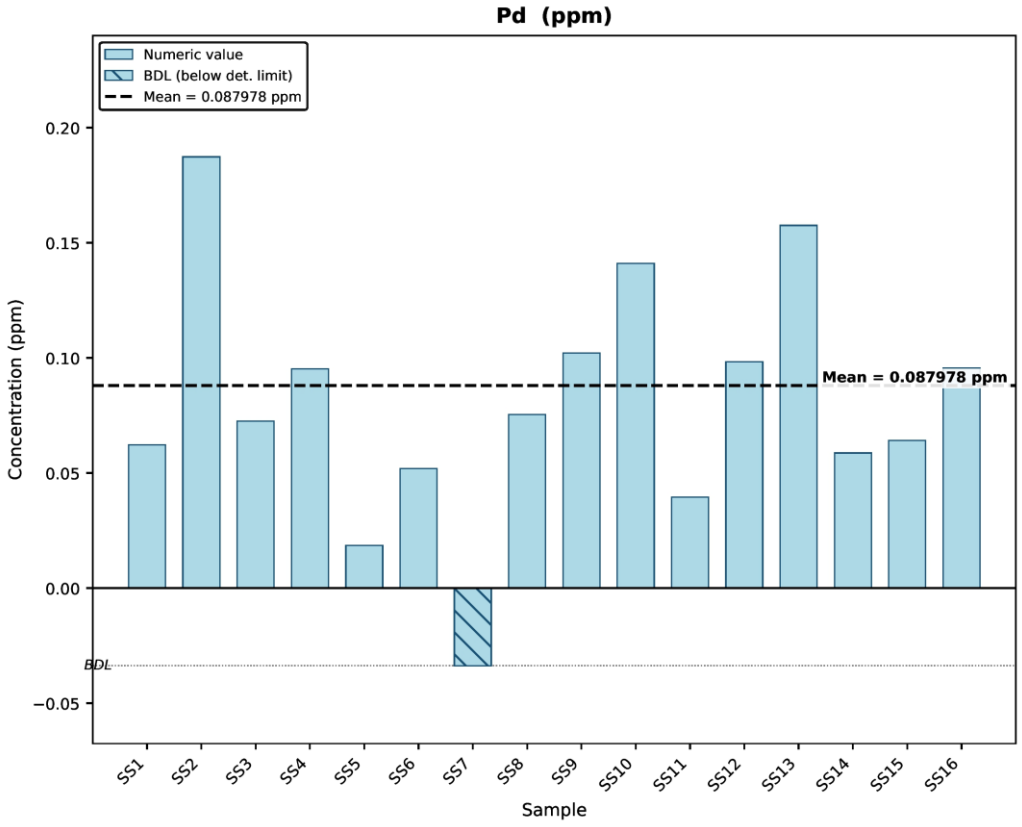


Figure 4.27 Palladium values observed in samples

4.2.32 Phosphorus (P)

Phosphorus was ADL across all 16 samples, SS1 through SS16, without exception. The universal ADL status for P throughout the entire sample suite indicates that P concentrations consistently exceed the ICP-MS calibration range in all 16 dolerites, confirming that it is highly abundant.

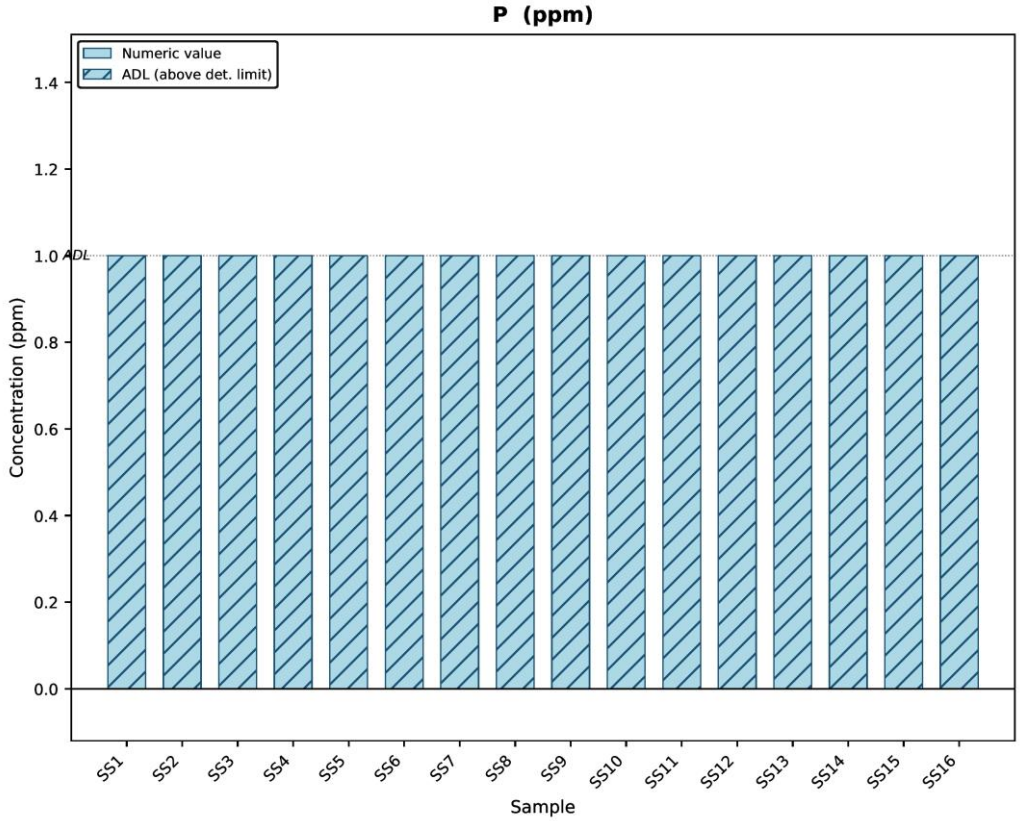


Figure 4.28 Phosphorus values observed in samples

4.2.33 Platinum (Pt)

Platinum was detected in 11 out of 16 samples. SS1 (0.0177 ppm), SS2 (0.0093 ppm), SS4 (0.0165 ppm), SS6 (0.0203 ppm), SS8 (0.0120 ppm), SS9 (0.0134 ppm), SS10 (0.0213 ppm), SS11 (0.0202 ppm), SS12 (0.0162 ppm), SS13 (0.0062 ppm), and SS16 (0.0116 ppm), remaining BDL in SS3, SS5, SS7, SS14, and SS15. The highest Pt was recorded in SS10 (0.0213 ppm) and SS6 (0.0203 ppm), while the lowest detectable value appeared in SS13 (0.0062 ppm), broadly distributed PGE with moderate variability.

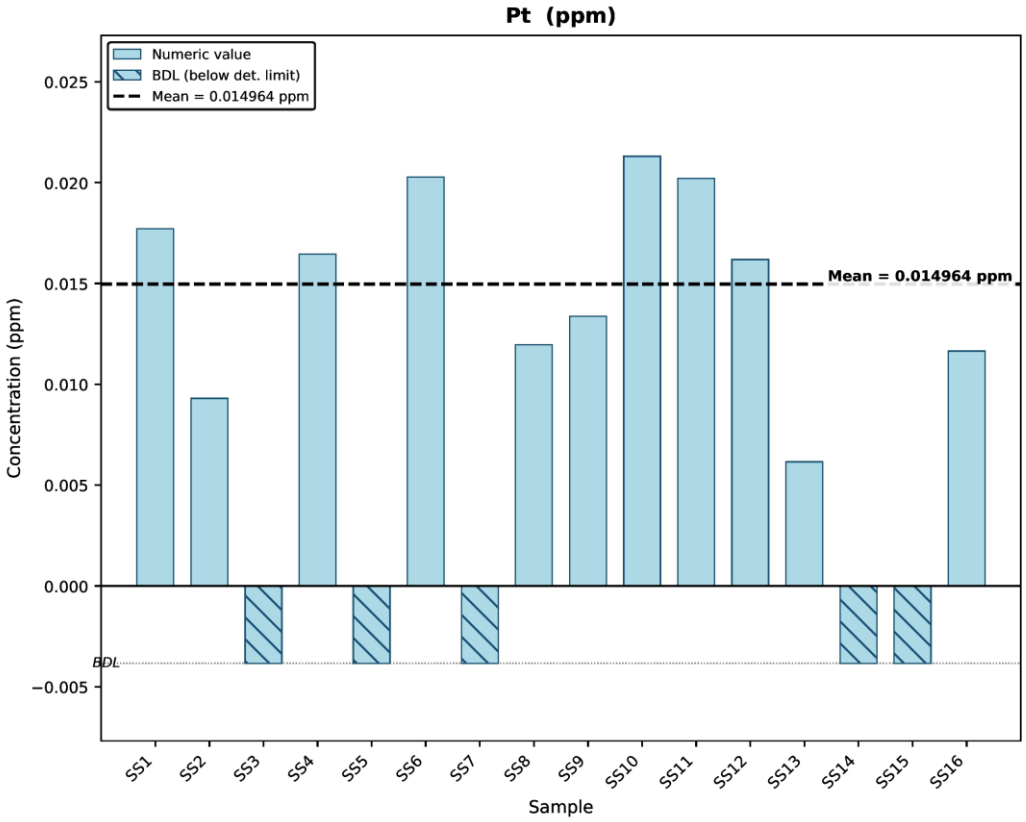


Figure 4.29 Platinum values observed in samples

4.2.34 Potassium (K)

Potassium yielded numeric values in 6 samples and ADL readings in the remaining 10. Among the quantifiable samples, the range was 6.212–10.852 ppm with a mean of approximately 7.692 ppm; SS6 (7.729 ppm), SS7 (10.852 ppm, highest numeric K in the dataset), SS10 (6.549 ppm), SS13 (7.483 ppm), SS14 (6.212 ppm being lowest), and SS16 (7.325 ppm). The ADL status in SS1, SS2, SS3, SS4, SS5, SS8, SS9, SS11, SS12, and SS15 indicates that K concentrations in those 10 samples exceed the instrument's calibration range and are thus even higher than the numeric maximum of 10.852 ppm recorded in SS7.

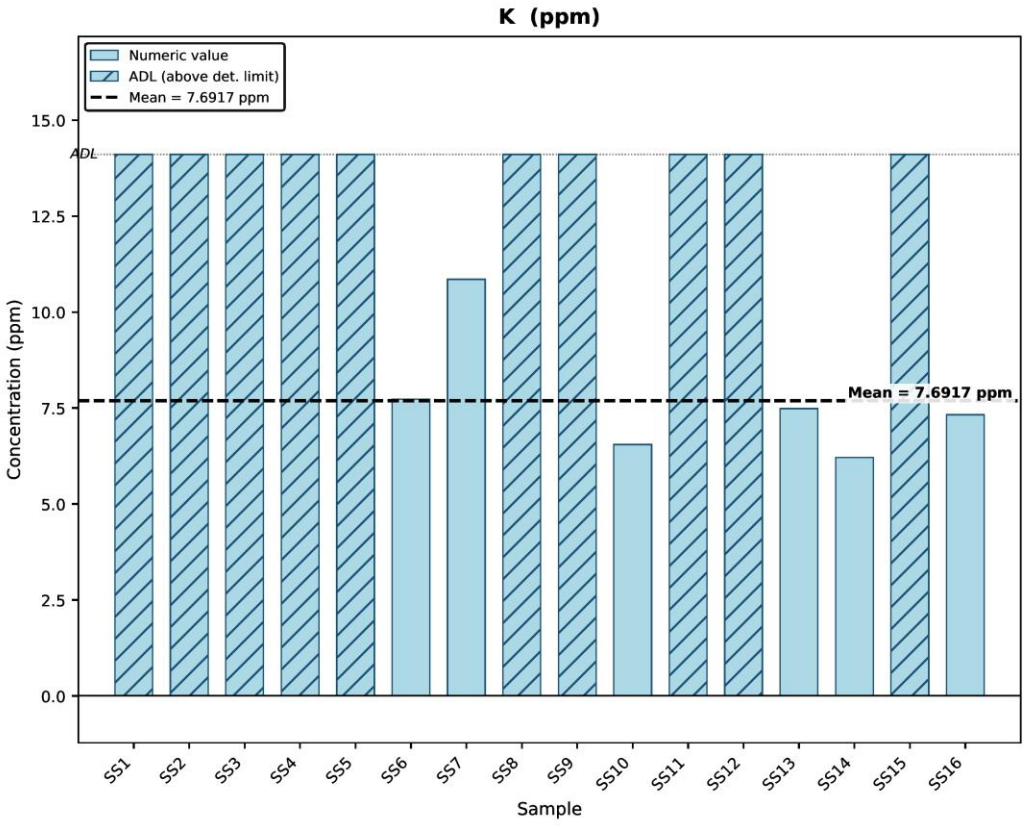


Figure 4.30 Potassium values observed in samples

4.2.35 Praseodymium (Pr)

Praseodymium was detected in only 4 out of 16 samples, SS3 (0.0372 ppm), SS5 (0.1071 ppm), SS8 (0.1100 ppm), and SS11 (0.0383 ppm), remaining BDL in SS1, SS2, SS4, SS6, SS7, SS9, SS10, SS12, SS13, SS14, SS15, and SS16. The highest value was recorded in SS8 (0.1100 ppm), followed closely by SS5 (0.1071 ppm), both of which are substantially higher than the other two detecting samples SS3 and SS11, suggesting localized LREE enrichment.

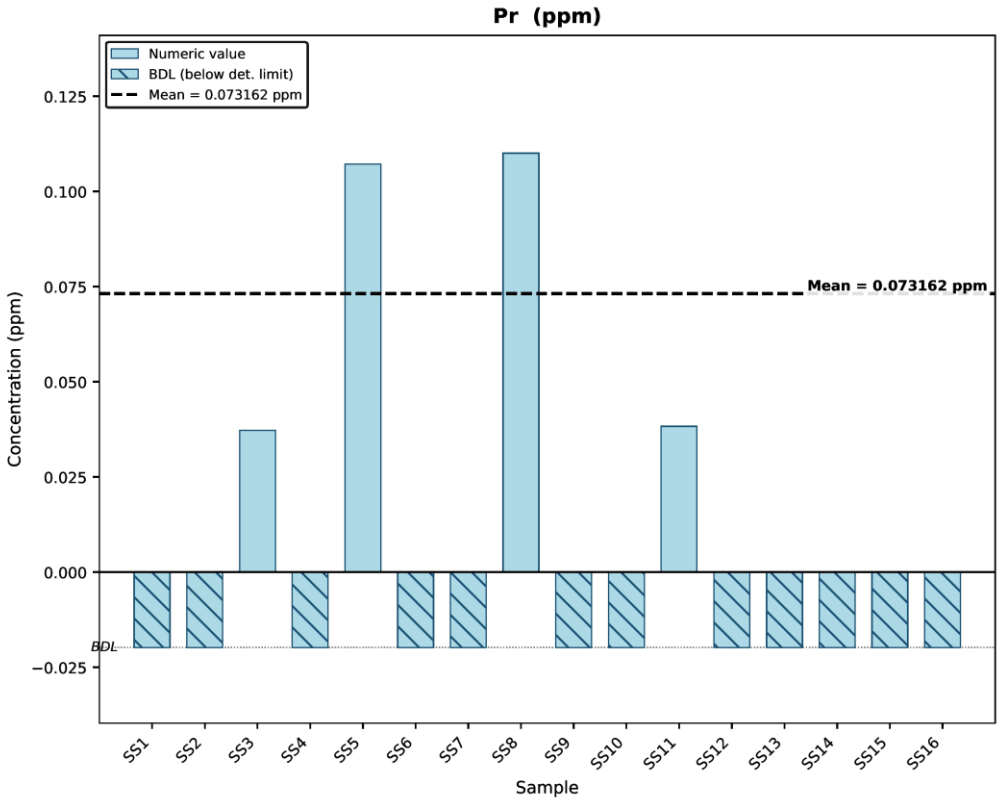


Figure 4.31 Praseodymium values observed in samples

4.2.36 Rhenium (Re)

Rhenium remained BDL across all 16 samples, SS1 through SS16, without exception. The complete absence of detectable Re is consistent with its geochemical behavior as a trace element typically recovered as a byproduct of molybdenum processing, and its universal BDL status across the suite mirrors the identically BDL status of Mo throughout all 16 samples.

4.2.37 Rhodium (Rh)

Rhodium remained BDL across all 16 samples, SS1 through SS16, without exception. The universal absence of detectable Rh in the entire sample suite is consistent with Rh being the rarest PGE in continental Mafic Rocks.

4.2.38 Rubidium (Rb)

Rubidium was detected in all 16 samples with a concentration range of 0.0721–0.5004 ppm and a mean of approximately 0.2511 ppm. The highest Rb was recorded in SS1 (0.5004 ppm), followed by SS2 (0.4457 ppm) and SS3 (0.4328 ppm), while the lowest values occurred in SS10 (0.0721 ppm), SS4 (0.0767 ppm), and SS13 (0.0758 ppm). The universal detection of Rb and its relatively elevated concentrations in SS1, SS2, and SS3, which cluster together as the highest-Rb samples, contrasts sharply with the much lower Rb values in SS4, SS10, and SS13, indicating a two-tier alkali distribution.

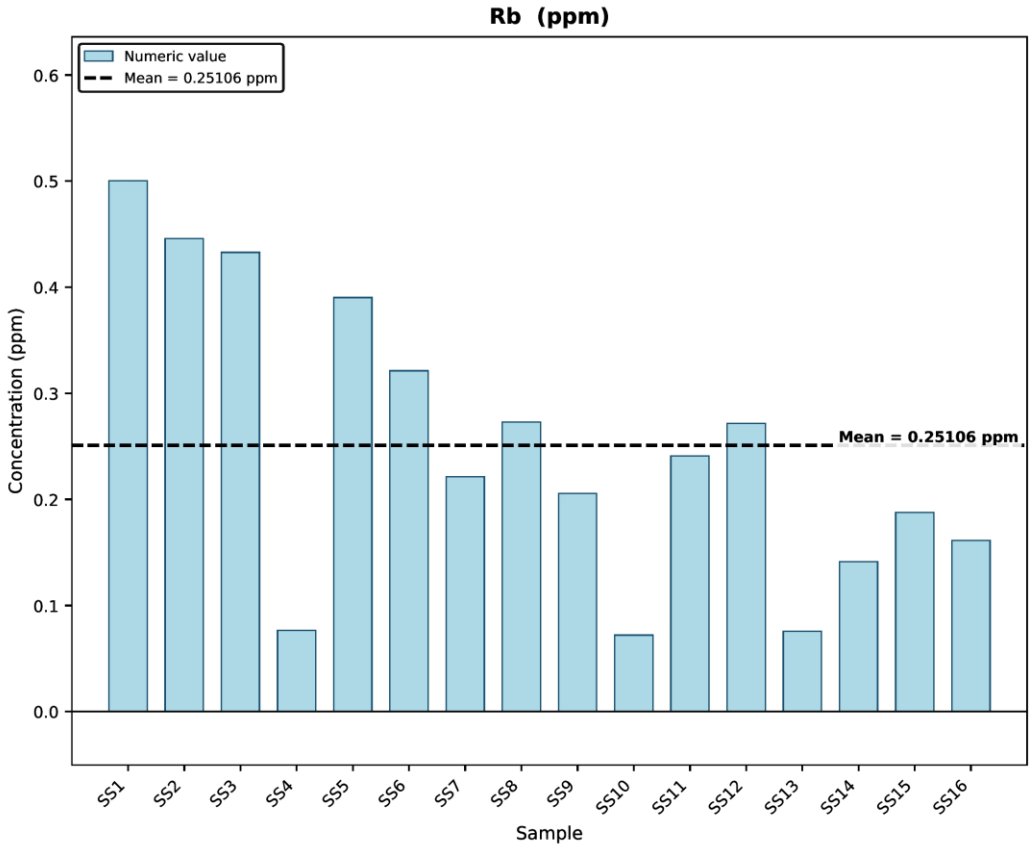


Figure 4.32 Rubidium values observed in samples

4.2.39 Ruthenium (Ru)

Ruthenium was detected in 6 out of 16 samples, SS1 (0.0582 ppm), SS2 (0.0181 ppm), SS5 (0.0475 ppm), SS6 (0.0101 ppm), SS9 (0.0419 ppm), and SS12 (0.0104 ppm), remaining BDL in SS3, SS4, SS7, SS8, SS10, SS11, SS13, SS14, SS15, and SS16. The highest Ru was recorded in SS1 (0.0582 ppm), followed by SS5 (0.0475 ppm) and SS9 (0.0419 ppm), while the lowest detectable value appeared in SS6 (0.0101 ppm), a moderately restricted PGE with SS1 highest.

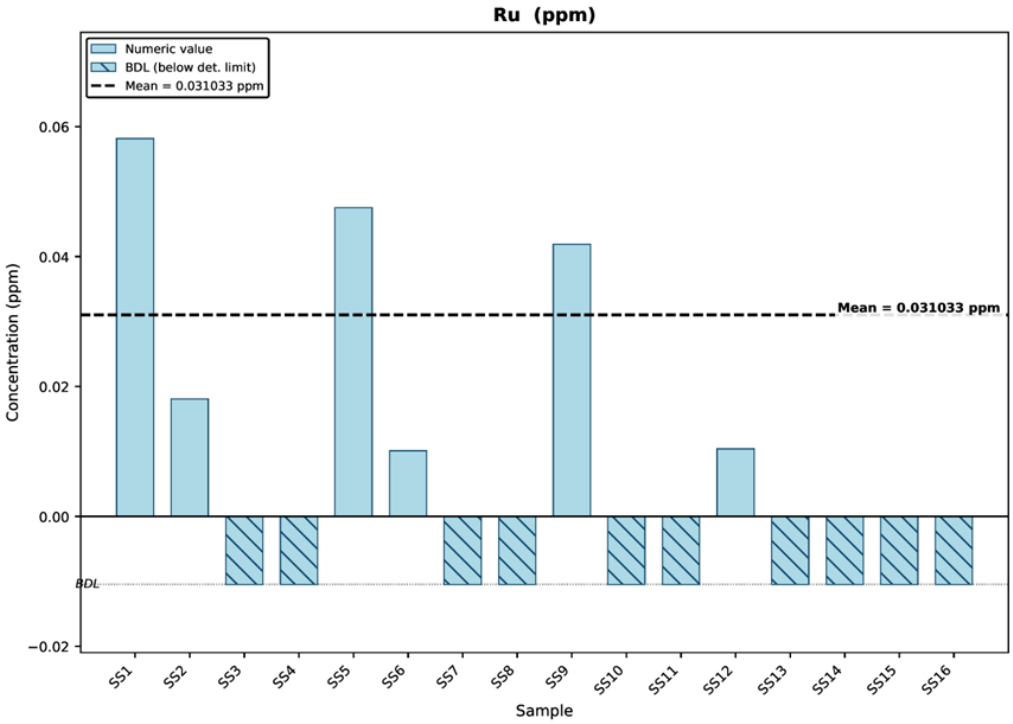


Figure 4.33 Ruthenium values observed in samples

4.2.40 Samarium (Sm)

Samarium was detected in 8 out of 16 samples, SS3 (0.0129 ppm), SS5 (0.0080 ppm), SS6 (0.0047 ppm), SS8 (0.0093 ppm), SS12 (0.0057 ppm), SS13 (0.0072 ppm), SS14 (0.0020 ppm), and SS15 (0.0157 ppm), remaining BDL in SS1, SS2, SS4, SS7, SS9, SS10, SS11, and SS16. The highest Sm value was recorded in SS15 (0.0157 ppm), while the lowest detectable value appeared in SS14 (0.0020 ppm). The detection of Sm in exactly half the samples, and the occurrence of BDL in SS1 and SS11, both of which are relatively enriched in other elements.

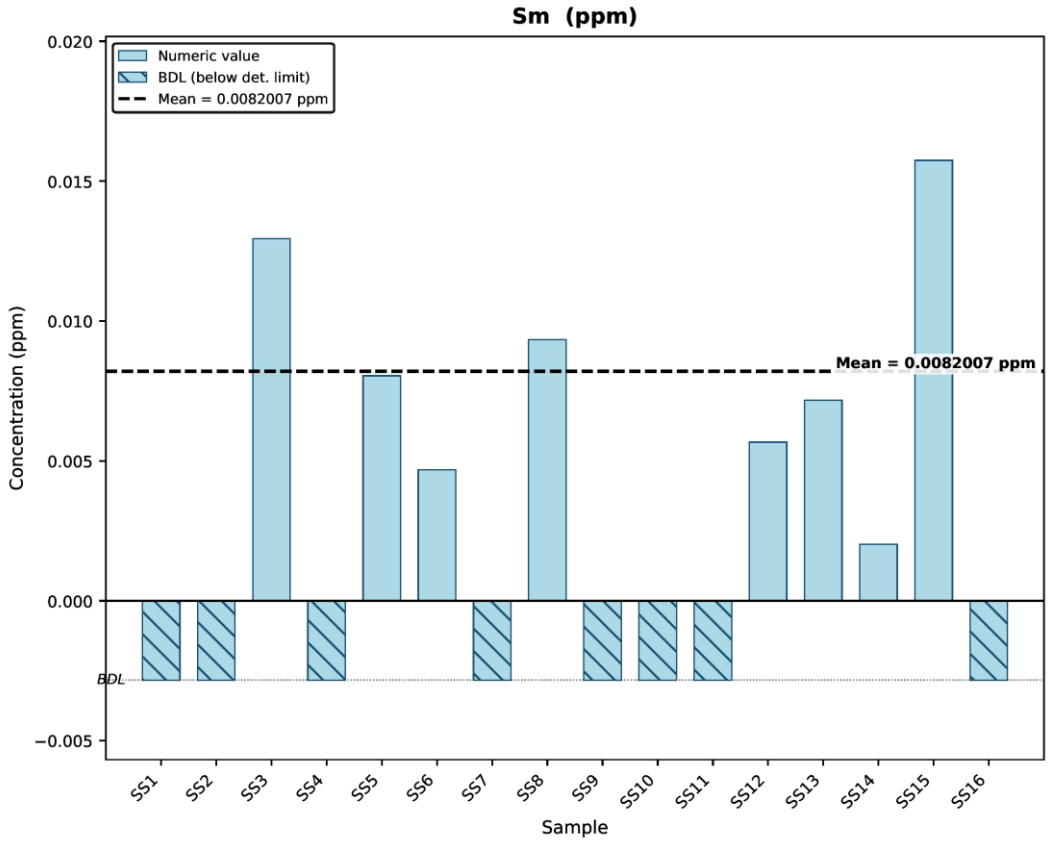


Figure 4.34 Samarium values observed in samples

4.2.41 Scandium (Sc)

Scandium was detected in 15 out of 16 samples, remaining BDL only in SS9, with a concentration range of 0.0007–0.0026 ppm and a mean of approximately 0.0017 ppm. The highest Sc values were recorded in SS7 (0.0026 ppm) and SS4 (0.0021 ppm), while the lowest detectable values appeared in SS2 (0.0007 ppm) and SS8 (0.0008 ppm). The near universal detection of Sc across SS1 through SS16, with only SS9 showing BDL, confirms a consistent trace level background of Sc throughout the dolerite body. The low concentrations throughout are consistent with Sc's compatible behavior in mafic systems, where it is distributed at trace levels across the full range of compositional variations represented by the 16 samples.

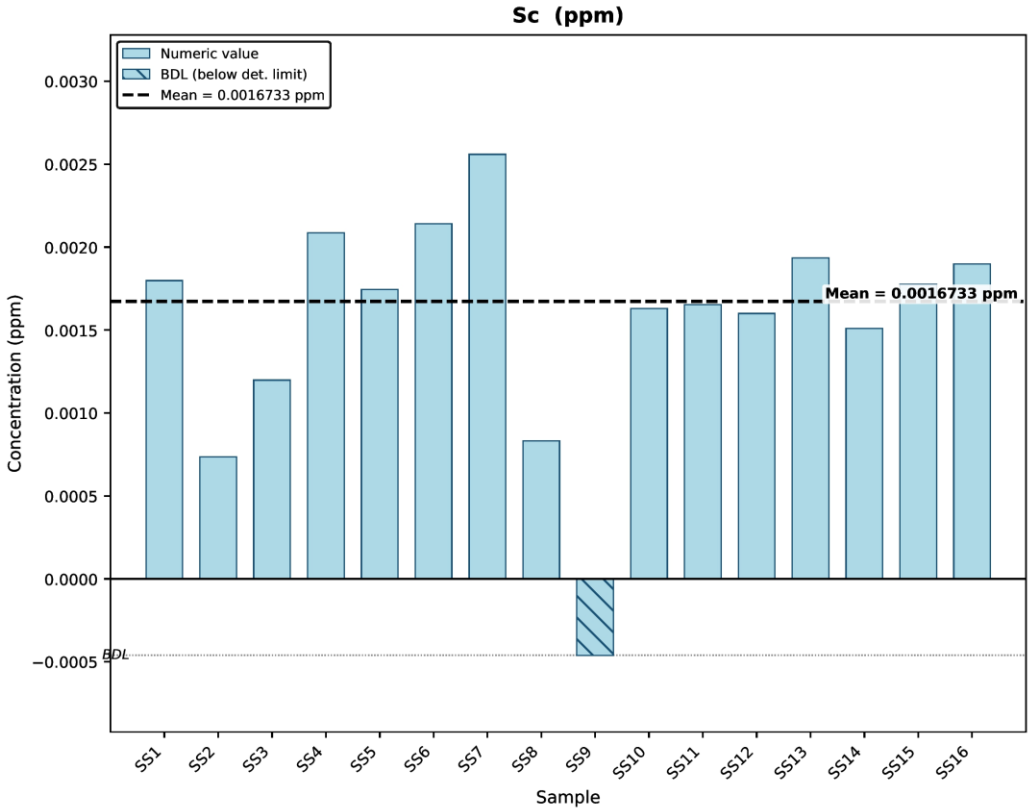


Figure 4.35 Scandium values observed in samples

4.2.42 Silicon (Si)

Silicon remained BDL across all 16 samples, SS1 through SS16, without exception.

4.2.43 Silver (Ag)

Silver was detected in 15 out of 16 samples, remaining BDL only in SS5, with a concentration range of 0.0005–0.0157 ppm and a mean of approximately 0.0080 ppm. The highest Ag was recorded in SS2 (0.0157 ppm), followed by SS4 (0.0102

ppm) and SS6 (0.0128 ppm), while the lowest detectable value appeared in SS1 (0.0005 ppm), broadly but variably distributed.

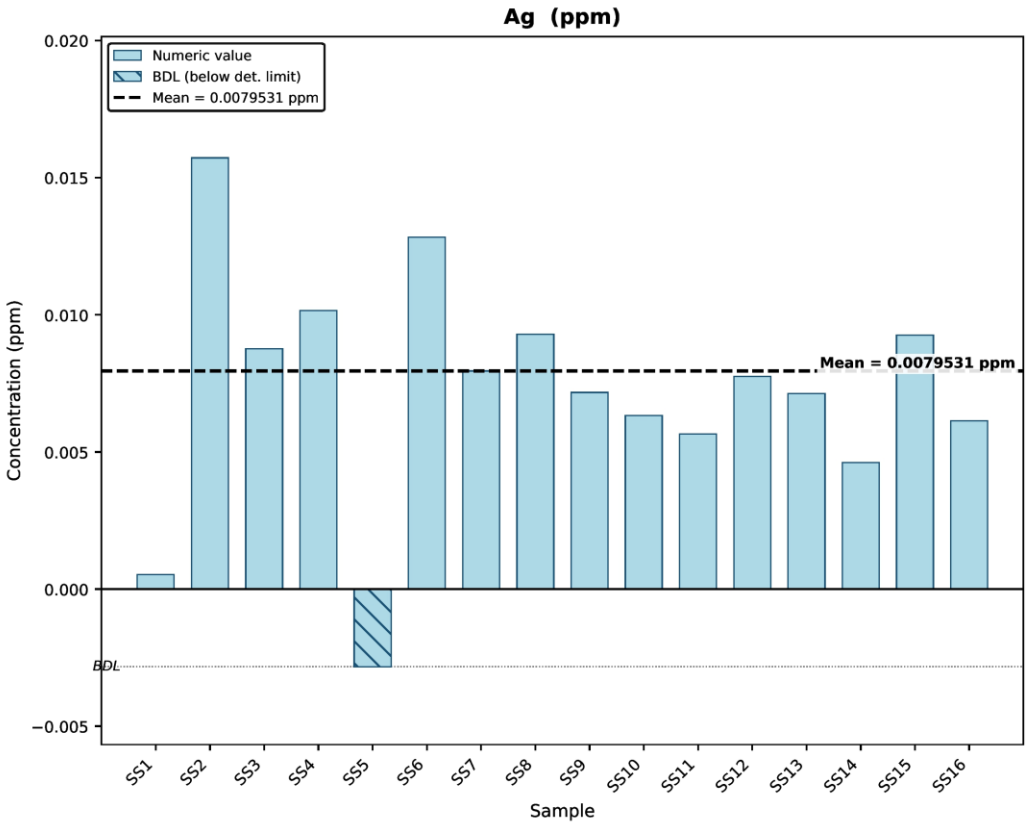


Figure 4.36 Silver values observed in samples

4.2.44 Tantalum (Ta)

Tantalum was detected in 7 out of 16 samples, SS3 (0.0089 ppm), SS5 (0.0158 ppm), SS6 (0.0045 ppm), SS8 (0.0095 ppm), SS9 (0.0132 ppm), SS14 (0.0132 ppm), and SS15 (0.0206 ppm), remaining BDL in SS1, SS2, SS4, SS7, SS10, SS11, SS12, SS13, and SS16. The highest Ta was recorded in SS15 (0.0206 ppm), followed by SS5 (0.0158 ppm) and SS9 (0.0132 ppm), while the lowest detectable value appeared in SS6 (0.0045 ppm), sporadically distributed high field strength element.

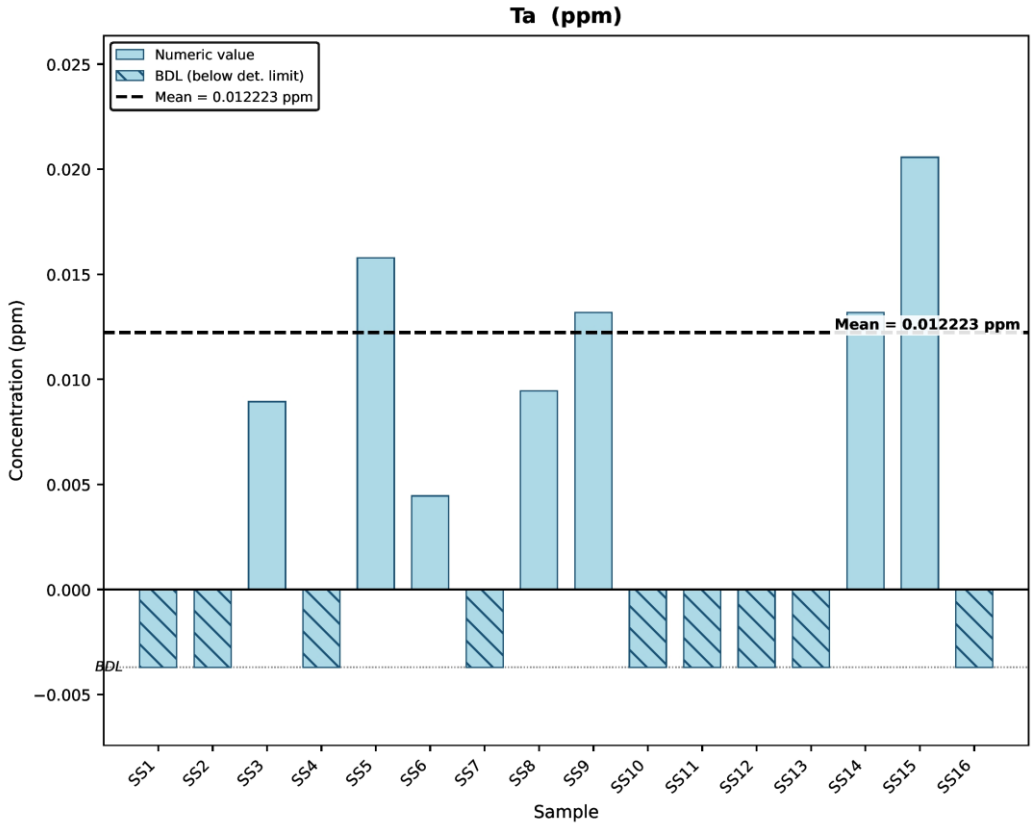


Figure 4.37 Tantalum values observed in samples

4.2.45 Tellurium (Te)

Tellurium was detected in 8 out of 16 samples, SS1 (0.0135 ppm), SS2 (0.0244 ppm), SS5 (0.0109 ppm), SS6 (0.0081 ppm), SS7 (0.0399 ppm), SS9 (0.0121 ppm), SS13 (0.0174 ppm), and SS16 (0.0288 ppm), remaining BDL in SS3, SS4, SS8, SS10, SS11, SS12, SS14, and SS15. The highest Te was recorded in SS7 (0.0399 ppm), followed by SS16 (0.0288 ppm) and SS2 (0.0244 ppm), while the lowest detectable value appeared in SS6 (0.0081 ppm). The distribution of Te across 8 non-consecutive samples reflects the heterogenetic nature of distribution within the intrusive body.

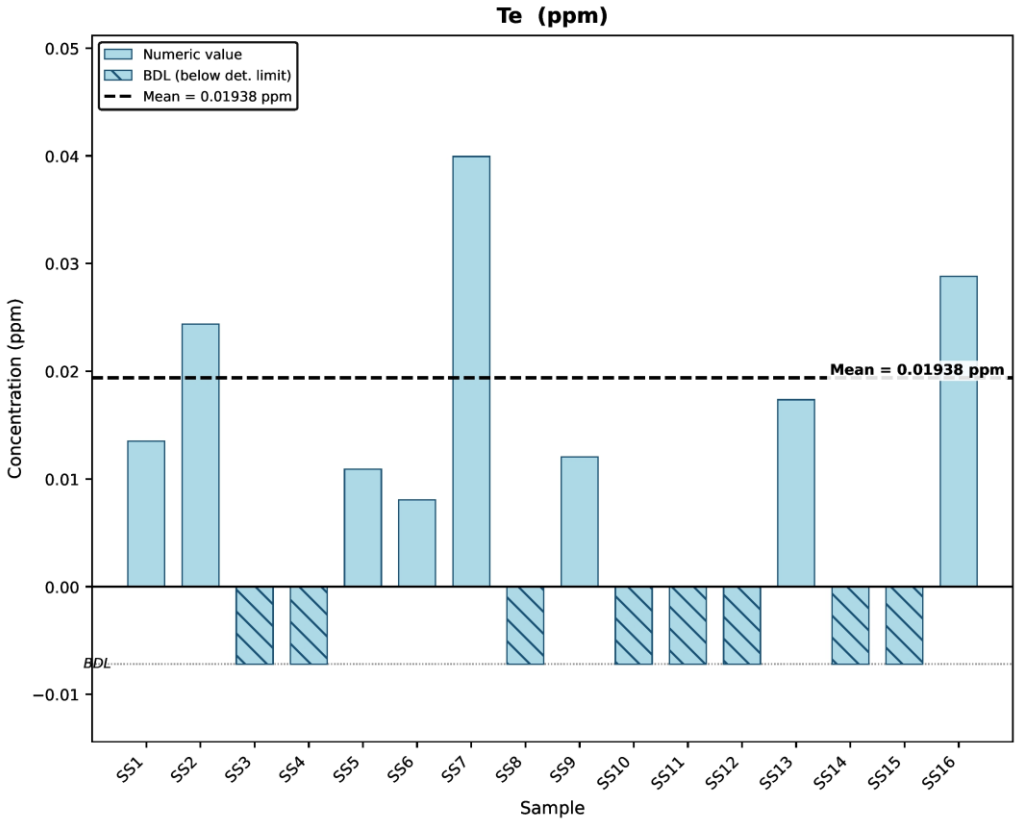


Figure 4.38 Tellurium values observed in samples

4.2.46 Terbium (Tb)

Terbium was detected in 10 out of 16 samples, SS1 (0.0040 ppm), SS4 (0.0047 ppm), SS5 (0.0070 ppm), SS10 (0.0089 ppm), SS11 (0.0057 ppm), SS12 (0.0079 ppm), SS13 (0.0058 ppm), SS14 (0.0084 ppm), SS15 (0.0036 ppm), and SS16 (0.0068 ppm), remaining BDL in SS2, SS3, SS6, SS7, SS8, and SS9. The highest Tb value was recorded in SS10 (0.0089 ppm), followed by SS14 (0.0084 ppm), while the lowest detectable value appeared in SS15 (0.0036 ppm), moderately widespread HREE.

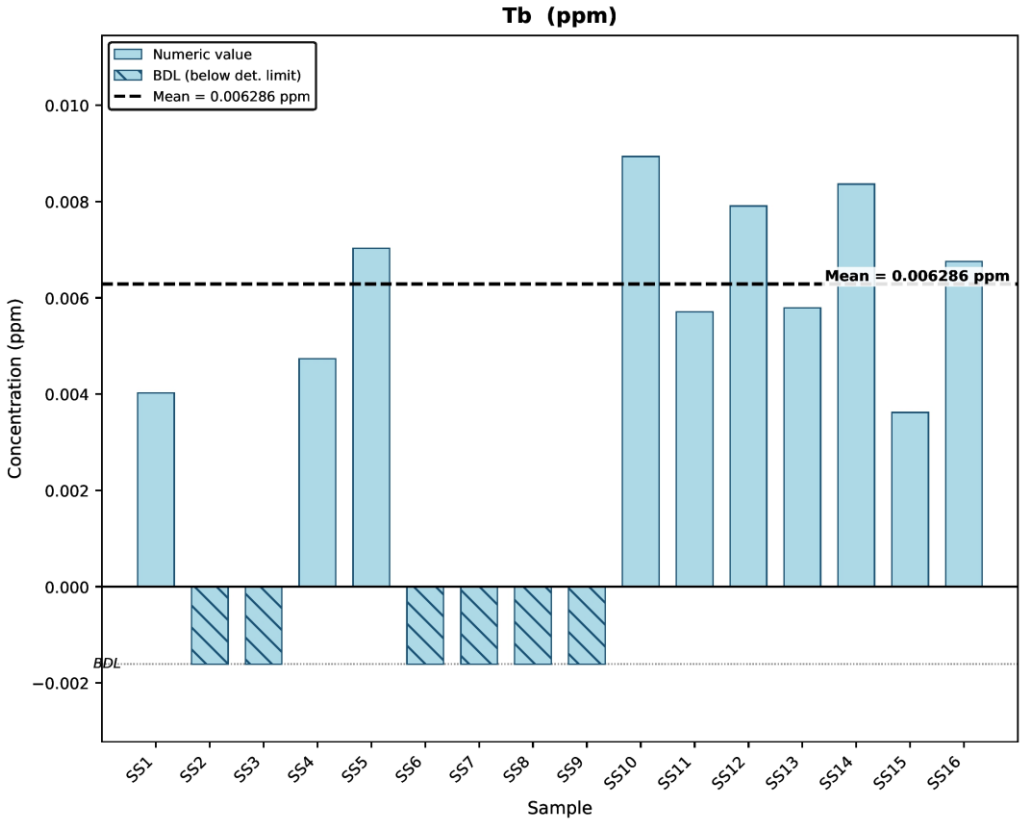


Figure 4.39 Terbium values observed in samples

4.2.47 Thulium (Tm)

Thulium was detected in 15 out of 16 samples, remaining BDL only in SS8, with a concentration range of 0.0011–0.0066 ppm and a mean of approximately 0.0039 ppm. The highest Tm value was recorded in SS5 (0.0066 ppm), followed by SS6 (0.0059 ppm) and SS16 (0.0059 ppm), while the lowest detectable value appeared in SS9 (0.0011 ppm), consistent low-level HREE presence.

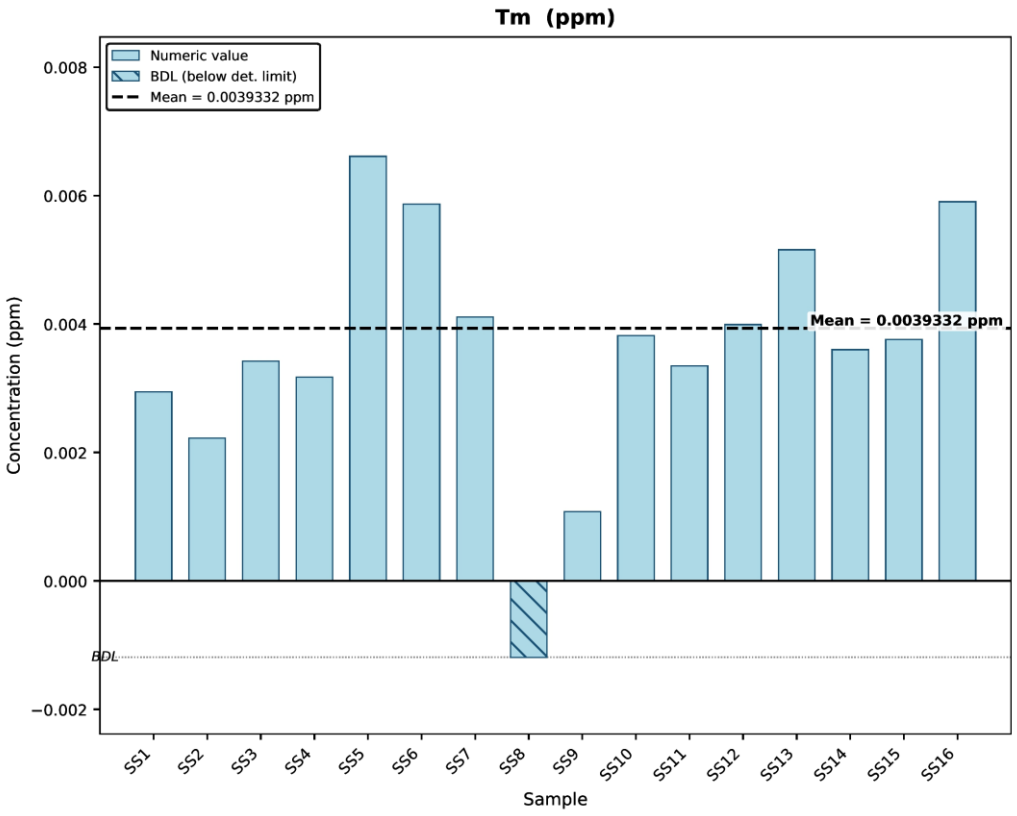


Figure 4.40 Thulium values observed in samples

4.2.48 Tin (Sn)

Tin remained BDL across all 16 samples, SS1 through SS16, without exception.

4.2.49 Tungsten (W)

Tungsten remained BDL across all 16 samples, SS1 through SS16, without exception.

4.2.50 Titanium (Ti)

Titanium was detected in all 16 samples with a concentration range of 0.0391–0.7035 ppm and a mean of approximately 0.1929 ppm. The highest Ti was recorded in SS2 (0.7035 ppm), followed by SS1 (0.6221 ppm) and SS5 (0.4773 ppm), while the lowest values occurred in SS14 (0.0391 ppm), SS10 (0.0398 ppm), and SS13 (0.0422 ppm). The high Ti in SS2 and SS1 is consistent with those being among the most Fe-Ti oxide enriched samples, with SS2 also recording the highest Nb and second highest Pd, further reinforcing the interpretation of a significant oxide component in SS2. The contrast between the Ti-rich upper group (SS1, SS2, SS5, SS11) and the Ti-poor lower group (SS14, SS10, SS13, SS4) reflects major differences in Fe-Ti oxide content across the dolerite body.

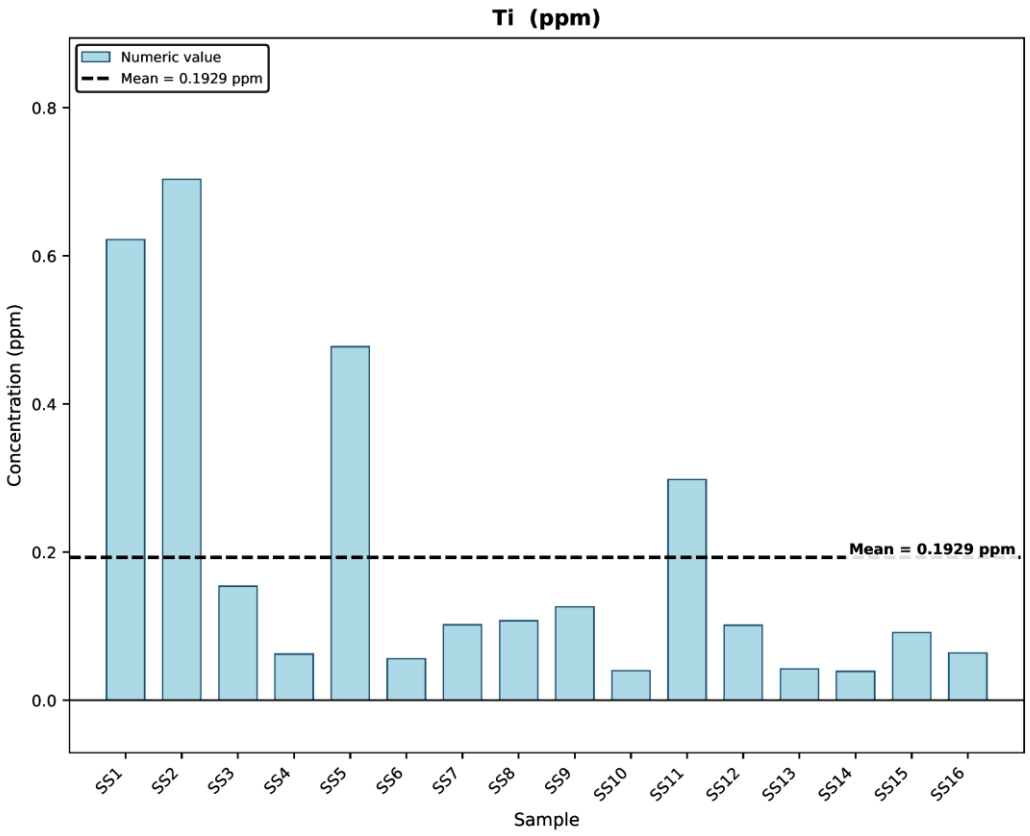


Figure 4.41 Titanium values observed in samples

4.2.51 Uranium (U)

Uranium was detected in 14 out of 16 samples, remaining BDL in SS10 and SS16, with a concentration range of 0.0277–0.4130 ppm and a mean of approximately 0.1284 ppm. The highest U was recorded in SS1 (0.4130 ppm), more than twice the second highest value in SS9 (0.2080 ppm), while the lowest detectable value appeared in SS4 (0.0277 ppm). The nearly 15 fold range in U concentrations from SS4 to SS1, combined with BDL in SS10 and SS16 and elevated values in SS1 and SS9, indicates highly heterogeneous U distribution across the sample suite.

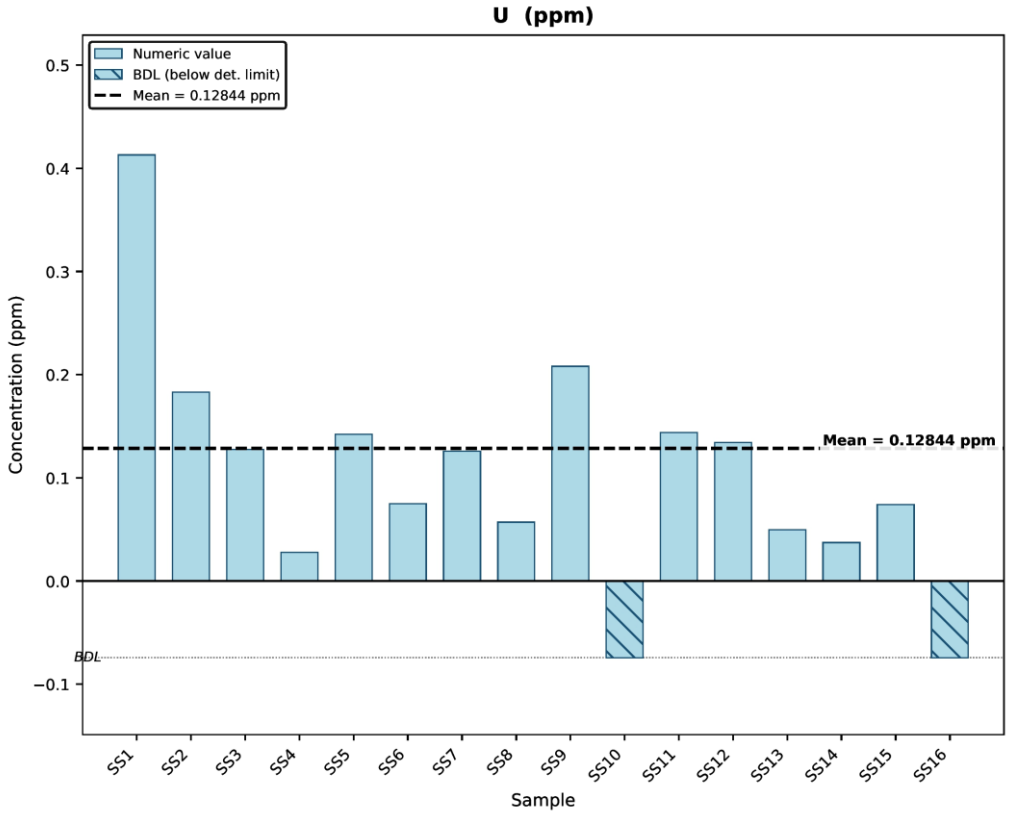


Figure 4.42 Uranium values observed in samples

4.2.52 Vanadium (V)

Vanadium was detected in all 16 samples with a concentration range of 0.0664–1.1613 ppm and a mean of approximately 0.2942 ppm. The highest V was recorded in SS1 (1.1613 ppm), followed by SS5 (0.6650 ppm) and SS3 (0.4710 ppm), while the lowest values occurred in SS14 (0.0664 ppm), SS16 (0.0878 ppm), and SS10 (0.0955 ppm). The nearly 18 fold variation in V concentration from SS14 to SS1 is one of the most pronounced inter sample contrasts in the dataset.

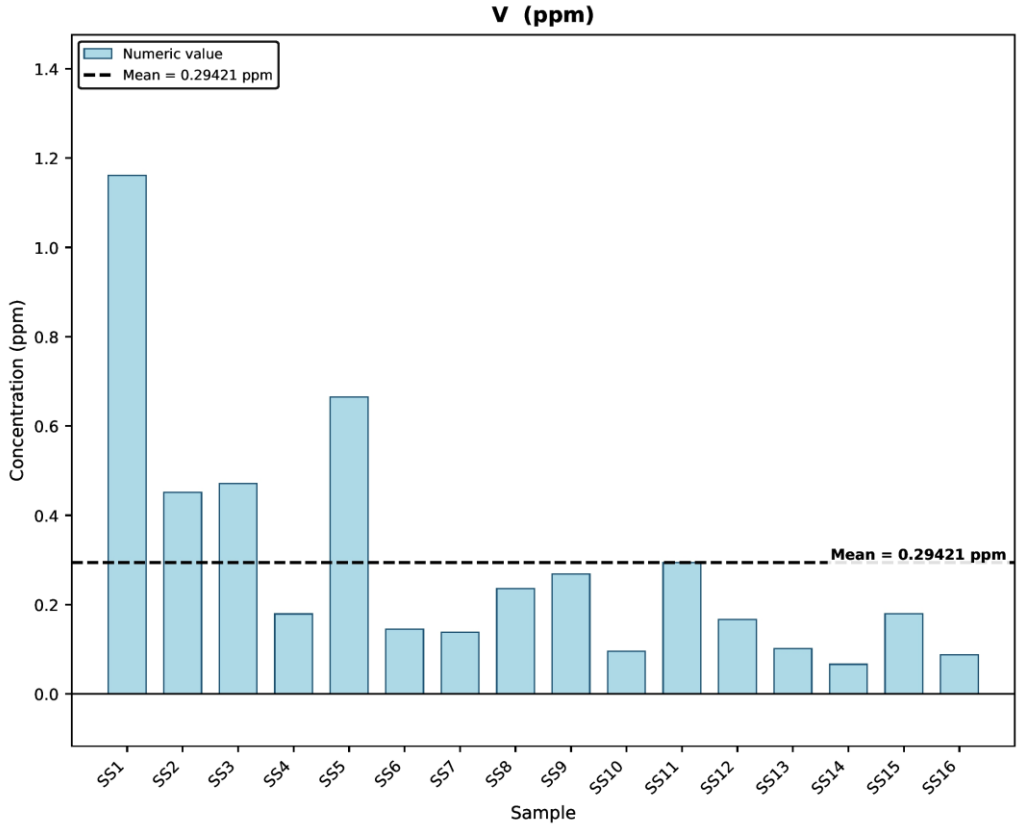


Figure 4.43 Vanadium values observed in samples

4.2.53 Ytterbium (Yb)

Ytterbium was detected in 15 out of 16 samples, remaining BDL only in SS14, with a concentration range of 0.0004–0.0021 ppm and a mean of approximately 0.0013 ppm. The highest Yb value was recorded in SS13 (0.0021 ppm), followed by SS1 (0.0016 ppm) and SS3 (0.0019 ppm), while the lowest detectable value appeared in SS10 (0.0004 ppm) and SS5 (0.0005 ppm), indicating low-level HREE with modest variability.

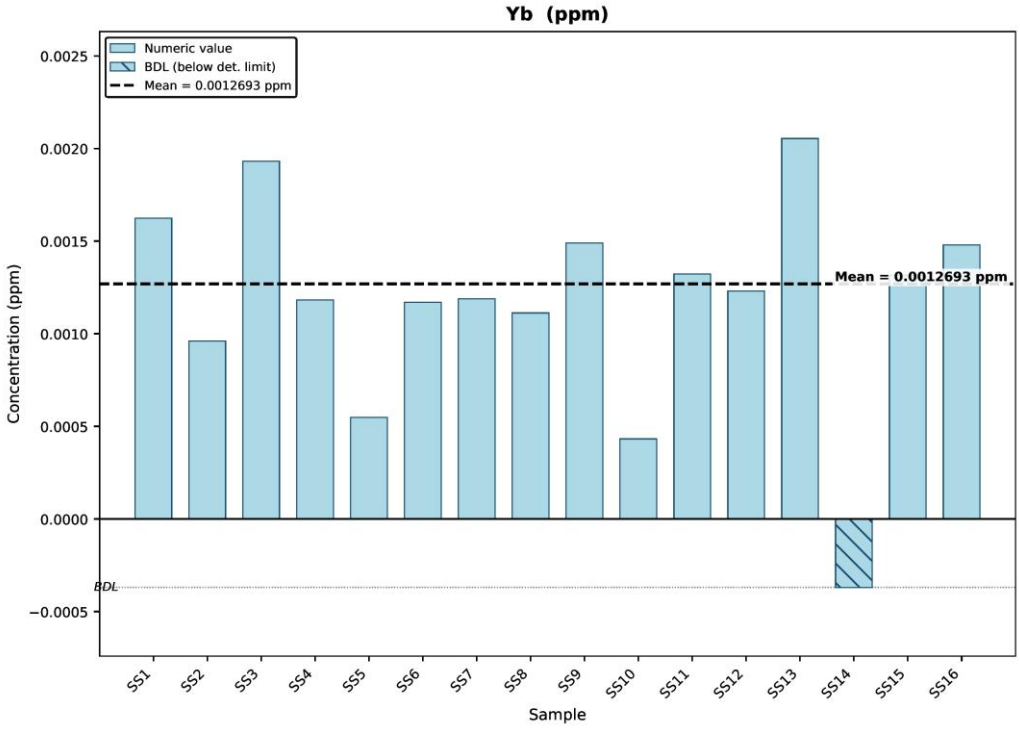


Figure 4.44 Ytterbium values observed in samples

4.2.54 Yttrium (Y)

Yttrium was detected in all 16 samples with a concentration range of 0.0005–0.0070 ppm and a mean of approximately 0.0023 ppm. The highest Y value was recorded in SS1 (0.0070 ppm), followed by SS9 (0.0041 ppm) and SS5 (0.0035 ppm),

while the lowest value occurred in SS14 (0.0005 ppm) followed by SS15 (0.0006 ppm), generally tracking the same enrichment pattern as other compatible/mafic-associated elements (highest in SS1).

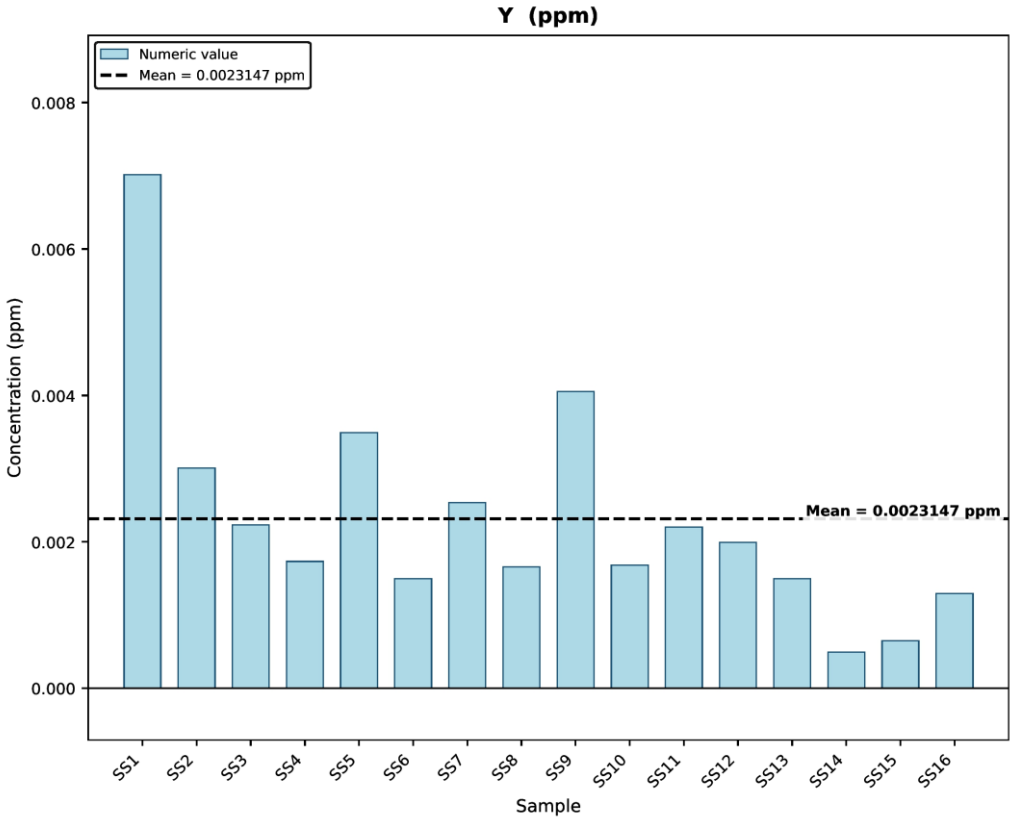


Figure 4.45 Yttrium values observed in samples

4.2.55 Zinc (Zn)

Zinc was detected in all 16 samples with a concentration range of 0.0083–0.1146 ppm and a mean of approximately 0.0381 ppm. The highest Zn was recorded in SS1 (0.1146 ppm), followed by SS2 (0.0893 ppm) and SS5 (0.0606 ppm), while the lowest values occurred in SS10 (0.0083 ppm), SS14 (0.0086 ppm), and SS8 (0.0177 ppm). The consistent detection of Zn across all 16 samples follows a similar pattern to Cu, V, Mn, and Mg, with SS1 being the richest and SS10/SS14 being the

poorest, confirming that Zn distribution broadly tracks the overall mafic enrichment trend across the suite rather than being controlled by discrete zones.

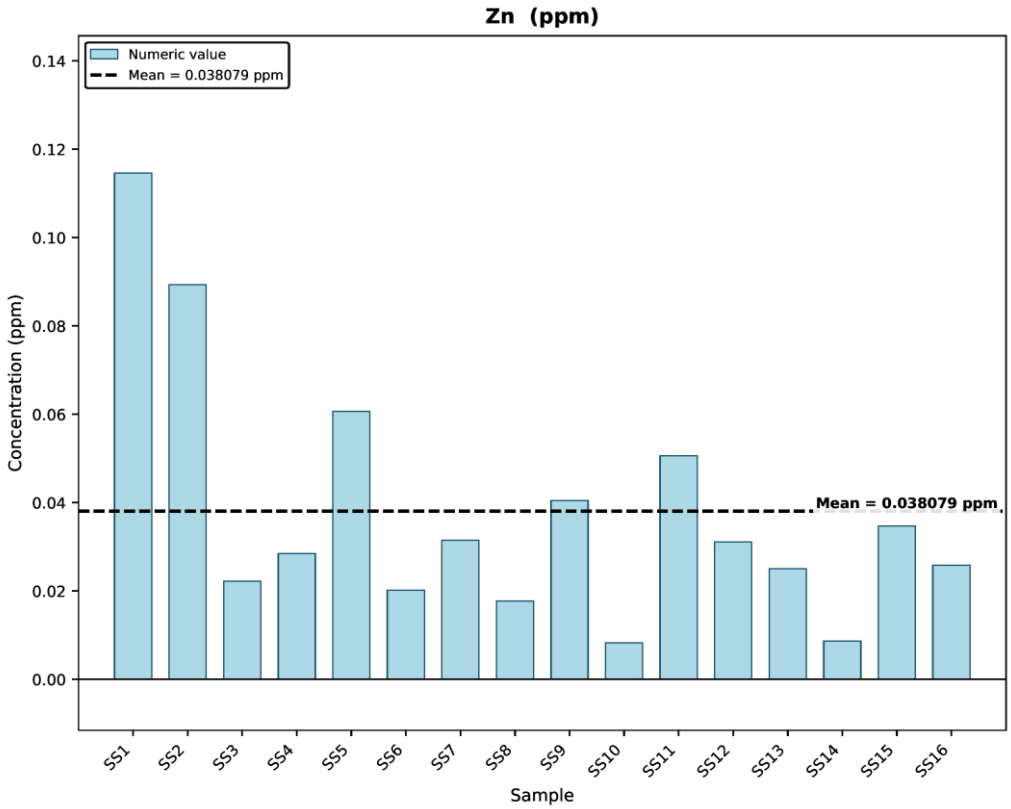


Figure 4.46 Zinc values observed in samples

4.2.56 Zirconium (Zr)

Zirconium was detected in only 3 out of 16 samples, SS1 (0.0032 ppm), SS2 (0.0013 ppm), and SS8 (0.0018 ppm), remaining BDL in the remaining 13 samples including SS3 through SS7, SS9 through SS16. The highest Zr was recorded in SS1 (0.0032 ppm), while the lowest detectable value appeared in SS2 (0.0013 ppm). The near-universal BDL status of Zr across 13 of the 16 samples, combined with its detection only in SS1, SS2, and SS8, confirms that the Zr bearing phase is either absent or extremely rare in most of these dolerites.

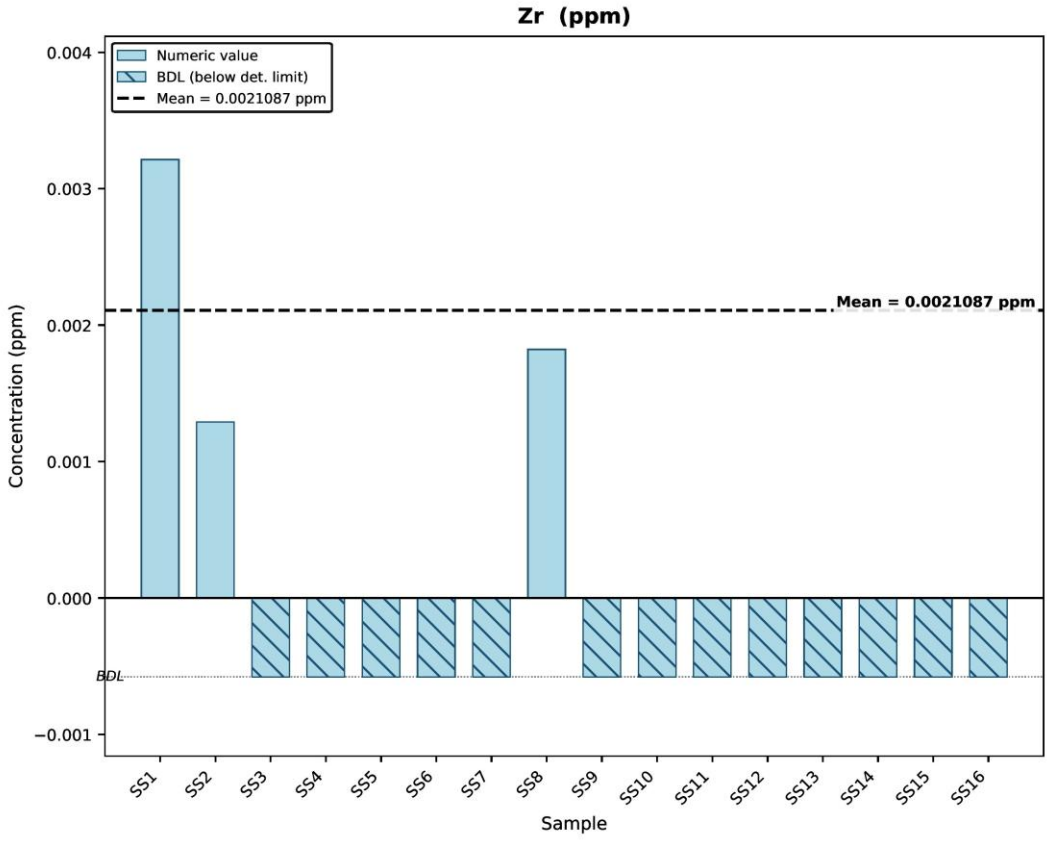


Figure 4.47 Zirconium values observed in samples

4.2.57 Uses of critical minerals

The critical minerals identified in the Oghi, Mansehra dolerites collectively underpin a vast range of modern industrial, technological, and strategic applications. Rare earth elements, including Nd, Pr, Dy, Tb, and Sm, are indispensable in the fabrication of Nd-Fe-B permanent magnets used in electric vehicle motors and wind turbine generators, while Eu, Tb, and Y serve as phosphors in LED lighting and displays, La and Ce find application in rechargeable batteries and catalytic converters, Gd functions as an MRI contrast agent, and Er and Yb are critical in fiber optic amplifiers and advanced defense systems (Binnemans et al., 2013; Graedel et al., 2015; Jowitt et al., 2018; Mancheri et al., 2019). Among the platinum group elements, Pd and Pt are primarily deployed in catalytic converters for vehicle emission control and hydrogen fuel cells, while Ir and Ru are essential in electrical contacts, hard disk

drives, and chemical catalysts, with Pd gaining increasing relevance in green energy storage (Nuss & Eckelman, 2014; USGS, 2025). Technology and energy transition metals contribute broadly across sectors; Ga is fundamental to compound semiconductors (GaAs, GaN) for 5G communications, LEDs, and radar systems (Moskalyk, 2003), Ge enables fiber optic cables, infrared optics, and night-vision devices (Werner et al., 2017), Hf is critical in nuclear reactor control rods and advanced MOSFET semiconductor gate insulators, Li drives lithium ion batteries for electric vehicles and grid-scale energy storage (Swain, 2017), Nb strengthens high-alloy steels and superconducting alloys for MRI machines (Papp, 2013), Ta is essential in electronic capacitors, jet engine superalloys, and surgical implants (Mancheri et al., 2019), and Te underpins CdTe thin film photovoltaic solar panels and thermoelectric devices (Fthenakis, 2009). In the battery and energy metals category, Co is vital for lithium-ion battery cathodes and jet turbine superalloys, Mn serves as a deoxidizer in steel and an active component in emerging battery chemistries, Ni enables stainless steel, NMC and NCA electric vehicle battery cathodes, and catalysts (Mudd, 2010), while V is foundational to vanadium redox flow batteries for grid energy storage and high strength steel alloys (Cunha et al., 2015; USGS, 2025). Among the structural and industrial critical metals, Al remains the world's most widely used non-ferrous metal across transportation, construction, and packaging, Cr is indispensable in stainless steel production and chrome plating; Cu is the cornerstone of electrical wiring, power transmission, and the global energy transition (Northey et al., 2014), Mg lightweights automotive and aerospace alloys; Ti is deployed in aerospace structures, medical implants, and TiO2 pigments, and Zn is the primary agent for galvanizing steel against corrosion (USGS, 2025). The remaining critical minerals serve equally vital roles; Ag supports electronics, photovoltaic cells, and antimicrobial medical applications, As enables GaAs and InAs semiconductor compounds for LEDs and transistors, Ba functions as a drilling mud weighting agent and medical contrast material, Be strengthens aerospace alloys and provides X-ray-transparent windows, B is integral to borosilicate glass, fiberglass, and nuclear radiation shields, K and P are the twin pillars of global fertilizer supply chains, with P additionally emerging in lithium iron phosphate (LFP) battery technology, Sb serves as a flame retardant and lead acid battery component, U fuels nuclear power plants for low-carbon electricity generation and has applications in

cancer treatment (IAEA, 2022), and Zr provides nuclear reactor fuel cladding, refractory ceramics, and dental crown materials (USGS, 2025).

4.3 Other minerals

4.3.1 Cadmium (Cd)

Cadmium was detected in 13 out of 16 samples, remaining BDL in SS6, SS8, and SS13, with a concentration range of 0.0003–0.0022 ppm and a mean of approximately 0.0012 ppm. The highest Cd was recorded in SS1 (0.0022 ppm) and SS9 (0.0021 ppm), while the lowest detectable value appeared in SS16 (0.0003 ppm), a broadly but variably distributed chalcophile trace element.

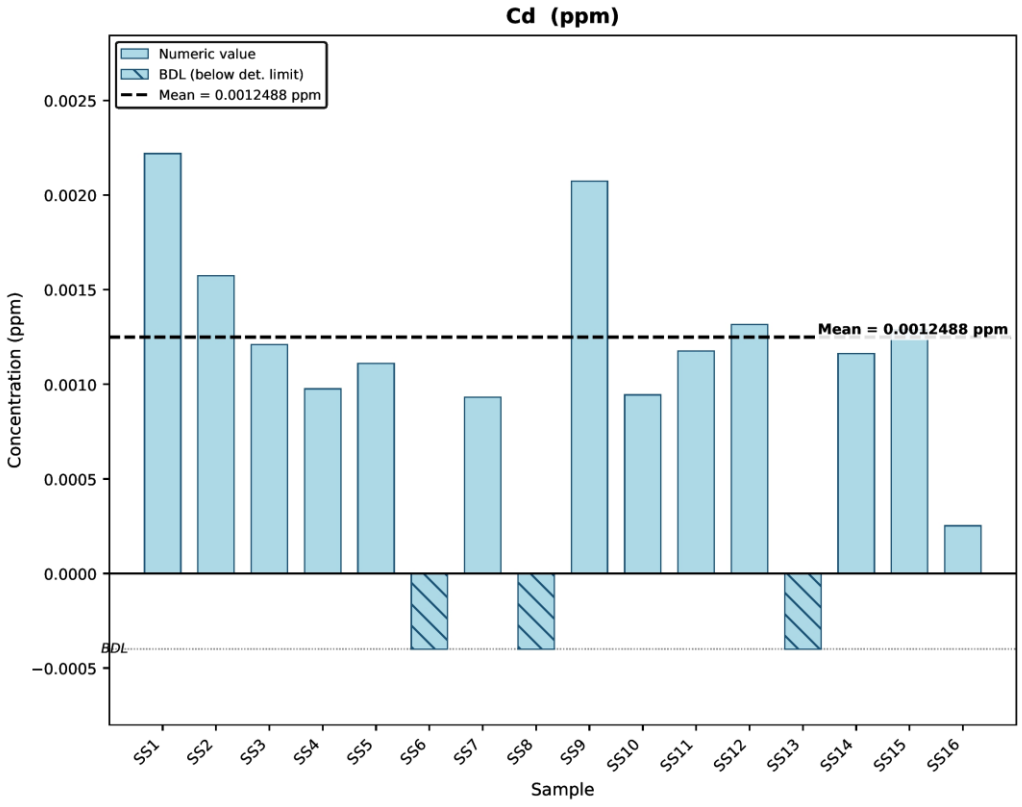


Figure 4.48 Cadmium values observed in samples

4.3.2 Calcium (Ca)

Calcium registered ADL across all 16 samples, SS1 through SS16, without exception. The universal ADL status for Ca confirms extremely elevated Ca concentrations throughout the entire sample suite, well beyond the ICP-MS calibration range, confirming that Ca bearing phases are pervasive throughout the intrusion.

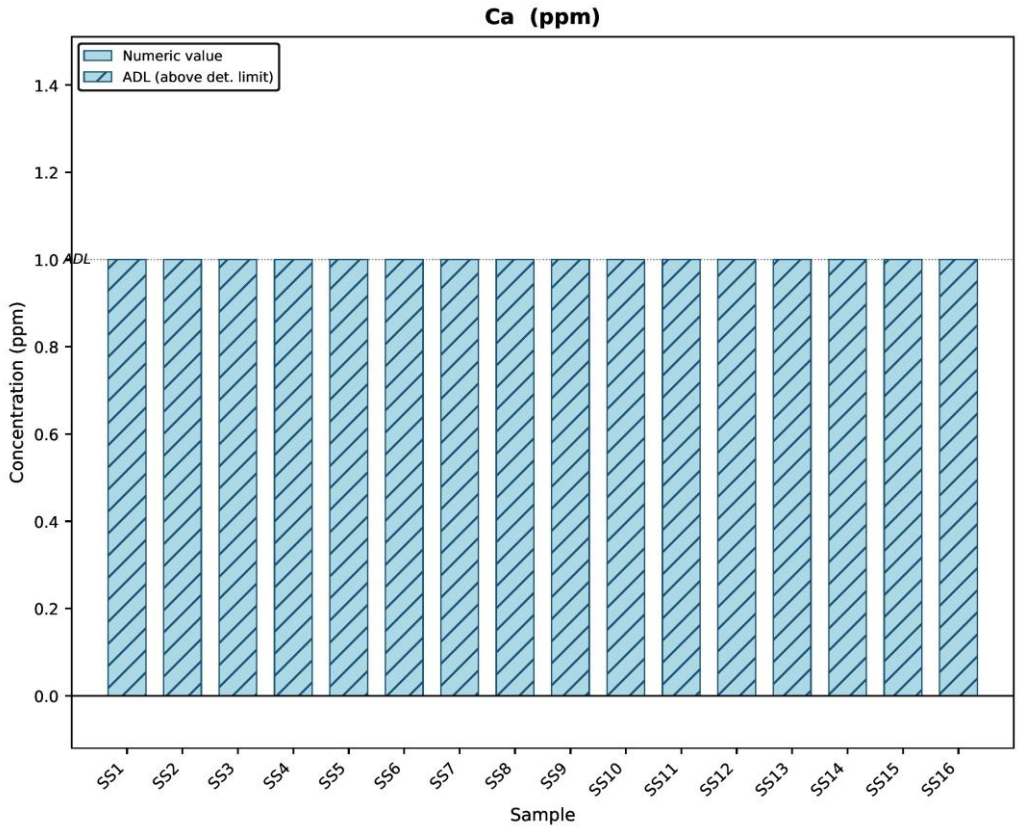


Figure 4.49 Calcium values observed in samples

4.3.3 Gold (Au)

Gold remained BDL across all 16 samples, SS1 through SS16, without exception. The universal absence of detectable Au across the entire suite, SS1 to SS16, confirms that no significant Au mineralization is present in the analyzed Oghi dolerites at detectable concentrations.

4.3.4 Iron (Fe)

Iron registered ADL in SS1 and yielded numeric values in the remaining 15 samples, with a range of 0.7980–8.2740 ppm and a mean of approximately 4.078 ppm. The highest numeric Fe was recorded in SS5 (8.274 ppm), followed by SS2 (6.848 ppm) and SS11 (6.495 ppm), while the lowest value occurred in SS14 (0.798 ppm). The ADL status in SS1 indicates that Fe in that sample exceeds the calibration range and is thus higher than even the 8.274 ppm maximum recorded in SS5, confirming Fe is a major, abundant constituent consistent with the mafic character of the rocks.

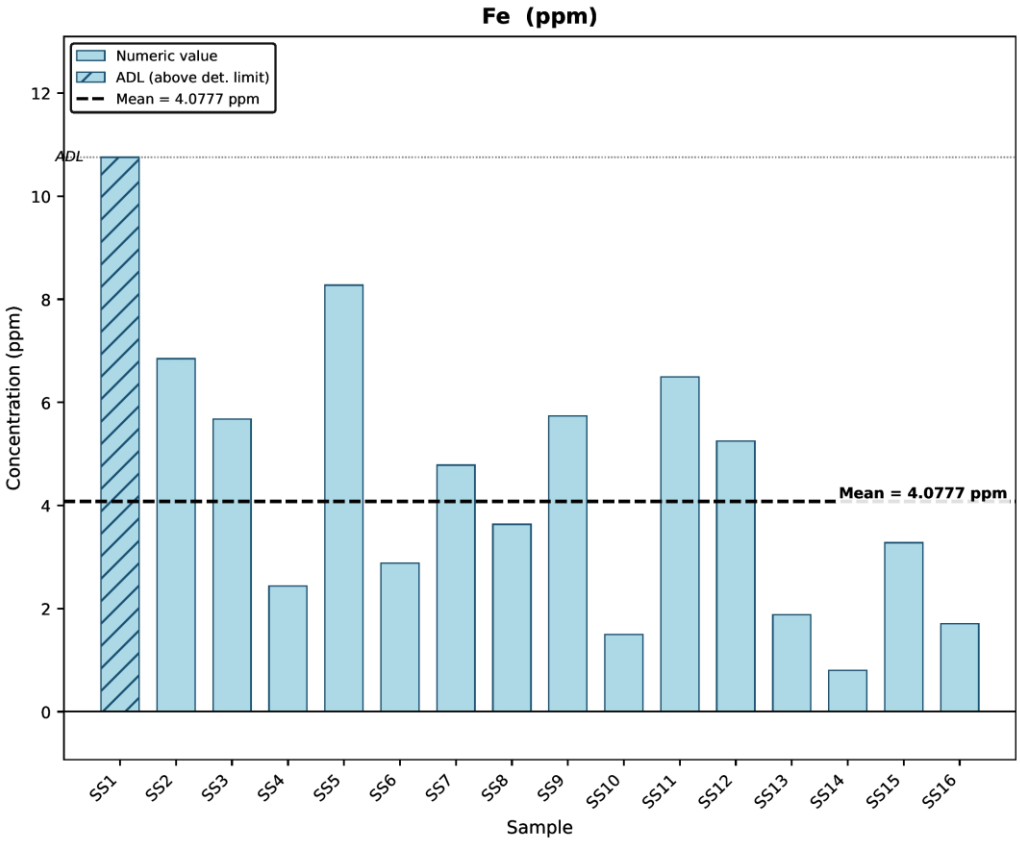


Figure 4.50 Iron values observed in samples

4.3.5 Mercury (Hg)

Mercury remained BDL across all 16 samples, SS1 through SS16, without exception.

4.3.6 Molybdenum (Mo)

Molybdenum remained BDL across all 16 samples, SS1 through SS16, without exception.

4.3.7 Selenium (Se)

Selenium remained BDL across all 16 samples, SS1 through SS16, without exception. Despite the pervasive sulfide evidence across the suite, Se is undetectable in all 16 samples, suggesting that Se-bearing phases are either absent or present well below the ICP-MS quantification limits throughout the entire Oghi dolerite intrusion.

4.3.8 Sodium (Na)

Sodium registered ADL in SS1, SS2, and SS5, and yielded numeric values in the remaining 13 samples, with a range of 0.1656–4.9304 ppm and a mean of approximately 1.297 ppm among numeric samples. The highest numeric Na was recorded in SS11 (4.930 ppm), followed by SS3 (3.607 ppm) and SS9 (1.631 ppm), while the lowest value occurred in SS14 (0.166 ppm). The ADL status in SS1, SS2, and SS5 indicates that Na in those samples exceeds the calibration range. The highest numeric Na in SS11 correlates with that sample's anomalous Ba (0.0740 ppm) and Li (0.0534 ppm), suggesting coupled alkali/incompatible-element enrichment.

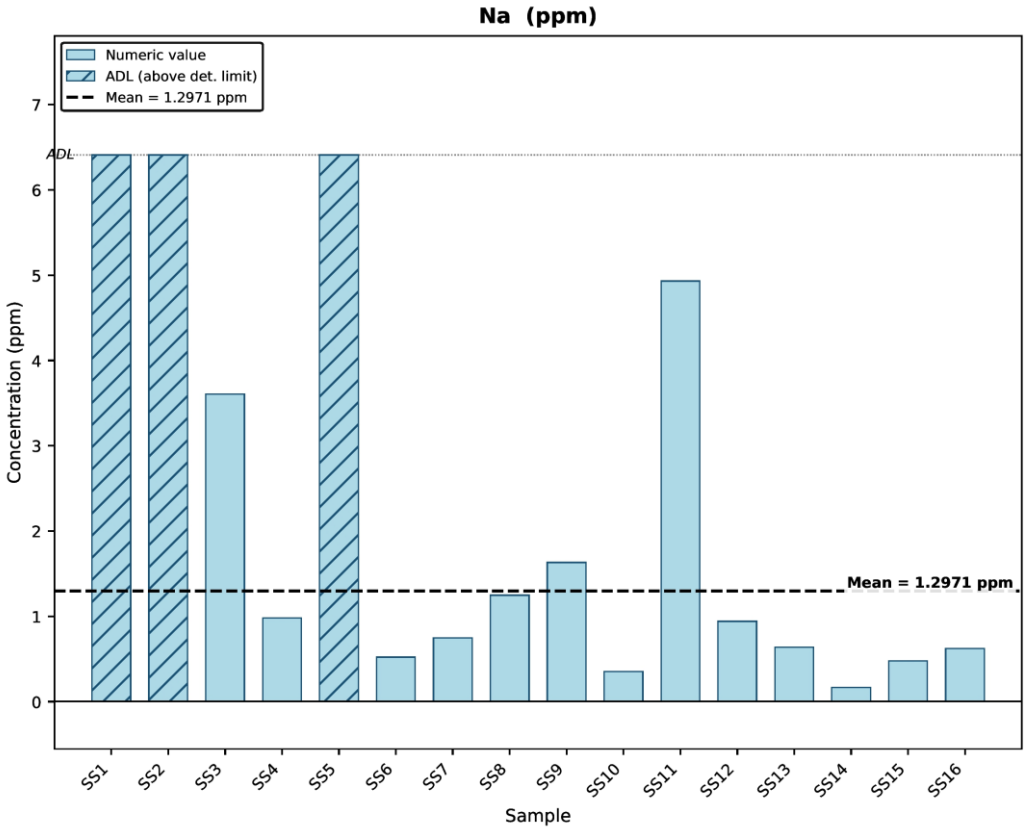


Figure 4.51 Sodium values observed in samples

4.3.9 Strontium (Sr)

Strontium was detected in 15 out of 16 samples, remaining BDL only in SS10, with a concentration range of 0.0001–0.0471 ppm and a mean of approximately 0.0131 ppm. The highest Sr was recorded in SS1 (0.0471 ppm), followed by SS2 (0.0434 ppm) and SS14 (0.0203 ppm), while the lowest detectable value appeared in SS16 (0.0001 ppm). The high Sr in SS1 and SS2 is consistent with those samples' elevated Ca (both ADL), Na, and Ba values, while the very low Sr in SS16 (0.0001 ppm) despite its moderate Na indicates heterogeneous distribution of Ca-bearing phases across the suite. The BDL status of Sr in SS10 coincides with that sample's very low values for Ba (0.0007 ppm), Mg (0.0060 ppm), Ti (0.0398 ppm), and most other elements, reinforcing SS10 as the most geochemically impoverished sample in the dataset.

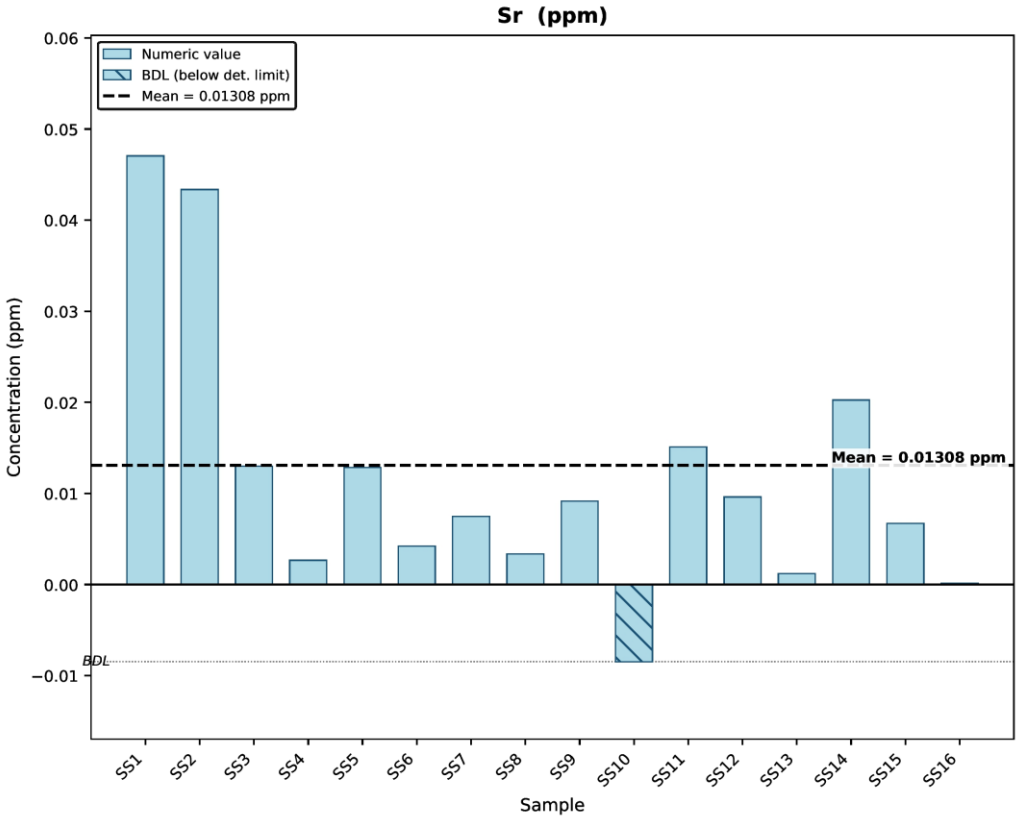


Figure 4.52 Strontium values observed in samples

4.3.10 Sulfur (S)

Sulfur registered ADL in SS1, SS2, SS3, SS5, SS8, SS9, SS10, SS13, SS15, and SS16, and yielded numeric values in SS4 (0.773 ppm), SS6 (9.705 ppm), SS7 (4.611 ppm), SS11 (2.221 ppm), SS12 (1.583 ppm), and SS14 (1.594 ppm). The highest numeric S was recorded in SS6 (9.705 ppm), followed by SS7 (4.611 ppm) and SS11 (2.221 ppm), while the lowest numeric value appeared in SS4 (0.773 ppm). The ADL status in 10 of the 16 samples indicates that S concentrations in most of the suite are very high, confirming that sulfide mineralization is pervasive throughout the Oghi dolerites rather than restricted to a single zone. The highest numeric S in SS6, which also records the highest Sb (0.0900 ppm), detectable Pt (0.0203 ppm) and Te (0.0081 ppm), and ADL K, suggests that SS6 represents a zone of particularly intense sulfide and alkali coenrichment within the intrusive body.

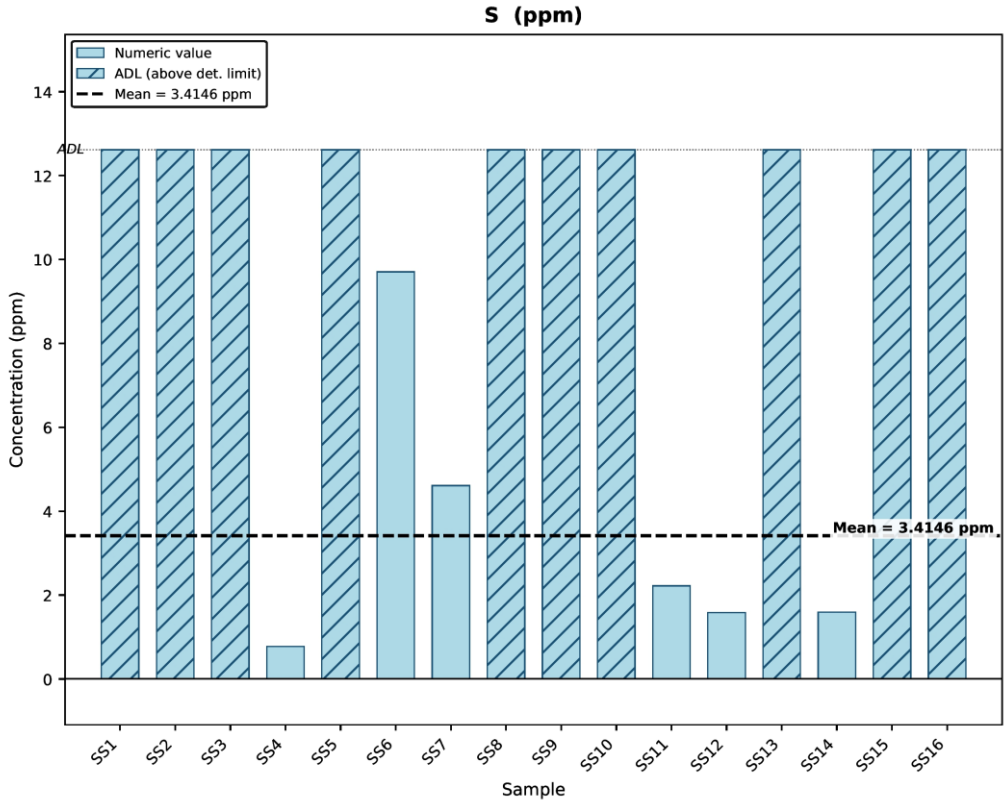


Figure 4.53 Sulfur values observed in samples

4.3.11 Thallium (Tl)

Thallium was detected in only 4 out of 16 samples, SS6 (0.0120 ppm), SS10 (0.0174 ppm), SS14 (0.0350 ppm), and SS16 (0.0353 ppm), remaining BDL in SS1, SS2, SS3, SS4, SS5, SS7, SS8, SS9, SS11, SS12, SS13, and SS15. The highest Tl was recorded in SS16 (0.0353 ppm), followed by SS14 (0.0350 ppm), while the lowest detectable value appeared in SS6 (0.0120 ppm), a restricted, low-abundance trace element with no clear spatial pattern.

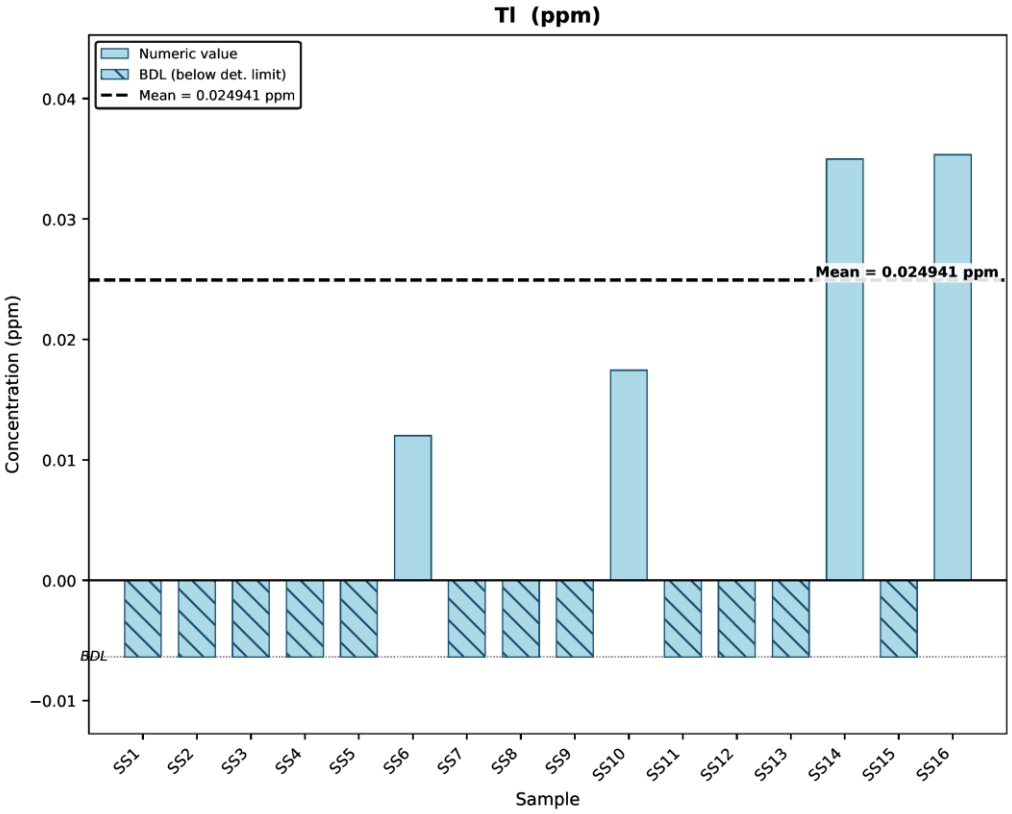


Figure 4.54 Thallium values observed in samples

4.3.12 Thorium (Th)

Thorium was detected in all 16 samples with a concentration range of 0.0037–0.0251 ppm and a mean of approximately 0.0140 ppm. The highest Th was recorded in SS1 (0.0251 ppm), followed by SS2 (0.0204 ppm) and SS9 (0.0188 ppm), while the lowest values occurred in SS10 (0.0037 ppm) and SS3 (0.0062 ppm), highest in SS1, broadly tracking that sample's overall enrichment.

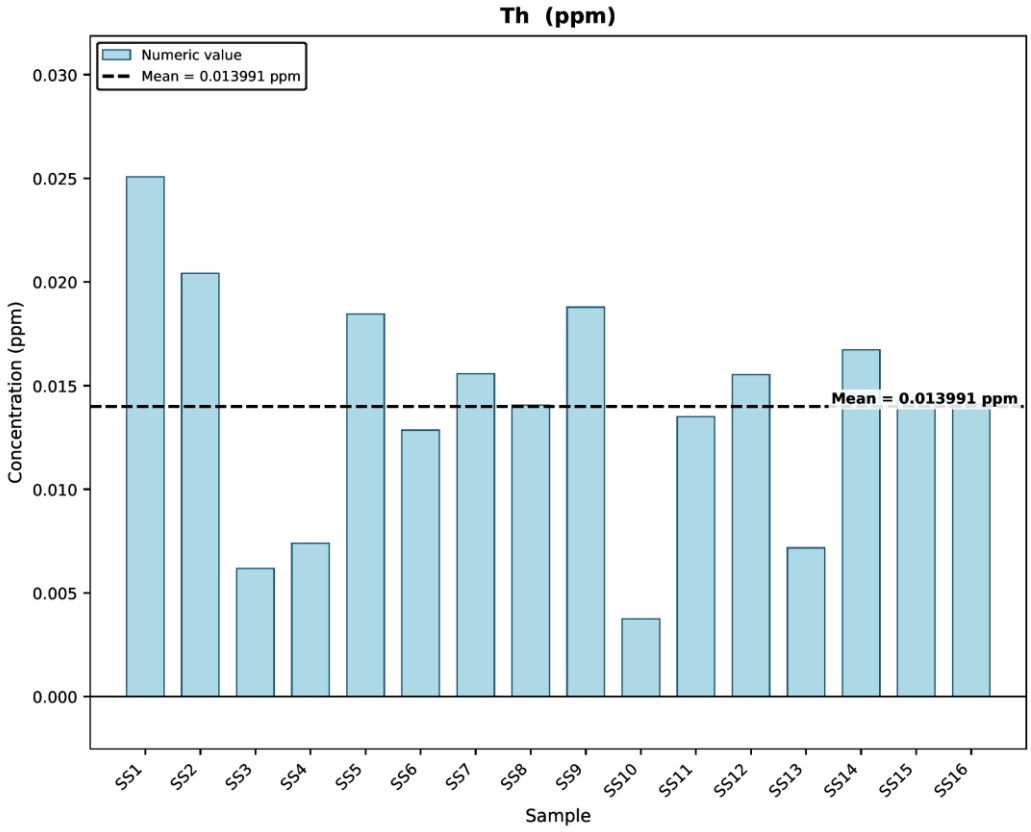


Figure 4.55 Thorium values observed in samples

4.3.13 Uses of other minerals

The noncritical minerals detected in the Oghi, Mansehra dolerites likewise serve a broad and economically significant spectrum of industrial and technological applications. Fe, as the world's most widely used metal, forms the basis of global steel production for construction, infrastructure, transportation, and machinery, with Fe-Ti oxide minerals additionally serving as raw materials for both iron and titanium production (USGS, 2025). Ca compounds are equally pervasive, underpinning construction materials such as lime, cement, and gypsum, as well as agricultural soil amendment, steelmaking flux, and water treatment processes, while Na compounds, including NaCl for food preservation, NaOH for pulp and paper industries, Na2CO3 for glass manufacturing, and NaHCO3 for food and pharmaceutical applications are ranked among the most commercially produced chemicals worldwide (USGS, 2025).

S drives the production of sulfuric acid (H2SO4), the single most manufactured industrial chemical globally, which is indispensable in fertilizer production, petroleum refining, metal smelting, and chemical synthesis, with elemental S additionally applied in rubber vulcanization, fungicides, and pharmaceuticals (USGS, 2025). Au serves critical functions in jewelry, electronics such as connectors and bonding wire, central bank monetary reserves, dentistry, medical applications, and as a reflective coating in space technology, while Cd, despite its declining use due to toxicity concerns, has historically contributed to NiCd rechargeable batteries, electroplating, and pigments, with lithium-ion technologies progressively replacing it in most applications (Nuss & Eckelman, 2014; USGS, 2025). Hg has been employed in fluorescent lamps, thermometers, dental amalgam, artisanal gold mining, and chlor-alkali production, though its global use is being systematically phased out under the Minamata Convention (UNEP, 2019), and Mo serves as an alloying agent in high-temperature-resistant steels, a catalyst in petroleum hydrodesulfurization, and a solid lubricant in the form of MoS2 (Papp, 2014; USGS, 2025). Se finds application across glass manufacturing, xerography, nutritional supplements, and photovoltaic semiconductors including CIS solar cells; Sr contributes to pyrotechnics, ferrite magnets, ceramics, and bone cancer radiotherapy via 89Sr; Th is utilized in gas mantles, high-temperature ceramics, tungsten welding alloys, and holds significant potential as a nuclear fuel in thorium fuel cycle reactors (IAEA, 2005; USGS, 2025); and Tl, despite being highly toxic and tightly regulated, finds niche applications in Tl based superconductors, infrared detectors, specialized optical glass, and 201Tl cardiac imaging in nuclear medicine (USGS, 2025).

CHAPTER 5

DISCUSSION

5.1 Discussion

The geochemical data obtained through ICP-MS analysis of the sixteen dolerite samples from Oghi, Mansehra reveals a complex and geochemically diverse mafic intrusive suite whose trace element systematics invite meaningful comparison with both the regional geological framework and broader global analogues of mafic hosted critical mineral systems. The findings not only add a new dimension to the existing understanding of the Oghi, Mansehra geological domain but also highlight the prospective significance of these intrusions within the context of critical mineral exploration in northern Pakistan.

The regional geological setting of the Masehra, Hazara area has been progressively refined since the foundational lithostratigraphic work of Calkins et al. (1975), who recognized the Tanawal Formation and the intrusive granitoids of Mansehra as key stratigraphic and structural elements of the Hazara Basin. The tectonic synthesis of Tahirkheli (1979) established the broader context of Indian plate convergence with Eurasian terrains, while Treloar and Izatt (1993) emphasized thrust stacking and crustal thickening as the dominant mechanisms of orogenic evolution across the Himalayan collision zone.

DiPietro and Pogue (2004) subsequently provided refined tectonostratigraphic subdivisions of the western Himalaya and identified localized shear zones of which the most relevant being the the Oghi Shear Zone as probable structural controls on mafic dyke emplacement in the region. This structural context is directly pertinent to the present study, as the spatial distribution of the 16 analyzed dolerite samples likely reflects emplacement along this shear zone. The geochemical heterogeneity observed across the sample suite, most dramatically in the nearly 355 fold inter sample variation in Mg concentrations (SS14: 0.0046 ppm to SS1: 1.6211 ppm) and the approximately 18 fold variation in both V (SS14: 0.0664 ppm to SS1: 1.1613 ppm) and Mn (SS16: 0.0194 ppm to SS1: 0.3436 ppm), may partly reflect structural compartmentalization of magma batches during emplacement along this shear corridor.

The petrogenetic context of the Mansehra Granitic Complex, within which the Oghi dolerites are emplaced, was established through geochronological and geochemical investigations of Naeem et al., (2016, 2021), who confirmed an Early Paleozoic emplacement age (466–478 Ma) using U-Pb zircon geochronology and documented strongly peraluminous, S-type, calcalkaline geochemical signatures reflecting crustal melting of the Tanawal Formation protolith.

Mehmood et al., (2022) further investigated the REE mineralization potential of the Mansehra Granitic Complex and reported that despite geochemical indicators of extensive fractionation, including strong negative Eu, Ba, Nb, Ti, and Zr anomalies, the granitic complex is broadly barren in terms of REE and strategic metal mineralization, owing to the dominance of muscovite and biotite over REE concentrating accessory phases during partial melting. This finding is significant for contextualizing the present study; the REE poor character of the associated granites contrasts sharply with the systematic REE signatures documented in the Oghi dolerites, confirming that the two magmatic suites represent geochemically and petrogenetically independent systems where one derived from crustal melting, the other from a mantle source.

Ismaeel et al. (2019) conducted the most direct prior investigation of the Oghi, Mansehra dolerites, describing them as fine to medium grained rocks displaying ophitic to subophitic textures, with plagioclase and clinopyroxene as dominant mineral phases and opaques, quartz, biotite, amphibole, olivine, apatite, chlorite, orthopyroxene, and epidote constituting minor to accessory phases. Geochemically, they characterized the dolerites as subalkalic, metaluminous, tholeiitic to transitionally alkalic, with elevated TiO2 contents and a ferroan character, and evaluated their physico-mechanical suitability for construction use. While this work constituted a meaningful petrological contribution, it explicitly did not extend to trace element systematics or critical mineral assessment, which is a gap that the present study directly addresses.

The comparison with similar mafic intrusions in the broader northern Pakistan hinterland, particularly the rift related basic dykes of the Malka area documented by Majid et al. (1991), provides important tectonic context for the Oghi dolerites. Majid et al. (1991) interpreted the Malka dykes as Permian rift related intrusions emplaced during extensional tectonism associated with the breakup of Gondwana and the opening of the Neo-Tethys Ocean along the northwestern Indian plate margin, deriving from the subcontinental lithospheric mantle source. This interpretation directly informs the tectonic setting of the Oghi dolerites; the predominantly BDL Cr across 11 of 16 samples, the moderate Nb concentrations (up to 0.1292 ppm in SS2), the near universal detection of V and Ti throughout all 16 samples, and the absence of subduction related geochemical signatures such as strong Nb-Ta depletion are collectively consistent with within plate to post collisional intraplate mafic magmatism rather than arc related magmatism, aligning with the extensional origin proposed by Majid et al. (1991) for analogous mafic intrusions in the region.

Internationally, mafic and ultramafic intrusions are well established as hosts of magmatic sulfide and REE mineralization. The mechanisms by which sulfide liquid immiscibility, crystal accumulation, and late stage hydrothermal redistribution can produce economically viable concentrations of Ni, Cu, Co, and REEs in mafic magmatic ore systems have been comprehensively described by Naldrett (2013) and

Robb (2013, 2020). Naldrett (2013) established that the formation of magmatic Ni-Cu-PGE sulfide ore fundamentally depends on the attainment of sulfide liquid immiscibility within the primary magma, a process that is triggered by silica enrichment through crustal assimilation, pressure decrease during magma ascent, or mixing of compositionally distinct magma batches, and that the PGE budget of resulting sulfide ore is governed by the sulfide silicate R-factor at the time of sulfide saturation.

Robb (2013) further described how the distribution of economically significant mineral deposits across diverse tectonic settings, from the collisional orogens to rift environments, reflects the fundamental controls of magmatic differentiation, fluid rock interaction, and structural focusing on ore forming processes, emphasizing that mafic intrusions in collisional orogen settings can host economically significant critical mineral enrichment when mantle derived magmas interact with S-bearing or incompatible element enriched crustal lithologies during emplacement.

The Rare Earth Element (REE) mineralization in post collisional alkaline magmatic systems of northern Pakistan was documented for the first time by Hussain et al. (2020), who identified REE mineralized syenite and associated pegmatite within the Kohistan Batholith at Tangir Darel, with U-Pb zircon ages of 30–31 Ma confirming emplacement during post collisional magmatism triggered by slab break off and asthenospheric upwelling. The demonstration by Hussain et al. (2020) that post collisional mantle derived alkaline magmatic systems along the Tethyan orogen can generate economic Rare Earth Element (REE) concentrations through prolonged fractional crystallization provides a directly applicable geodynamic framework for the Oghi dolerites. The localized Light Rare Earth Elements (LREE) enrichment detected in SS8 (Pr: 0.1100 ppm; Ce: 0.0928 ppm) and SS5 (Pr: 0.1071 ppm) alongside near, universal detection of Eu, Gd, Y, Tm, and Nd across the sample suite, combined with universally ADL phosphorus, are consistent with the REE enrichment mechanisms described by Hussain et al. (2020), wherein late stage fractional crystallization concentrates REEs in residual melts and fluid phases within structurally focused

zones of the intrusive body. The methodological validation provided by Hussain et al. (2020), demonstrates the effectiveness of ICP-MS based trace element analysis for assessing REE mineralization potential in northern Pakistan magmatic systems, further supports the analytical approach adopted in the present study. Similarly, Mehmood et al. (2022), using the same ICP-MS based geochemical framework for the Mansehra Granitic Complex, established a comparative geochemical baseline that allows the critical mineral potential of the Oghi dolerites to be evaluated against their granitic host rock suite, a comparison that strongly favors the mafic intrusions as the more geochemically prospective of the two for REE and PGE mineralization.

The geochemical characteristics of the Oghi, Mansehra dolerites documented in the present study both corroborate and significantly extend the prior findings of Ismaeel et al. (2019), although the ppm values obtained in the current data set are not economically viable. The universally elevated Ti (range: 0.0391–0.7035 ppm; highest in SS2 at 0.7035 ppm; mean: 0.193 ppm), the pervasive Fe enrichment (numeric range up to 8.274 ppm in SS5, with SS1 recording ADL), and the consistently high V across all 16 samples (range: 0.0664 ppm in SS14 to 1.1613 ppm in SS1; mean: 0.294 ppm) collectively reinforce the ferroan, TiO2 enriched tholeiitic affinity identified by Ismaeel et al. (2019) and extend it into the trace element domain for the first time. However, the present data reveal geochemical dimensions absent from Ismaeel et al.'s (2019) dataset, most critically the near universal PGE enrichment, Pd detected in 15 of 16 samples (range: 0.0185 ppm in SS5 to 0.1873 ppm in SS2; Pd/Pt >1 in all co-detectable sample pairs), Pt in 11 of 16 samples (up to 0.0213 ppm in SS10), alongside pervasive Cu across all 16 samples (maximum: 0.5458 ppm in SS5; mean: 0.239 ppm) and widespread high S (ADL in 10 of 16 samples; highest numeric value of 9.705 ppm in SS6). These features define a sulfide bearing mafic system with economic mineral potential far exceeding what could be inferred from the engineering focused dataset of Ismaeel et al. (2019).

The mineralogical and geochemical baseline established by Naeem et al. (2021) for the Mansehra Granitic Complex provides a critical comparative framework for the present study. While Naeem et al. (2021) confirmed the broadly barren REE

character of the MGC, attributing the low REE to muscovite and biotite dominated melting rather than REE concentrating accessory phase crystallization, the present data reveal a systematically contrasting trace element signature in the associated dolerites which is non-economic but meaningful; universal Eu (0.0025–0.0078 ppm), Gd (0.0052–0.0480 ppm), Y (0.0005–0.0070 ppm), and Tm (0.0011–0.0066 ppm) across all 16 samples; near universal Nd (14 of 16; up to 0.0455 ppm in SS2) and Th (all 16; up to 0.0251 ppm in SS1); localized Pr enrichment in SS8 (0.1100 ppm) and SS5 (0.1071 ppm); elevated Nb in SS2 (0.1292 ppm) and SS1 (1.0064 ppm); and universally ADL P. This contrast confirms that the dolerites represent an independent mantle derived geochemical system that must be assessed separately from and holds greater critical mineral prospectivity than the cooccurring granitic suite.

The global analogue framework established by Naldrett (2013) for magmatic sulfide deposits, encompassing world class Ni-Cu-PGE systems including the Bushveld Complex of South Africa and the Noril'sk-Talnakh intrusions of Russia, provides the most directly applicable process model for interpreting the sulfide related geochemical signature of the Oghi dolerites. The pervasive high S (ADL in SS1, SS2, SS3, SS5, SS8, SS9, SS10, SS13, SS15, and SS16; highest numeric value of 9.705 ppm in SS6), universal Cu enrichment (maximum: 0.5458 ppm in SS5; mean: 0.239 ppm), near-universal Pd (mean: 0.088 ppm; maximum: 0.1873 ppm in SS2), Pt in 11 samples, and co-occurrence of chalcophile elements Te, Ag, and Sb across most of the sample suite are consistent with Naldrett's (2013) framework for pervasive disseminated sulfide mineralization driven by mantle-derived mafic magma attaining sulfide saturation through interaction with S-bearing crustal lithologies during emplacement. While the Oghi dolerites are not large layered intrusions of Bushveld scale, Naldrett (2013) explicitly established that even small mafic intrusions emplaced in structurally controlled corridors within collisional orogen settings can develop sulfide saturation and associated PGE-Cu enrichment when appropriate conditions are met, a process level analogy directly applicable to the Oghi Shear Zone controlled dolerite emplacement. The Pd/Pt ratios greater than 1 in all 11 co-detectable sample pairs, ranging from 1.96 in SS11 to 25.61 in SS13, and the wide Pd range (0.019–0.187 ppm) are consistent with the variable R-factor (sulfide-silicate ratio) effects

described by Naldrett (2013) as governing PGE budget in disseminated sulfide ore systems.

Robb (2013) similarly established that the tectonic position of an intrusion within a collisional orogen, as is the case for the Oghi dolerites within the Lesser Himalayan Zone, does not preclude significant critical mineral enrichment; on the contrary, the interaction of mantle derived magmas with structurally complex, geochemically diverse crustal lithologies during emplacement in such settings can enhance chalcophile element and REE concentrations through multiple fluid rock interaction and fractional crystallization episodes, consistent with the heterogeneous geochemical distribution observed across the 16 Oghi samples. Naldrett (2013) further emphasized that even relatively modest mafic intrusive systems, not requiring Bushveld scale dimensions, can develop significant PGE and Cu-Ni mineralization when the primary magma assimilates external sulfur from country rocks, a mechanism fully consistent with the interaction of the Oghi dolerite magmas with the S-bearing Precambrian metasedimentary lithologies of the Tanawal Formation during ascent and emplacement along the Oghi Shear Zone.

In summary, the present dataset does not indicate economic mineralization of critical minerals within the Oghi Dolerites, it does reveal detectable, localized intra-formational enrichment anomalies that shed light on trace element behavior, lay the groundwork for more detailed follow-up work. In this sense, the study represents an early reconnaissance geochemical characterization of the Dolerites present in Oghi, Mansehra, though its implications for resource potential remain preliminary and non-economic, requiring further substantiation through additional sampling, mineralogical characterization, and economic screening.

CONCLUSIONS

The ICP MS geochemical analysis of sixteen dolerite samples from Oghi, Mansehra has successfully identified a diverse and geochemically meaningful assemblage of both critical and non critical minerals within this previously under characterized mafic intrusive suite. The data collectively demonstrate that the Oghi dolerites are not geochemically inert mafic rocks but rather carry meaningful concentrations of critical minerals including, PGE's, most notably palladium (mean 0.087978 ppm), platinum (mean 0.014964 ppm), ruthenium (mean 0.031033 ppm), and iridium (mean 0.013452 ppm), alongside pervasive copper (mean 0.238552 ppm) and sulfur (mean 3.41457 ppm) enrichment, universal vanadium (mean 0.294213 ppm) and titanium (mean 0.192896 ppm) detection, consistent rare earth element signatures, and elevated concentrations of niobium (mean 0.036781 ppm), Rubidium (mean 0.25106 ppm), gallium (mean 0.089724 ppm), lithium (mean 0.018594 ppm), and uranium (mean 0.128443 ppm), all of which are minerals of strategic and economic relevance under the USGS 2025 critical minerals framework. The overall geochemical character of the suite is consistent with a within plate to post collisional extensional tectonic setting, broadly comparable to the Permian rift related mafic intrusions of the broader northwestern Indian plate margin, and reflects a primary mantle derived magmatic system that underwent variable crustal interaction, fractional crystallization, and localized sulfide saturation during emplacement. The marked compositional heterogeneity across the 16 samples, best illustrated by the extreme inter sample variation in Mg, Fe, V, Mn, Cu, Pd, and Al, indicates that the intrusive body is internally diverse and that specific zones, particularly sample SS5 with its anomalous Cu-As-Ir-Fe signature, may represent locally enriched targets of particular mineralogical interest. Collectively, these results confirm that the Dolerites from Oghi, Mansehra have the capacity to host critical minerals, however, given the low absolute concentrations recorded, the findings remain at a reconnaissance level and do not by themselves point to economic mineralization. They should therefore be

regarded as a preliminary baseline, pending confirmation of adequate grade and tonnage for economic viability.

RECOMMENDATIONS

Future work should extend sampling beyond the present 16 specimens, focusing on fresh specimens and denser coverage around the SS5 anomaly to determine whether it represents a localized feature or a broader regional trend, and these new samples could be analyzed using a different four-acid total digestion technique as opposed to aqua regia used in this study, with results cross-checked against XRF and ICP-OES to obtain properly quantified concentrations of major and abundant elements. Mineralogy should be resolved using XRD and SEM-EDS to identify the dominant mineral phases, while electron microprobe analysis could identify the specific mineral sites where critical minerals are concentrated.

In summary, no determination of economic viability can be made until further data establish adequate grade, tonnage, spatial continuity, and mineral recoverability, together with a reasonable prospect of economic extraction, in conformity with established mineral resource reporting standards.

REFERENCES

Ali, S. H., Giurco, D., Arndt, N., Nickless, E., Brown, G., Demetriades, A., … Yakovleva, N. (2017). Mineral supply for sustainable development requires resource governance. Nature, 543(7645), 367–372.

Awan, R. S., Khan, A., Liu, C., Yang, S., Zang, Q., Wu, Y., Li, G., Iltaf, K. H., Tahir, M. and Ali, S. (2021). Subsurface geological model of sedimentary and metasedimentary wedge from Mansehra to Battal based on gravity data, Hazara area, Pakistan. Energy Geoscience, 2(4), 229-237.

Baig, M. S., & Lawrence, R. D. (1987). Precambrian to early Paleozoic orogenesis in the Himalaya, Kashmir. Kashmir Journal of Geology, 5, 1–22.

Balaram, V. (2021). Strategies to overcome interferences in elemental and isotopic geochemical analysis by quadrupole inductively coupled plasma mass spectrometry: A critical evaluation of the recent developments. Rapid Communications in Mass Spectrometry, 35(10), e9065.

Becker, J. S. (2007). Inorganic mass spectrometry: Principles and applications. John Wiley & Sons.

Binnemans, K., Jones, P. T., Blanpain, B., Van Gerven, T., Yang, Y., Walton, A., & Buchert, M. (2013). Recycling of rare earths: A critical review. Journal of Cleaner Production, 51, 1–22.

Bossart, P., Dietrich, D., Greco, A., Ottiger, R., & Ramsay, J. G. (1988). The tectonic structure of the Hazara-Kashmir Syntaxis, southern Himalayas, Pakistan. Tectonics, 7(2), 273–297.

Calkins, J. A., Offield, T. W., Abdullah, S. K., & Ali, S. T. (1975). Geology of the southern Himalaya in Hazara, Pakistan, and adjacent areas (USGS Professional Paper 716-C).

Crawford, M. B., & Searle, M. P. (1992). Field relationships and geochemistry of pre-collisional (India-Asia) granitoid magmatism in the central Karakoram, northern Pakistan. Tectonophysics, 206(1–2), 171–192.

Cunha, Á., Martins, J., Rodrigues, N., & Brito, F. P. (2015). Vanadium redox flow batteries: A technology review. *International Journal of Energy Research, 39(7), 889–918.

DiPietro, J. A., & Pogue, K. R. (2004). Tectonostratigraphic subdivisions of the Himalaya: A view from the west. Tectonics, 23(5).

Fthenakis, V. (2009). Sustainability of photovoltaics: The case for thin-film solar cells. Renewable and Sustainable Energy Reviews, 13(9), 2746–2750.

Graedel, T. E., Harper, E. M., Nassar, N. T., Nuss, P., & Reck, B. K. (2015). Criticality of metals and metalloids. Proceedings of the National Academy of Sciences, 112(14), 4257–4262.

Hall, G. E. M., & Plant, J. A. (1992). Analytical errors in the determination of high field strength elements and their implications in tectonic interpretation studies. Chemical Geology, 95(1–2), 141–156.

Hussain, A., Zhao, K. D., Arif, M., Palmer, M. R., Chen, W., Zhang, Q., … Girei, M. B. (2020). Geochronology, mineral chemistry and genesis of REE mineralization in alkaline rocks from northern Pakistan. Ore Geology Reviews, 126, 103749.

Hussain, I., Li, Z.-C., Fida, M., Hussain, J., Hussain, W., Pei, X.-Z., Yang, Y.-J., Wang, M., Li, R.-B., Pei, L., & Lin, H. (2024). Sub-Himalayan Mesozoic-Cenozoic tectonic-stratigraphic properties and deformation features in the western limb of Hazara Kashmir syntaxis, Pakistan. Arabian Journal of Geosciences, 17, 16.

International Atomic Energy Agency (IAEA). (2005). Thorium fuel cycle — Potential benefits and challenges (IAEA-TECDOC-1450).

International Atomic Energy Agency (IAEA). (2022). Nuclear power reactors in the world (Reference Data Series No. 2, IAEA-RDS-2/42). IAEA.

Ismaeel, M., Anjum, M. N., Ahmed, W., Hussain, A., & Sajid, M. (2019). Petrography, geochemistry and physico-mechanical properties of dolerite from

Oghi (Mansehra), Khyber Pakhtunkhwa, Pakistan. Journal of Himalayan Earth Sciences, 52(2), 185–196.

Jarvis, I., & Jarvis, K. E. (1992). Plasma spectrometry in the earth sciences: Techniques, applications and future trends. Chemical Geology, 95(1–2), 1–33.

Jowitt, S. M., Mudd, G. M., Werner, T. T., Weng, Z., Barkoff, D. W., & McCaffrey, D. (2018). The critical metals: An overview and opportunities and concerns for the future.

Jowitt, S. M., Werner, T. T., Weng, Z., & Mudd, G. M. (2018). Recycling of the rare earth elements. Current Opinion in Green and Sustainable Chemistry, 13, 1–7.

Kashani, A., & Mostaghimi, J. (2010). Aerosol characterization of concentric pneumatic nebulizer used in inductively coupled plasma—Mass spectrometry (ICP-MS). Atomization and Sprays, 20(5).

Khyber Pakhtunkhwa Minerals Development Department. (n.d.). Follow-up exploration targets: Hazara Division reconnaissance report. Government of Khyber Pakhtunkhwa.

Le Bas, M. J., Mian, M. J. I., & Rex, D. C. (1987). Age and nature of carbonatite emplacement in North Pakistan. International Journal of Earth Sciences, 76, 317–323.

Majid, M., Danishwar, S., & Hamidullah, S. (1991). Petrographic and chemical variations in the rift-related basic dykes of the Malka area (Lower Swat), NWFP, Pakistan. Geological Bulletin, University of Peshawar, 24, 1–23.

Mancheri, N. A., Sprecher, B., Bailey, G., Ge, J., & Tukker, A. (2019). Effect of Chinese policies on rare earth supply chain resilience. Resources, Conservation and Recycling, 142, 101–112.

Mehmood, A., Agheem, M. H., & Shaikh, A. J. (2022). Geochemical characteristics of Mansehra Granitic Complex, NW Himalayas, Pakistan: Implications for rare earth element mineralization potential. Authorea Preprints.

Meigs, J. A., Burbank, W. D., & Beck, A. R. (1995). Middle-late Miocene (>10 Ma) formation of the Main Boundary thrust in the western Himalaya. Geology, 23(5), 423–426.

Moskalyk, R. R. (2003). Gallium: The backbone of the electronics industry. Minerals Engineering, 16(10), 921–929.

Mudd, G. M. (2010). The environmental sustainability of mining in Australia: Key mega-trends and looming constraints. Resources Policy, 35(2), 98–115.

Naeem, M., Burg, J. P., Ahmad, N., Chaudhry, M. N., & Khalid, P. (2016). U-Pb zircon systematics of the Mansehra Granitic Complex: implications on the early Paleozoic orogenesis in NW Himalaya of Pakistan. Geosciences Journal, 20(4), 427-447.

Naeem, M., Khalid, P., & Anwar, A. W. (2015). Construction material prospects of granitic and associated rocks of Mansehra area, NW Himalaya, Pakistan. Acta Geodaetica et Geophysica, 50(3), 307-319.

Naeem, M., Zafar, T., Chaudhry, M. N., Burg, J. P., Ahmad, N., & Rehman, H. U. (2021). Mineralogy and geochemistry of calc-alkaline magmatic rocks from the Mansehra Granitic Complex, NW Himalaya, Pakistan: insights into petrogenesis and tectonic setting. Arabian Journal of Geosciences, 14(13), 1279.

Naldrett, A. J. (2004). Magmatic sulfide deposits: Geology, geochemistry and exploration. Springer.

Naldrett, A. J. (2010). From the mantle to the bank: The life of a Ni-Cu-(PGE) sulfide deposit. South African Journal of Geology, 113(1), 1–32.

Naldrett, A. J. (2013). Magmatic sulfide deposits: Geology, geochemistry and exploration. Springer.

Northey, S., Mohr, S., Mudd, G. M., Weng, Z., & Giurco, D. (2014). Modelling future copper ore grade decline based on a detailed assessment of copper resources and mining. Resources, Conservation and Recycling, 83, 190–201.

Nuss, P., & Eckelman, M. J. (2014). Life cycle assessment of metals: A scientific synthesis. PLOS ONE, 9(7), e101298.

Papp, J. F. (2013). Niobium (columbium): 2011 minerals yearbook. U.S. Geological Survey.

Papp, J. F. (2014). Molybdenum: 2012 minerals yearbook. U.S. Geological Survey.

Potts, P. J. (1987). A handbook of silicate rock analysis. Blackie & Son.

Qasim, M., Ding, L., Khan, M. A., Jadoon, I. A. K., Haneef, M., Baig, M. S., Imraz, M., & Cai, F. (2018). Tectonic implications of detrital zircon ages from Lesser Himalayan Mesozoic-Cenozoic strata, Pakistan. Geochemistry, Geophysics, Geosystems, 19(6), 1786–1811.

Qasim, M., Khan, M. A., & Haneef, M. (2014). Stratigraphic characterization of the Early Cambrian Abbottabad Formation in the Sherwan area, Hazara region, N. Pakistan: Implications for Early Paleozoic stratigraphic correlation in NW Himalayas, Pakistan. Journal of Himalayan Earth Sciences, 47(1), 25–40.

Robb, L. (2013). Introduction to ore-forming processes. John Wiley & Sons.

Robb, L. (2020). Introduction to ore-forming processes. John Wiley & Sons.

Searle, M. P. (1991). Geology and tectonics of the Karakoram Mountains. John Wiley and Sons.

Searle, M. P., Khan, M. A., Fraser, J. E., Gough, S. J., & Jan, M. Q. (1999). The tectonic evolution of the Kohistan-Karakoram collision belt along the Karakoram Highway transect, north Pakistan. Tectonics, 18(6), 929–949.

Swain, B. (2017). Recovery and recycling of lithium: A review. Separation and Purification Technology, 172, 388–403.

Tahirkheli, R. A. K. (1979). Geology of Kohistan and adjoining Eurasian and Indo-Pakistan continents, Pakistan. Geological Bulletin of the University of Peshawar, 11, 1–30.

Tahirkheli, R. K., & Majid, M. (1977). Geology of the Tanawals in the southwest Tanawal and Gandghar Range, Hazara, Pakistan. Journal of Himalayan Earth Sciences, 9(1), 1-21.

Taylor, C. D., & Theodorakos, P. M. (2002). Rock sample preparation (U.S. Geological Survey Open-File Report 02-0223, Chapter A1). U.S. Geological Survey.

Thomas, R. (2013). Practical guide to ICP-MS: A tutorial for beginners (3rd ed.). CRC Press. ISBN: 9781466555433.

Totland, M., Jarvis, I., & Jarvis, K. E. (1992). An assessment of dissolution techniques for the analysis of geological samples by plasma spectrometry. Chemical Geology, 95(1–2), 35–62.

Treloar, P. J., & Izatt, C. N. (1993). Tectonics of the Himalayan collision between the Indian Plate and the Afghan Block: A synthesis. In P. J. Treloar & M. P. Searle (Eds.), Himalayan tectonics (Geological Society Special Publication No. 74, pp. 69–87). Geological Society of London.

Treloar, P. J., Rex, D. C., 1990. Cooling and uplift histories of the crystalline thrust stack of the Indian plate internal zones west of Nanga Parbat, Pakistan Himalaya. Tectonophysics, 180, (2-4), 323-349.

U.S. Geological Survey (USGS), (2025a), Mineral commodity summaries 2025. U.S. Geological Survey.

U.S. Geological Survey (USGS), (2025b), About the 2025 List of Critical Minerals.

U.S. Geological Survey (USGS), (2025c, November 7), Final 2025 List of Critical Minerals. Federal Register, 90 (214), 50494–50507.

U.S. Geological Survey, (2025, November 7), Final 2025 List of Critical Minerals. Federal Register, 90(214), 50494–50507.

United Nations Environment Programme (UNEP). (2019). Global mercury assessment 2018. UN Environment Programme, Chemicals and Health Branch.

Werner, T. T., Mudd, G. M., & Jowitt, S. M. (2017). The world's by-product and critical metal resources part III: A global assessment of indium. Ore Geology Reviews, 86, 939–956.

Shoaib Ahmed Thesis MS

ORIGINALITY REPORT

8%	3%	7%	1%
SIMILARITY INDEX	INTERNET SOURCES	PUBLICATIONS	STUDENT PAPERS

PRIMARY SOURCES

1	Rizwan Sarwar Awan, Ashar Khan, Chenglin Liu, Shangfeng Yang et al. "Subsurface geological model of sedimentary and metasedimentary wedge from Mansehra to Battal based on gravity data, Hazara area, Pakistan", Energy Geoscience, 2021 Publication	1%
2	Submitted to Higher Education Commission Pakistan Student Paper	1%
3	ec.asm.org Internet Source	1%
4	Joseph A. DiPietro, Alex Pullen, Michael A. Krol. "Geologic history and thermal evolution in the Hinterland Region, Western Himalaya, Pakistan", Earth-Science Reviews, 2021 Publication	1%
5	Society of Earth Scientists Series, 2016. Publication	1%

6	Muhammad Qasim, Muhammad Asif Khan, Muhammad Haneef. "Stratigraphic characterization and structural analysis of the northwestern Hazara Ranges across Panjal Thrust, northern Pakistan", Arabian Journal of Geosciences, 2015 Publication	<1 %
7	www.researchgate.net Internet Source	<1 %
8	publikationen.bibliothek.kit.edu Internet Source	<1 %
9	sp.lyellcollection.org Internet Source	<1 %
10	Mustansar Naeem, Jean-Pierre Burg, Nasir Ahmad, Muhammed Nawaz Chaudhry, Perveiz Khalid. "U-Pb zircon systematics of the Mansehra Granitic Complex: implications on the early Paleozoic orogenesis in NW Himalaya of Pakistan", Geosciences Journal, 2016 Publication	<1 %
11	www.coursehero.com Internet Source	<1 %
12	"The geochemical and tectonic evolution of the central Karakoram, North Pakistan", Philosophical Transactions of the Royal	<1 %

	Society of London. Series A, Mathematical and Physical Sciences, 1997 Publication	
13	Douglas L. Miles. "Geological Applications of Plasma Spectrometry", Inductively Coupled Plasma Spectrometry and its Applications, 11/11/2006 Publication	<1 %
14	www.benchchem.com Internet Source	<1 %
15	Mustansar Naeem, Tehseen Zafar, Muhammad Nawaz Chaudhry, Jean-Pierre Burg, Nasir Ahmad, Hafiz Ur Rehman. "Mineralogy and geochemistry of calc-alkaline magmatic rocks from the Mansehra Granitic Complex, NW Himalaya, Pakistan: insights into petrogenesis and tectonic setting", Arabian Journal of Geosciences, 2021 Publication	<1 %
16	Raja Asim Zubair, Xiaoping Long, Mirza Shahid Baig. "Structural geometry, kinematics and paleostress of the Main Boundary Thrust: New constraints from the Hazara-Kashmir syntaxis, Northwest Himalayas, Pakistan", Journal of Asian Earth Sciences, 2022 Publication	<1 %

17	Jie Wei, An Wang, Tianyi Shen, Ganyu Lyu, Haoruo Li, Guocan Wang. "Reduction in the rate of exhumation of the Gangdese Mountains (Tibetan Plateau) through the Neogene and its implications for crustal shortening of the Himalaya", Palaeogeography, Palaeoclimatology, Palaeoecology, 2025 Publication	<1 %
18	Qianyu Li, Wen Zhang, Wanpeng Zhou, Pinghua Liu, Lilin Du, Chonghui Yang, Jianlong Wang, Hao Sun, Biao Fu, Guochun Zhao. "Detrital Zircon U-Pb-Hf Isotopes of the Changzhougou Formation in the Central–Southern Taihang Mountains and their Tectonic Implications", Acta Geologica Sinica - English Edition, 2026 Publication	<1 %
19	"Kinematic model for the Main Central thrust in Nepal", Geology, 2003 Publication	<1 %
20	Faisal Shahzad. "Remote sensing analysis of ongoing deformation in Hazara Kashmir Syntaxis in Northern Pakistan", 2008 Second Workshop on Use of Remote Sensing Techniques for Monitoring Volcanoes and Seismogenic Areas, 11/2008 Publication	<1 %

21	Kyle Keeler, Nathaniel Otjen. "AI goes nuclear: the environmental injustice of a nuclear and tech renaissance", Geoforum, 2026 Publication	<1 %
22	Muhammad Qasim, Lin Ding, Muhammad Asif Khan, Ishtiaq A. K. Jadoon et al. "Tectonic Implications of Detrital Zircon Ages From Lesser Himalayan Mesozoic-Cenozoic Strata, Pakistan", Geochemistry, Geophysics, Geosystems, 2018 Publication	<1 %
23	hppcb.nic.in Internet Source	<1 %
24	Dickin, A.P.. "A neodymium isotope study of plutons near the Grenville Front in Ontario, Canada", Chemical Geology, 19900625 Publication	<1 %
25	Basab Mukhopadhyay, Anshuman Acharyya, Debkumar Bhattacharyya, Sujit Dasgupta, Prabhas Pande. "Seismotectonics at the terminal ends of the Himalayan Arc", Geomatics, Natural Hazards and Risk, 2011 Publication	<1 %
26	Submitted to Hong Kong Baptist University Student Paper	<1 %

27	Ishtiaq A. K. Jadoon, Matthias Hinderer, Allah B. Kausar, Aziz A. Qureshi, Mirza S. Baig, Mohammad Basharat, Wolfgang Frisch. "Structural interpretation and geo-hazard assessment of a locking line: 2005 Kashmir earthquake, western Himalayas", Environmental Earth Sciences, 2014 Publication	<1 %
28	Samuel Chukwujindu Nwokolo, Edson L. Meyer, Chinedu Christian Ahia. "Eco-Mineral Recycling 4.0 and 5.0 - A Sustainable and Intelligent Path to Meeting Clean Energy Needs", CRC Press, 2026 Publication	<1 %
29	www.svemoresultat.se Internet Source	<1 %
30	Malay Mukul. "The geometry and kinematics of the Main Boundary Thrust and related neotectonics in the Darjiling Himalayan fold-and-thrust belt, West Bengal, India", Journal of Structural Geology, 2000 Publication	<1 %
31	Zhong, H.. "Shrimp U-Pb zircon geochronology, geochemistry, and Nd-Sr isotopic study of contrasting granites in the Emeishan large igneous province, SW China", Chemical Geology, 20070115	<1 %

	Publication	
32	d-nb.info Internet Source	<1 %
33	www.mdpi.com Internet Source	<1 %
34	James E. Fraser. "Chronology of deformation, metamorphism, and magmatism in the southern Karakoram Mountains", Geological Society of America Bulletin, 11/2001 Publication	<1 %
35	criticalstrategicmetals.com Internet Source	<1 %
36	erepo.uef.fi Internet Source	<1 %
37	stage.nma.org Internet Source	<1 %
38	Lima, J.L.F.C.. "Multi-pumping flow system for the spectrophotometric determination of dipyrone in pharmaceutical preparations", Journal of Pharmaceutical and Biomedical Analysis, 20030808 Publication	<1 %
39	www.hindawi.com Internet Source	<1 %

40	Khawaja M. Asim, Muhammad Awais, F. Martínez–Álvarez, Talat Iqbal. "Seismic activity prediction using computational intelligence techniques in northern Pakistan", Acta Geophysica, 2017 Publication	<1 %
41	Muhammad Zaheer, Muhammad Sabir Khan, Muhammad Saleem Mughal, Noman Abbasi. "Petrography, provenance, diaganesis and depositional environment of Murree Formation in Jhelum Valley, Sub Himalayas, Azad Jammu and Kashmir, Pakistan", Arabian Journal of Geosciences, 2017 Publication	<1 %
42	m.moam.info Internet Source	<1 %
43	M. P. Searle, M. B. Crawford, A. J. Rex. "Field relations, geochemistry, origin and emplacement of the Baltoro granite, Central Karakoram", Transactions of the Royal Society of Edinburgh: Earth Sciences, 2011 Publication	<1 %
44	R. B. S. Yadav, Yusuf Bayrak, J. N. Tripathi, S. Chopra, A. P. Singh, Erdem Bayrak. "A Probabilistic Assessment of Earthquake Hazard Parameters in NW Himalaya and the	<1 %

	Adjoining Regions", Pure and Applied Geophysics, 2011 Publication	
45	W. Joel Schiffer, Delores M. Robinson, Shah Faisal, Harold H. Stowell. "Exploring the tectonostratigraphy of the Pakistan Himalaya with new detrital zircon geochronology and neodymium isotope data from the Kaghan Valley", Geoscience Frontiers, 2023 Publication	<1 %
46	www.freepatentsonline.com Internet Source	<1 %
47	"Tectonic synthesis", Physics and Chemistry of the Earth, 1992 Publication	<1 %
48	Searle, Michael P.. "Diagnostic features and processes in the construction and evolution of Oman-, Zagros-, Himalayan-, Karakoram-, and Tibetan-type orogenic belts", Geological Society of America Memoirs, 2007. Publication	<1 %

Exclude quotes	Off	Exclude matches	Off
Exclude bibliography	Off		